CHARACTERIZATION AND RECONSTRUCTION OF COHERENT STRUCTURES IN WAKE FLOWS USING MODAL ANALYSIS

A Dissertation

by

THOMAS S. FOWLER, IV

Submitted to the Office of Graduate and Professional Studies of
Texas A&M University
in partial fulfillment of the requirements for the degree of

DOCTOR OF PHILOSOPHY

Co-Chairs of Committee,	Sharath Girimaji
	Freddie Witherden
Committee Members,	Moble Benedict
	Michael Moreno
Head of Department,	Srinivas Rao Vadali

December 2020

Major Subject: Aerospace Engineering

ABSTRACT

Large-scale coherent structures play a vital role in many turbulent flows of interest: atmospheric flows, astrophysical phenomena, oceanic circulation, and engineering applications over a variety of fields. In aerodynamics/fluid mechanics, wake flows are some of the most prevalent and practical flows of interest. Despite major advances in computational capabilities, the cost of direct numerical simulation will remain exorbitant for the foreseeable future. Reduced-order reconstructions of flows provide a 'real-time' CFD analog, approximating representation of large-scale structures and maintaining reasonable physical fidelity. These representations specifically capture the dominant instabilities and resulting large-scale phenomena, which often satisfy engineering purposes. This also aids in data compression, alleviating a growing problem of memory allocation and storage. Various system-level analysis tools are enabled, making the fluid dynamic effects readily accessible to subsystems for automated monitoring. Developments in these techniques stand to provide physically accurate flow phenomena for the field of visualization, too. By isolating the large-scale structures, components of the full reconstruction can be superimposed on base flows, providing cost-effective physical fidelity where small-scale features can be introduced independently toward desired aesthetics.

Modal decomposition techniques like proper orthogonal decomposition (POD) and dynamic mode decomposition (DMD) are ideally suited for developing a reduced-order representation of various flow field quantities. Both are well-established in the analysis of complex flows. However, a consensus is lacking regarding how such techniques should contribute toward representations of variable fidelity as prescribed by an end-user.

The primary objectives of this dissertation are to (i) characterize large-scale coherent structures in wake flows; and (ii) investigate different aspects of reduced-order reconstruction of wake flow fields utilizing POD and DMD. To accomplish this the canonical flow past a square cylinder has been computed in three key regimes: (i) steady laminar ($Re = 200$; steady in-flow); (ii) pulsatory laminar ($Re = 200$; pulsatory in-flow); and (iii) steady turbulent ($Re = 22,000$; steady in-flow).

The flow past a square cylinder contains several flow phenomena of importance to engineering applications, namely: massive separation, vortex-shedding, secondary instabilities, and coherent structures. Adequately capturing and isolating the effects of these phenomena contributes to a fuller understanding of the critical mechanisms inherent in wake flow physics.

CONTRIBUTORS AND FUNDING SOURCES

Contributors

This work was supported by a dissertation committee consisting of Professors Sharath S. Girimaji [advisor] and Freddie D. Witherden [co-advisor] of the Department of Ocean Engineering, Professor Moble Benedict of the Department of Aerospace Engineering, and Professor Michael R. Moreno of the Department of Mechanical Engineering.

All work conducted for the dissertation was completed by the student independently.

Funding Sources

Graduate study was supported by a fellowship from Texas A&M University.

NOMENCLATURE

DNS	Direct Numerical Simulation
CFD	Computational Fluid Dynamics
POD	Proper Orthogonal Decomposition
DMD	Dynamic Mode Decomposition
PSD	Power Spectral Density
PISO	Pressure-Implicit with Splitting of Operators
LIC	Linear Integral Convolution
PANS	Partially-Averaged Navier-Stokes
QoI	Quanity of Interest
SPOD	Spectral Proper Orthogonal Decomposition
RANS	Reynolds-Averaged Navier-Stokes
LES	Large Eddy Simulations
SRS	Scale-Resolving Simulations
PITM	Partially Integrated Transport Model
SFS	Sub-Filter Stress
VS	(von Kármán) Vortex-Shedding
KH	Kelvin-Helmholtz
FSPOD	Fourier-Spectral Proper Orthogonal Decomposition
CSPOD	Chebyshev-Spectral Proper Orthogonal Decomposition
SVD	Singular Value Decomposition
NPOD	Normalized Proper Orthogonal Decomposition

TABLE OF CONTENTS

Page

LIST OF FIGURES

FIGURE Page

LIST OF TABLES

TABLE Page

1. INTRODUCTION

Large scale coherent structures are inherent to many high Reynolds number, turbulent flows such as jets, wakes, and mixing layers [25, 26, 27]. These large-scale structures play a vital role in atmospheric flows, astrophysical phenomena, ocean circulation, and engineering applications [28, 29, 30, 31, 32, 33, 34, 35]. Despite the recent growth in computational capabilities, full-scale direct numerical simulations (DNS) of Navier-Stokes equations – that accurately compute the coherent structures by resolving all scales of motion (from integral to Kolmogorov) – are still too expensive.

In many investigations of scientific and engineering interest, an approximate description of the large-scale features is adequate. Therefore, a reduced-order representation of the structures with reasonable fidelity to the flow physics and governing equations is sought in many real-world applications. In multi-disciplinary engineering optimization problems where fluid flow is only one of the many considerations, reduced, even if approximate, rendering of the flow field is valuable for quick turn-around times of the design cycle. For example, the computation of the response of a structure to fluid forcing (flow-induced vibrations) requires that only large-scale flow features be known and many of the finer features are not very relevant for the engineering outcome.

Technological advancement of this kind would enable further development of concepts for active monitoring of wake flow conditions. One of these concepts, *digital twin*, has gained popularity for the efficient and safe functioning of engineering assets operating in extreme conditions – e.g., offshore oil and gas platforms, remote-controlled or autonomous ships, etc. Utilizing physical probes (or other measurements) to identify key characteristics of the flow, additional information can be extrapolated to model the remainder of the unmeasured wake. This enables a fully digital, real-time rendering which can predict how the flow will develop. Another concept, *video-to-video synthesis*, achieves a similar result through optical analysis and pattern recognition. Rather than measure the flow, video-to-video synthesis would allow for the identification of key features/structures in the flow from video which could then be modeled accordingly to predict fu-

ture behavior. This type of flow prediction lends itself to significant advancements in automation and augmentation of available data for operators/engineers to better make decisions. For example, in the instance of offshore platforms, this can lead to the development of low-fidelity representations of surrounding ocean currents based upon a combination of video input and/or strategically placed pressure or velocity probes. These representations can then be integrated into autonomous or user-assisted processes that monitor conditions and respond accordingly.

Another important reason for seeking a formal reduced-order representation of flow field stems from the need to compress data stemming from extremely large-scale computations [36, 37, 38, 39]. Currently, many DNS computations of flow fields are being performed motivated by different scientific objectives. Typically, post-processing of the full flow field is performed for meeting the objectives of the research investigation and the data is then archived in some form for future use. The volume of data generated is large and archival storage is emerging as a key challenge. At the present, different means of systematically compressing data using physics-inspired reduction techniques are being sought.

The third motivation for physics-based simplified flow representation comes from the field of visualization. In the entertainment industry, realistic depiction of flow phenomena is advancing rapidly to incorporate increasingly physically accurate features. By isolating the key physical structures and simplifying them in this manner, coherent structures can be overlaid onto fluid flows for visualization purposes. This mitigates the need for specific simulations tailored to a given scenario while maintaining physical fidelity at a much lesser computational cost. The output representation can then be augmented with artistic small-scale features to yield a realistic synthetic flow field.

In summation, reduced-order reconstructions that capture the large-scale structures in complex flows would enable reasonably accurate 'real-time' CFD which in turn would make many other system-level analysis tools possible. Such tools include concepts like digital twins and/or video-to-video synthesis, both extracting key information and modeling overall effects upon the system. This could provide real-time data approximating the applicable forcing and be used by engineers

to make any necessary adjustments. These techniques could also prove useful in the entertainment industry. By extracting the mean flow characteristics and the relevant large-scale structures, physically accurate renderings can be overlaid for use in a variety of media depicting fluid flow.

Modal decomposition techniques, such as proper orthogonal decomposition (POD) and dynamic mode decomposition (DMD) are ideally suited for developing a reduced-order representation of signals and vector fields of various types. Both being well-established in the analysis of complex flows, they provide fundamental building blocks toward this endeavor. However, a consensus is lacking on how such techniques should contribute toward representations of different degrees of fidelity as prescribed by the end-user.

The primary objectives of this dissertation are to (i) characterize large-scale coherent structures in wake flows; and (ii) investigate different aspects of reduced-order reconstruction of wake flow field using POD and DMD. The wake of the flow past a square cylinder is chosen as the benchmark flow for various reasons. In aerodynamics/fluid mechanics, wake flows are some of the most prevalent and practical flows of interest, and a thorough understanding/monitoring is required to ensure safety and efficiency. For example: optimizing safety and efficiency on congested airports runways [40, 41, 42, 43]; efficient operation of wind farms [44, 45, 46, 47]; mitigating detectable wakes of submersibles [48, 49, 50]; safe operation of offshore platforms [51, 52, 53, 54]; each of these instances is subject to catastrophe if not provided sufficient consideration.

Toward this end, this dissertation addresses various aspects that contribute toward the development of a reduced-order reconstruction methodology which can be applied to high-fidelity wake flow data. To accomplish this the canonical flow past a square cylinder has been utilized in three key regimes: (i) steady laminar ($Re = 200$; steady in-flow); (ii) pulsatory laminar ($Re = 200$; pulsatory in-flow); and (iii) steady turbulent ($Re = 22,000$; steady in-flow). The specific studies undertaken are:

I. Pulsating Flow Past a Square Cylinder: Analysis of Force Coefficient Spectra and Vortex Structure Development [55] (Chapter 2);

II. Partially-Averaged Navier-Stokes Simulations of Turbulent Flow past a Square Cylinder:

Comparative Assessment of Statistics & Coherent Structures at Different Resolutions [56] (Chapter 3); and

III. Toward Data-Driven Reduced-Order Spatio-temporal Reconstruction of Wake Flows using Modal Analysis (Chapter 4).

The flow past a square cylinder contains several flow phenomena of importance to engineering applications, namely: massive separation, vortex-shedding, secondary instabilities, and coherent structures. Adequately capturing and isolating the effects of these phenomena contribute to a fuller understanding of the critical mechanisms inherent in wake flow physics.

In the first study, steady and pulsatory laminar flows past a square cylinder ($Re = 200$) are analyzed in preparation for characterizing flow structures in the turbulent regime. The main objective of the study is to examine the changes to the laminar vortex-shedding flow structures induced by time-dependent forcing. This study is used to gain insight into the regimes before, during, and after the 'lock-in' regime. It has a significant impact on the variation of the vortex-shedding frequency and forces experienced by the body. Additional insight into the way the vortex-structure develops differently under each regime is sought along with correlations to forces and probe spectra. The prior works of Minewitsch [1] and Steggel and Rockliff [2] are expounded upon to accomplish these objectives.

Flow past a square cylinder within the turbulent regime is computed using the partially-averaged Navier-Stokes (PANS) technique for varying degrees of scale-resolution in the second study. PANS – a bridging SRS method – offers a precision-on-demand aspect, enabling increased efficiency over DNS and large eddy simulations (LES) while improving accuracy as compared to Reynolds-averaged Navier-Stokes (RANS) models. The precision demanded for various quantities of interest (QoI) depends on the complexity of the flow in question and the required degree of accuracy for its application. The study serves two objectives: (i) to establish the accuracy of PANS for this wake flow; and (ii) to characterize the large-scale coherent structures in the wake.

In the final study, a dataset obtained from a high-fidelity PANS simulation is utilized to demonstrate a general, reduced-order reconstruction methodology for wake flows. The primary objective

of this work is to develop this methodology using fundamental modal analysis techniques, for which a combination of POD and DMD is used. Three aspects contributing to the robustness and accuracy of the reconstruction are assessed: (i) local normalization of the flow field; (ii) pre-filtering of small time- and spatial-scales; and (iii) optimization of the sampling rate.

This dissertation is organized into three studies comprising Chapters 2, 3, and 4, each utilizing the canonical flow past a square cylinder. The first study (Chapter 2) investigates the correlations between vortex-structure development under pulsatory laminar in-flow and the forces imparted on the body. The second study (Chapter 3) utilizes the PANS technique to compute turbulent simulations, assess their accuracy according to their varied scale-resolution for different QoI, and then further develop a method for quantified comparison of coherent structures. Finally, the third study (Chapter 4) utilizes a dataset from a high-fidelity PANS simulation to develop and demonstrate a reduced-order methodology for wake flow reconstruction. The conclusions obtained from each study are then summarized in the final chapter (Chapter 5).

2. PULSATING FLOW PAST A SQUARE CYLINDER: ANALYSIS OF FORCE COEFFICIENT SPECTRA AND VORTEX STRUCTURE DEVELOPMENT[1]

This study examines the changes in force coefficients and wake flow structures of a square cylinder subject to pulsating in-flow at different frequencies. The Reynolds number is 200*, according to previous literature. Over a range of forcing frequencies, a regime is observed where the shedding frequency scales with the forcing frequency rather than the natural shedding frequency, known as the lock-in phenomenon in literature. The change in spectral character across three frequency regimes – pre-lock-in, lock-in, and post-lock-in – are examined and characterized. During pre-lock-in, the shedding frequency remains equal to the natural shedding frequency. However, the corresponding peak in lift coefficient (C_L) power spectral density (PSD) is a single decade larger than that of the neighboring minima. This contrasts greatly with subsequent regimes where the amplitudes of the peaks are observed to be substantially larger than the amplitudes of the neighboring minima. The onset of lock-in is sharp, and the corresponding excitation frequency is identified. The shedding frequency becomes a function of the forcing frequency within this regime, and the corresponding C_L PSD peak is four decades larger than that of neighboring minima. The transition beyond the lock-in regime is more gradual with peaks of the spectra broadening until separating into multiple discrete peaks. To comprehend the changes in the force coefficients, the vortex structure in the wake is characterized at different frequencies. The connection between the vortex development sequence and force profile is investigated and z-vorticity probes are utilized to correlate these qualitative observations with prior quantitative analysis. Three-dimensional flow effects are also examined.*

[1]Reprinted with permission from "Pulsating Flow Past a Square Cylinder: Analysis of Force Coefficient Spectra and Vortex Structure Development" by T.S. Fowler IV, F.D. Witherden, and S.S. Girimaji, 2020. ASME: Journal of Fluids Engineering, 142 (12), 121106, ©2020 by ASME.

2.1 Introduction

Wake flows exhibit multiple important features such as separation, shear-layer instability, and vortex shedding. Canonical examples of wake flows are those past square and circular cylinders. On account of their simple geometries, these configurations are ideally suited for investigating the complex physics of wake flows. Such flows also represent a simplified model for the forces experienced by offshore and naval structures subject to current- and wave-type hydraulic forces [57, 58]. Under certain circumstances, these conditions can trigger a phenomenon known as vortex-induced vibration [59] which, in turn, can amplify the forces experienced by the body and result in premature failure of the structure. There is significant interest in means and/or mechanisms for vortex suppression [60, 61, 62, 63]. In the context of naval architecture, the situation is complicated by the fact that the freestream is highly pulsatile.

The goal of this work is to examine the response of square cylinder wake flows subjected to an unsteady (pulsating) inflow. An important advantage of the square cylinder is that the point of separation is subject to less variation than in the circular cylinder; a property which enables other flow features to be examined with greater precision. The presence of inflow unsteadiness profoundly changes the wake structures and forces experienced by the body. It is known from studies of circular geometries that resonant frequencies exist which can significantly affect the shedding frequency, as well as substantially affect lift and drag forces [64, 65]. This phenomenon is referred to as "lock-in", where the vortex shedding frequency "locks in" with the inline vibration frequency (or forcing frequency, depending on the reference frame). Outside of the regime where this phenomenon occurs, inline vibration frequencies have a minimal impact on the vortex shedding frequency, remaining quite similar to that observed under steady flow conditions. While some literature exists for square geometries [1, 2] there is limited data around the transition into and out of lock-in. Furthermore, much insight can be gained by analyzing the development of the vortex structures in each regime, leading to improved understanding of the aforementioned phenomena. The effect of three-dimensional (3D) features must also be understood.

For the case of steady flow past a square cylinder, Jiang and Cheng [7] have recently investi-

gated the variations of hydrodynamic forces and wake flow characteristics over a range of Reynolds number ($10 \leq Re \leq 400$) using both two- (2D) and three-dimensional direct numerical simulations (DNS). Here, the Reynolds number is defined as $Re = U_\infty D/\nu$, where U_∞ is the incoming freestream velocity, D is cylinder diameter (or side length in the case of the square cylinder), and ν is the kinematic viscosity. The authors identify the values of critical Reynolds number which demarcate various flow instabilities, as follows:

i. $Re = 46$, the onset of vortex shedding;

ii. $Re = 165.7$, where mode A instability manifests;

iii. $Re = 210$, where mode B instability leads toward more three-dimensional effects; and

iv. $Re = 330$, where the recirculation region becomes intermittent.

In this work, the authors have discussed the development of the spanwise-varying mode A and mode B instabilities, and related them to those instabilities found for circular geometries, identified by Williamson [66].

For the case of circular cylinder, Tanida et al. [65] investigated transverse and inline oscillations for $40 \leq Re \leq 10^4$. A synchronization with the forcing frequency is found about twice the natural shedding frequency for transverse oscillations and similarly about twice the natural shedding frequency for inline fluctuations. Likewise, Griffin and Ramberg [64] studied these inline oscillations for $Re = 190$ and found similar lock-in behavior about twice the natural shedding frequency ($1.2 \leq f_e/f_0 \leq 2.5$) for equivalent $0.07 \leq x_e/D \leq 0.30$ and noted similar synchronization to other experiments at higher and lower Reynolds number. Okajima [6] investigated the variation of vortex shedding frequency with regard to $70 \leq Re \leq 2 \times 10^4$ over a rectangular prism, ranging from aspect ratios of 1 to 4, subject to steady flow. More recently, Dutta et al. [67] presented results for inline oscillations of a square cylinder at $Re = 170$ and 355, $f_e/f_0 = 0$, 0.5, 1.0, and 2.0, focusing primarily on visualizations, velocity profiles, and vorticity contours within the scope.

Some studies of oscillatory flow past a square cylinder have been performed at $Re = 200$. Minewitsch et al. [1] performed DNS over a wide array of excitation conditions ($0.5 \leq f_e/f_0 \leq$

4; $0.05 \leq x_e/D \leq 0.40$) to parameterize regimes of distinctly different behavior. The primary regimes for antisymmetric shedding proposed are referred to as: (i) regime of superposition; (ii) lock-in; and (iii) transition regime beyond lock-in. As the forcing frequency and/or amplitude are increased beyond the lock-in regime, flow structures near the body eventually transition from developing asymmetrically to symmetrically, returning to asymmetry farther downstream. This behavior is precedented by studies of circular geometries, which reported a competition between several asymmetric modes and a symmetric mode of vortex shedding, under various vibrations and orientations [68, 69, 70]. Furthermore, this work notes the existence of *combination frequencies* and recommends that they be further investigated. Steggel and Rockliff [2] expounded upon this work using a hybrid discrete vortex method to investigate various aspect ratio rectangular cylinders ($0.4 \leq L/D \leq 2.5$) and subjecting them to $x_e/D = 0.10$, 0.20 for a range of forcing frequencies $1 \leq f_e/f_0 \leq 3$. This study further identifies a secondary region of lock-in for the cases of $L/D = 2$, $x_e/D = 0.20$, and $f_e/f_0 \geq 2$ where the shedding frequency reportedly synchronizes with the forcing frequency. It is also suggested that the results at moderately low Reynolds number have similarities to those performed at higher Reynolds number, but would require further study to confirm.

In this work, we extend the studies of Minewitsch et al. [1] and Steggel and Rockliff [2] to examine the three regimes of forcing in more details. Specifically, we seek to:

i. characterize the differences in the force spectra in the three regimes; and

ii. establish the sequence of flow events in each regime in an effort to identify the physics underlying the lock-in mechanism.

We perform DNS for the case of pulsating flow at $Re = 200$ over a range of excitation frequencies for a fixed excitation amplitude. Using force coefficient histories, along with their power spectral density (PSD) estimates, distinct regimes are examined, highlighting the distinguishing physics inherent in each.

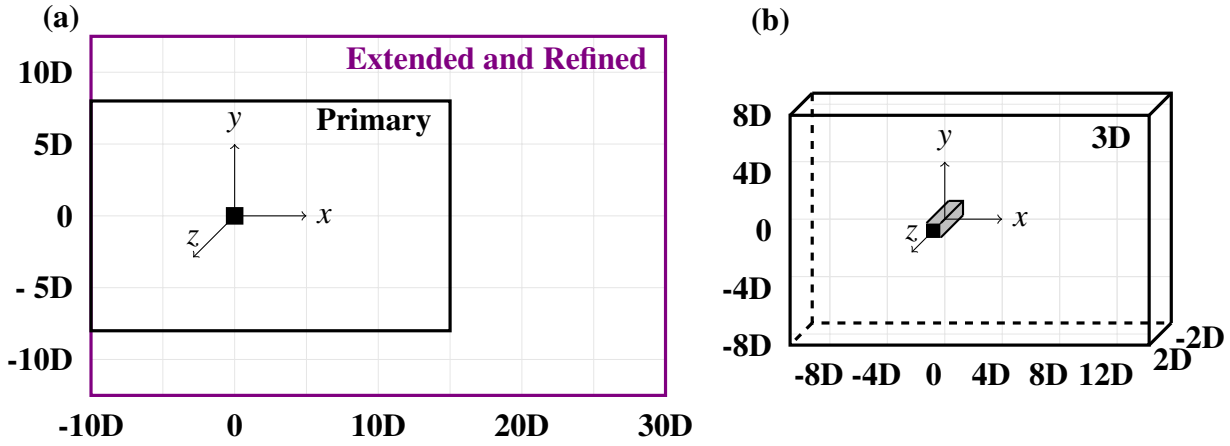

Figure 2.1: (a) Streamwise-normal view of the Primary (P) and Extended and Refined (ER) grid domains, measuring $25D \times 16D$ and $40D \times 25D$, respectively. (b) The three-dimensional grid domain is simply an extrusion of the P-grid by $4D$ in the z-direction, measuring $25D \times 16D \times 4D$. Further details are provided in Table 3.1 regarding the computational domains and point distributions of these grids.

2.2 Numerical Methodology

In order to simulate flow over a square cylinder geometry, we employ the incompressible form of the Navier-Stokes equations along with the continuity equation:

$$\frac{\partial \mathbf{u}}{\partial t} + (\mathbf{u} \cdot \nabla)\mathbf{u} = -\nabla P + \nu \nabla^2 \mathbf{u}; \tag{2.1a}$$

$$\nabla \cdot \mathbf{u} = 0; \tag{2.1b}$$

where $\mathbf{u}$ represents the velocity vector; P is pressure; and ν is the kinematic viscosity. The value of kinematic viscosity is then determined according to the Reynolds number of the flow.

The computational domain is depicted in Figure 2.1, Figure 2.2, and detailed in Table 3.1, utilizing a Cartesian coordinate system (x, y, z) such that the origin coincides with the center of the square cylinder. The x-direction is aligned streamwise, the y-direction crosswise, and the z-direction spanwise. As is detailed in Table 3.1, these structured grids have uniform spacing along the cylinder faces and geometric grading elsewhere throughout the domain. It can also be noted that

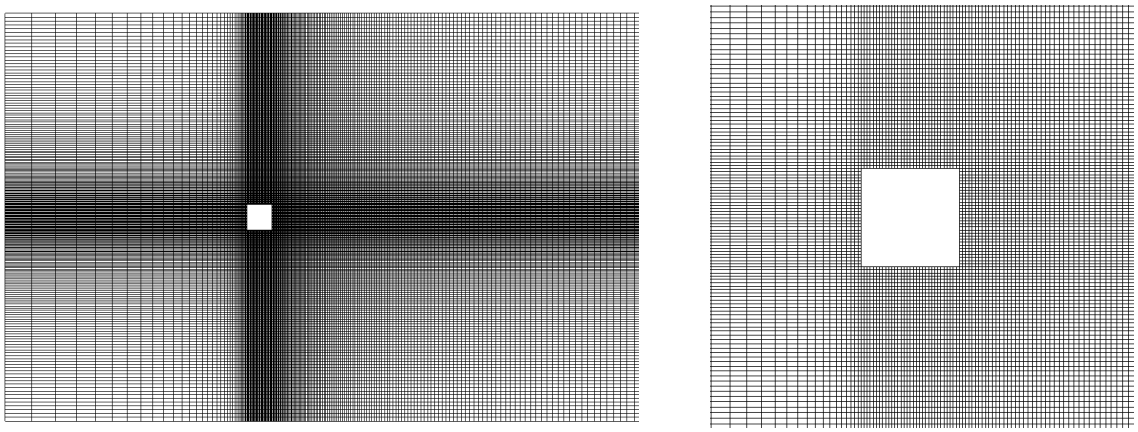

(a) (b)

Figure 2.2: (a) Wireframe representation of the full domain of the Primary (P) grid. (b) A zoomed-in view of the cells surrounding the square cylinder for P-grid. Further details are provided in Table 3.1 regarding their specific distribution.

Table 2.1: Grid sizes used for various computations. Tangential and perpendicular grid spacing about the cylinder faces are given by $\Delta x_t/D$ and $\Delta x_p/D$.

Grid	Physical Domain	Computational Domain	# of Points	$\Delta x_t/D$	$\Delta x_p/D$
P	$25D \times 16D$	192×224	$84,928$	$1/32$	$1/32$
ER	$40D \times 25D$	359×388	$267,598$	$1/80$	$1/50$
3D	$25D \times 16D \times 4D$	$192 \times 224 \times 30$	$1,316,384$	$1/32$	$1/32$

the key differences between the Primary (P) and Extended and Refined (ER) grids is an increased resolution about the square cylinder and an extension of the domain by $15D$ in the downstream direction and by $4.5D$ in the positive and negative y-directions. A temporally varying velocity profile is prescribed at the inlet with a mean of unity (i.e., $U_\infty = 1$). This reduces to a steady inflow velocity for the validation case ($f_e = 0$). A convective boundary condition is applied at the outlet plane (opposite the inlet), no-slip conditions at the cylinder faces, and periodic conditions at the transverse planes (and spanwise planes, in the three-dimensional cases).

This study focuses on inline oscillations of incoming flow, also called pulsating flow. This

Table 2.2: Parameter regime for all simulations and studies. All filled circles represent specific values of the normalized forcing frequency, f' which were run.

Batch	No. of Runs	f' Simulations	Objective
P-I	16	0 0.5 1 1.5 2 2.5 3	Validation with Literature [2]
P-II	8	0 1 2 3 4	Extension of Range
P-III	10	1.62 1.63 1.64 1.65 1.66 1.67 1.68	Onset of Lock-in
P-IV	5	2.52 2.54 2.56 2.58	Transition Out of Lock-in
ER	8	0 0.5 1 1.5 2 2.5 3	Verification of 2D Grid
3D	10	0 0.5 1 1.5 2 2.5 3	Investigation of 3D Effects

pulsation of the inlet velocity is applied in a manner similar to that used by Minewitsch et al. [1] and Steggel and Rockliff [2]:

$$U_i = U_\infty + U_A \sin(2\pi f_e t); \tag{2.2a}$$

$$U_A = 2\pi f_e x_e; \tag{2.2b}$$

where the magnitude of this velocity pulsation, U_A, is a function of the excitation amplitude, x_e, and excitation frequency, f_e. The excitation frequency is selected relative to the natural shedding frequency, f_0 (the special case of f_s at $f' = 0$), and normalized as:

$$f' = \frac{f_e}{f_0}. \tag{2.3}$$

All cases in this work use $x_e/D = 0.20$, which falls in the middle of the range studied by Minewitsch [1] and is similarly used by Steggel and Rockliff [2]. Both studies indicate that the distinct regimes occur for a wide range of x_e/D values, and as such, this value has been selected for ease of comparison. The normalized forcing frequency, f', is varied over the range of values

detailed in Table 2.2. Between the three configurations, 57 simulations are reported: 39 using the P-grid (2D) for $0 \leq f' \leq 4$; 8 using the ER-grid (2D) for $0 \leq f' \leq 2.6$; and 10 on the 3D-grid for $0 \leq f' \leq 3$.

During these simulations, spanwise-averaged lift and drag coefficients, C_L and C_D, are evaluated at every time step. They are calculated in situ according to the following:

$$C_D = \frac{F_x}{\frac{1}{2}AU_\infty^2}; \tag{2.4a}$$

$$C_L = \frac{F_y}{\frac{1}{2}AU_\infty^2}; \tag{2.4b}$$

where F_x and F_y are the net forces acting on the cylinder in the x- and y-directions, respectively, and A is the area of the projected face of the cylinder. With these force coefficient histories, the mean drag coefficient, $\overline{C_D}$, the mean lift coefficient $\overline{C_L}$, and the root-mean-square of the lift coefficient, C_L', is calculated by averaging over no fewer than 50 shedding cycles, which was found to converge for all aforementioned variables:

$$\overline{C_D} = \frac{1}{N}\sum_{i=1}^{N} C_{D,i}; \tag{2.5a}$$

$$\overline{C_L} = \frac{1}{N}\sum_{i=1}^{N} C_{L,i}; \tag{2.5b}$$

$$C_L' = \sqrt{\frac{1}{N-1}\sum_{i=1}^{N}(C_{L,i} - \overline{C_L})^2}; \tag{2.5c}$$

where $C_{D,i}$ and $C_{L,i}$ represent the value of C_D and C_L at each time step and N is the total number of time steps included in the averaging period.

The PSD is then computed using Welch's overlapped segment averaging estimator [71]. The primary peak found in the C_L power spectra is then recorded as the shedding frequency, f_s, and

reported in its dimensionless form as the Strouhal number, St_s, or normalized with f_e as follows:

$$St_s = \frac{f_s D}{U_\infty}; \tag{2.6a}$$

$$f^* = \frac{f_e}{f_s}; \tag{2.6b}$$

where the subscript, s, denotes the shedding frequency.

These simulations are performed in OpenFOAM [72] using the Pressure-Implicit, Split-Operator (PISO) algorithm [73]. Second-order finite volume schemes are used for spatial and temporal discretization. The time steps for each simulation are selected for efficiency while maintaining a Courant number less than one throughout the domain.

2.3 Validation

Simulating the steady flow case is essential, both to ensure that our methodology is capturing the relevant phenomena and to establish a reference shedding frequency, f_0 with respect to each grid employed. This case corresponds to the parametric extreme of $f_e = 0$ or $x_e = 0$. The main quantities of interest are: St_s, $\overline{C_D}$, and C_L'. The results for these quantities are listed alongside those in the literature in Table 2.3 and Table 2.4 for two-dimensional studies and three-dimensional studies, respectively.

All cases are initialized with the velocity throughout the domain equal to that of the mean inflow velocity. Each case is given sufficient time to develop ($t^* = tU_\infty/D \geq 375$) and averaged over a period at least as long. This is equivalent to at least 50 shedding cycles of initialization and averaging. This allows sufficient time for the development of periodic vortex shedding – the Bénard-von Kármán instability [74] – and is evident by the characteristic periodicity of the C_L time history.

The $\overline{C_D}$ values found in this work match well with the reported literature. Furthermore, all $\overline{C_L}$ values are approximately zero, as expected from the symmetry of the flow. Findings for C_L'

Table 2.3: Summary of steady flow over square cylinder literature for $Re = 200$ (2D).

Authors	Phys. Domain	Comp. Domain	St_s	$\overline{C_D}$	C_L'
Okajima [6]	N/A	N/A	0.139, 0.1451		
Luo et al. [8]	N/A	N/A	0.159		
Luo et al. [9]	N/A	N/A	0.165		
Franke et al. [4]	20D×12D	186×156	0.157	1.6	
Minewitsch et al. [1]	20D×12D	70×64	0.16	1.5	
Okajima [5][1]				1.450	
Steggel and Rockliff [2]			0.154	1.461	0.362
Sohankar et al. [3]	22D×18D	169×121	0.170	1.46	0.32
Jiang and Cheng [7]	60D×60D		0.153	1.442	0.413
Present	25D×16D	192×224	0.159	1.503	0.438
	40D×25D	359×388	0.153	1.484	0.433

[1] as reproduced by Steggel and Rockliff [2]

tend towards higher values, however, this appears to be sensitive to domain size and boundary conditions. In Franke et al. [4] the authors instead report a C_L fluctuation value of ± 0.62 and this matches well with the two-dimensional cases which have C_L fluctuation values of ± 0.620 and ± 0.613 for the P- and ER-grids, respectively.

The PSDs for the two-dimensional simulations' lift and drag coefficient histories are shown in Figure 2.3. Note that the spectra are presented in log-log scale and as such might appear different than others within literature. Within the C_L spectra, the primary peak corresponds to $f_0 = 0.159$ for the P-grid and $f_0 = 0.153$ for the ER-grid, and the secondary peak then corresponds to a higher harmonic, $3f_0$. Similarly, for the C_D spectra, the primary peak corresponds to $2f_0$, as is expected from literature, and the secondary peak also corresponds to a higher harmonic, $4f_0$. It is clear from the spectra that:

i. The P-grid is sufficient for capturing the force coefficient spectra, as there is marginal difference between that of the P-grid and the ER-grid, despite its markedly higher resolution.

Table 2.4: Summary of steady flow over square cylinder literature for $Re = 200$ (3D).

Reference	Phys. Domain	Comp. Domain	St_s	$\overline{C_D}$	C'_L
Okajima [6]	N/A	N/A	0.139, 0.1451		
Luo et al. [8]	N/A	N/A	0.159		
Luo et al. [9]	N/A	N/A	0.165		
Sohankar et al. [3]	22D×18D×6D	169×121×25	0.157	1.39	0.21
	22D×18D×10D	169×121×41	0.160	1.41	0.22
Saha et al. [10]	24D×10D×6D	178×80×32	0.161	1.60	
Jiang and Cheng [7]	60D×60D×15D		0.149	1.393	0.248
Present	25D×16D×4D	192×224×30	0.156	1.491	0.369

ii. The St_s indicated by the C_L spectra is in good agreement with the reported literature, as the St_s found lies in the middle of the range in literature ($0.139 \leq St_s \leq 0.170$; indicated by the yellow region).

iii. The primary peak for the C_D spectra is in good agreement with the reported literature, although we note that few quantitative results are available for comparison.

Therefore, further simulations will utilize the P-grid for the sake of computational efficiency.

A limited number of three-dimensional simulations are also performed for this study, the results of which can be seen in Table 2.4. Preliminary findings indicate that the primary integral quantities were not strongly affected by the inclusion of three-dimensional effects, and most importantly, neither are the characteristics of the spectra. Therefore, it was decided that two-dimensional simulations are sufficiently rich for spectral analysis and thus selected for computational efficiency. However, it is noted in Sohanakar et al [3] that mode A instability does initiate at $Re = 200$. While this was also visible in preliminary 3D cases, again, at this time it does not seem to impact the spectral characteristics and will require further investigation in the future.

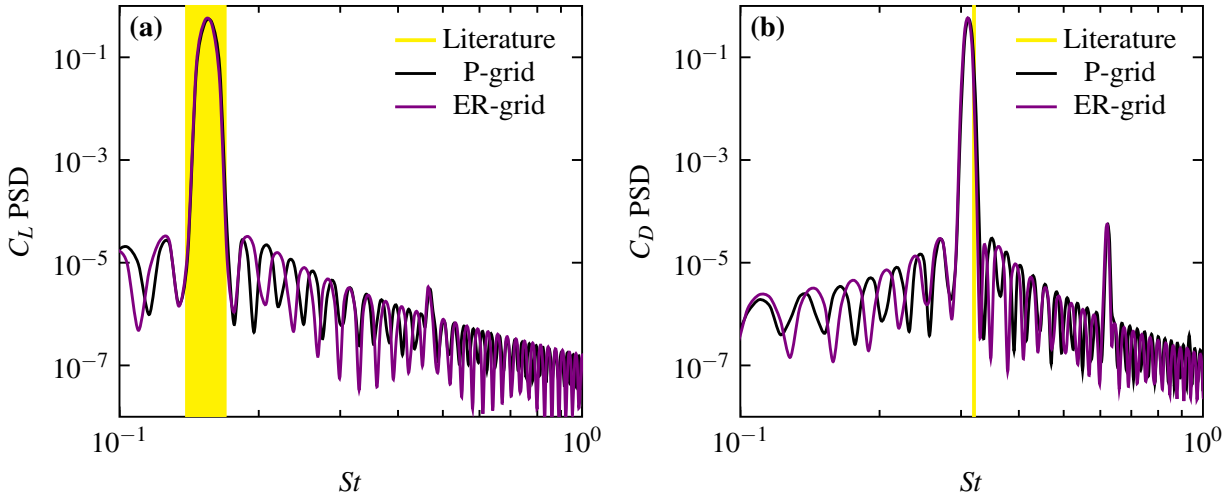

Figure 2.3: Force coefficient power spectra for steady flow over a square cylinder for simulations performed with the Primary (P) and Extended and Refined (ER) grids: (a) C_L spectrum, compared against the range of literature [1, 2, 3, 4, 5, 6, 7, 8, 9, 10], indicated by a highlighted vertical band; (b) C_D spectrum compared against Minewitsch et al. [1], also indicated by a highlighted vertical line.

2.4 Results & Discussion

For this work, the normalized forcing frequency, f' is varied as $0 \leq f' \leq 4.0$ (as detailed in Table 2.2) and $x_e/D = 0.20$ is selected in order to compare to results found in Steggel & Rockliff [2]. This parameter space contains representative examples of all regimes of interest, however, the analysis performed could similarly be applied for any choice of x_e/D. That analysis is as follows:

i. Summarization of primary integral quantities ($\overline{C_D}$, C_L', and f^*) for the full range of f' and validation with available literature [2]. [Figure 2.4]

ii. Examination of force coefficient power spectra to determine predominant frequencies and spectral characteristics, before, during, and after the lock-in regime. [Figures 2.5, 2.6]

iii. Qualitative observations of z-vorticity contours illustrating representative shedding cycles and highlighting differential vortex-structure development, before, during, and after the lock-in regime. [Figures 2.7-2.11]

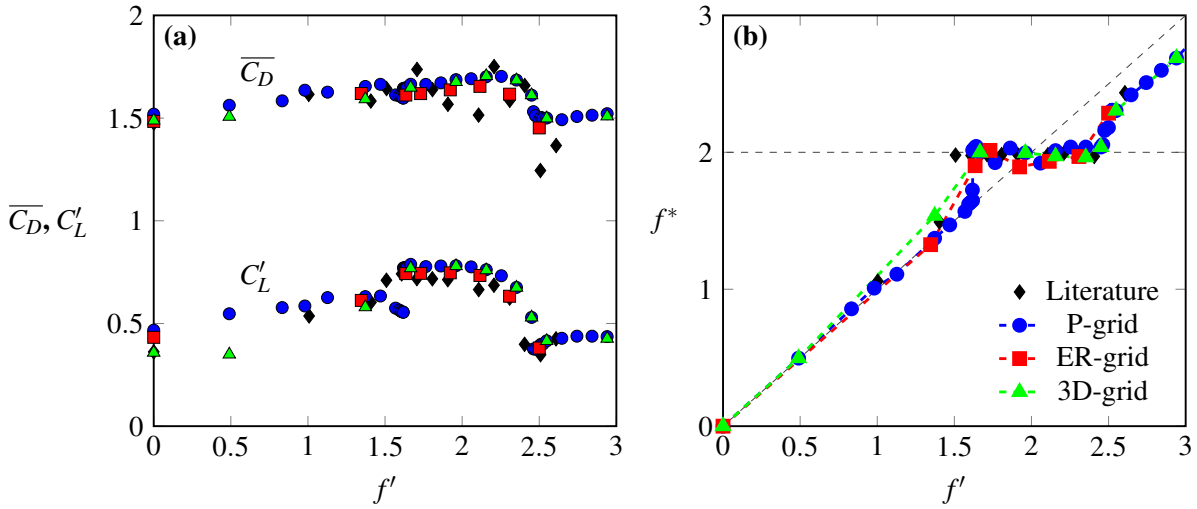

Figure 2.4: Primary integral quantities for inline oscillating flow over a square cylinder at $x_e/D = 0.20$ for the Primary (P), Extended and Refined (ER), and three-dimensional (3D) grids compared against prior work by Steggel and Rockliff [2]: (a) $\overline{C_D}$,C'_L versus f'; (b) f^* vs. f'

iv. Correlation between prior quantitative and qualitative analysis for the sake of clarifying specific connections which explain the lock-in mechanism and contrast against the behavior seen before and after. [Figures 2.12-2.15]

v. Verification of the efficacy of two-dimensional simulations in providing insight into a three-dimensional problem by comparing the coefficient of lift power spectra. [Figure 2.16]

2.4.1 Demarcation and Validation of Different Frequency Regimes

The three regimes noted by Minewitsch [1] are clear from Figure 2.4:

i. the regime of superposition (pre-lock-in);

ii. the lock-in regime; and

iii. the transition regime beyond lock-in (post-lock-in).

During pre-lock-in ($f' < 1.6$) the shedding frequency remains the same as the natural shedding frequency ($f^* = f'$). The onset of the lock-in regime ($1.6 \leq f' \leq 2.4$) is hallmarked by a sharp

jump in f^* to a value of 2, or rather, where $f_s = f_e/2$. The shedding frequency,f_s, immediately drops 20% below f_0, and then increases linearly with f_e. It continues increasing until reaching a peak value approximately 20% above f_0. The initial jump in f^* is furthermore preceded by a small decline in $\overline{C_D}$ and C_L'. Both force coefficients are higher within the lock-in regime, C_L' more so, relative to values in the previous regime. This is established in literature [2, 1] and also observed by similar circular cylinder studies [65, 75]. Over the transition regime beyond lock-in ($f' > 2.4$), the decrease in $\overline{C_D}$ is less distinct than C_L', reducing by 12% as compared to 50%. This reduction, however, brings $\overline{C_D}$ back towards values similar to that of steady flow. In this regime, $f^* \neq 2$ and f_s slowly approaches f_0 as f' increases. Beyond $f' \geq 3$, we observe (in agreement with the findings of Minewitsch[1]) that f^* approaches f'. These results also match well with the findings of Steggel & Rockliff [2] with the exception of $\overline{C_D}$ over the lock-in regime. However, here they noted that "The drag is more erratic and it is difficult to say how the flow pulsations have influenced the mean drag." This is an indication that this phenomena is numerical in nature, rather than physical, as all of the domains used in the present study are in good agreement, continuing to slightly increase until entering the transition regime.

2.4.2 Spectral Analysis of Different Frequency Regimes

In order to further investigate lock-in phenomena, the PSD of the lift and drag coefficients are generated from their histories as detailed in Section 2.2. For all C_L spectra (presented in Figure 2.5), the natural shedding frequency, f_0, is indicated by a dashed line and colored green if the shedding frequency $f_s \approx f_0$, red if $f_s < f_0$, and blue if $f_s > f_0$. The range between f_s and f_0 is highlighted in the same color. For all C_D spectra (presented in Figure 2.6), the applied forcing frequency, f_e is indicated by a red dashed line. In all regimes, the primary C_L peak occurs at the shedding frequency, f_s, and all subsequent peaks align according to $f_n = |f_s + nf_e|$ for some positive integer, n, in agreement with the combination frequencies identified by Minewitsch [1] . Similarly, the primary C_D peaks occur at the forcing frequencies and their harmonics. Again, note that the spectra which follow are presented in log-log scale and as such may appear different than comparable literature.

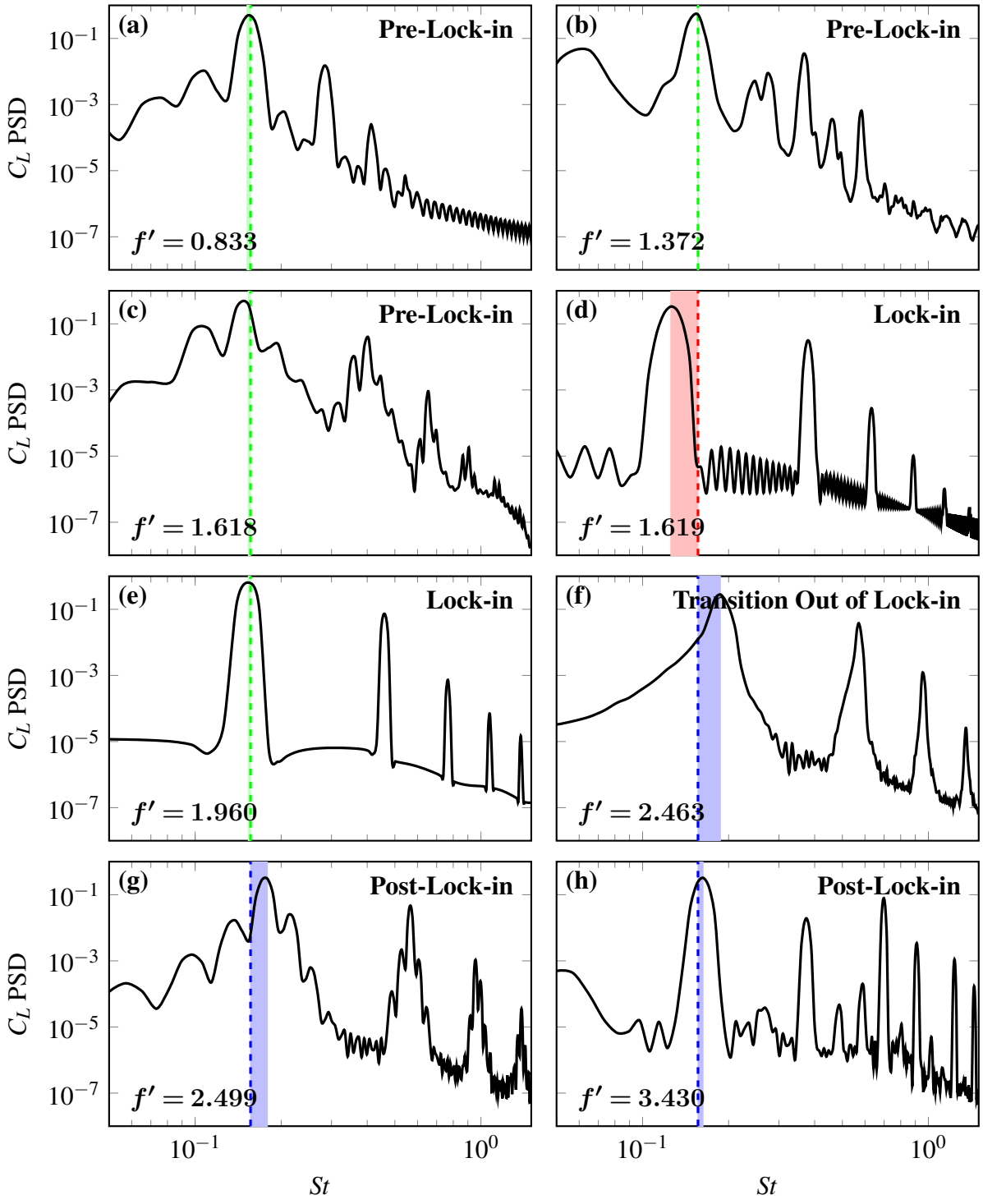

Figure 2.5: Lift coefficient power spectra for inline oscillating flow over a square cylinder, as performed on the P-grid (2D), for a sampling of f': (a) $f' = 0.833$; (b) $f' = 1.372$; (c) $f' = 1.618$; (d) $f' = 1.619$; (e) $f' = 1.960$; (f) $f' = 2.463$; (g) $f' = 2.499$; (h) $f' = 3.430$. The natural shedding frequency, f_0, is indicated by a dashed line in each plot and the range between f_s and f_0 is highlighted for reference.

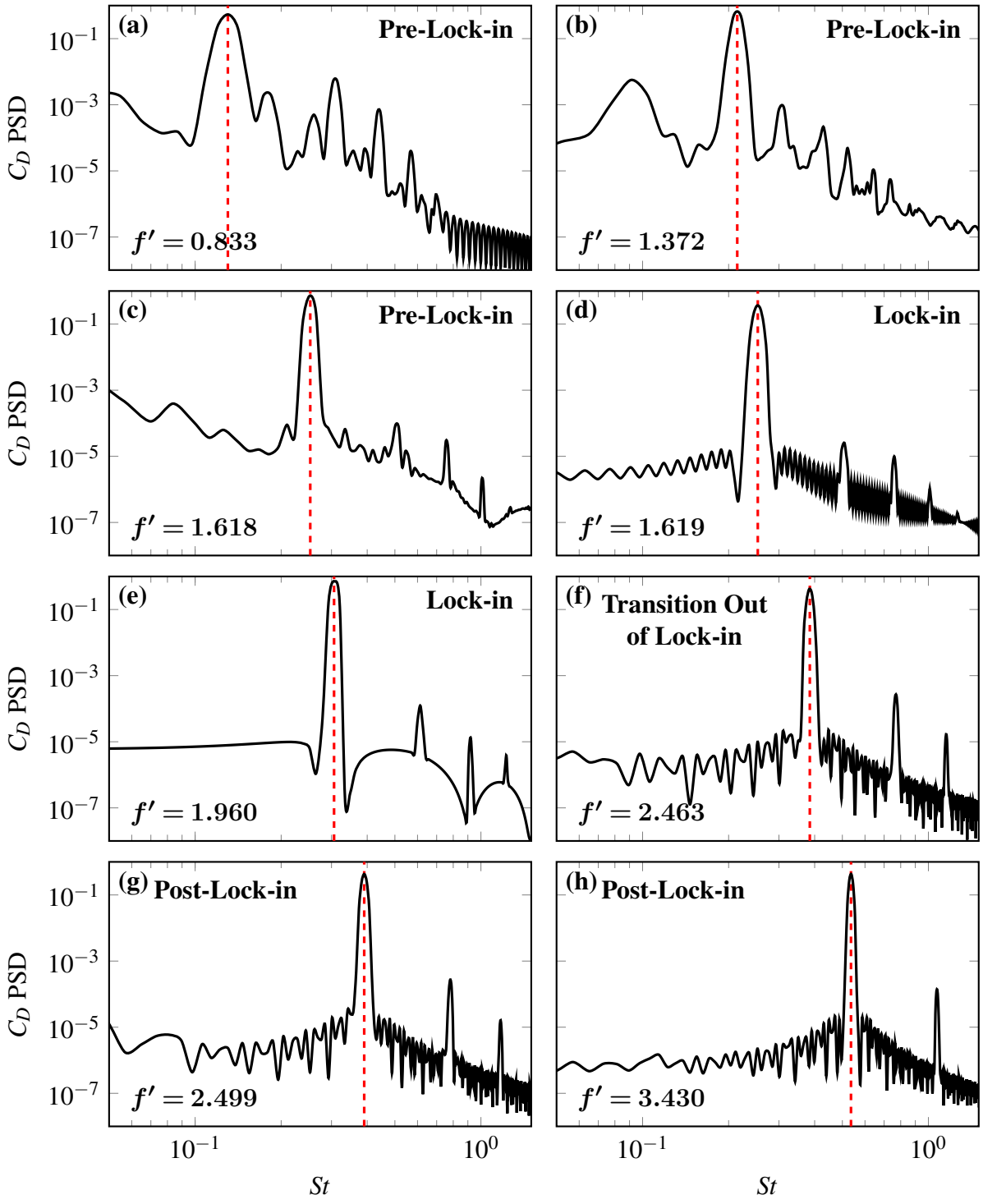

Figure 2.6: Drag coefficient power spectra for inline oscillating flow over a square cylinder, as performed on the P-grid (2D), for a sampling of f': (a) $f' = 0.833$; (b) $f' = 1.372$; (c) $f' = 1.618$; (d) $f' = 1.619$; (e) $f' = 1.960$; (f) $f' = 2.463$; (g) $f' = 2.499$; (h) $f' = 3.430$. The applied forcing frequency, f_e is indicated by a dashed vertical line in each plot for reference.

In the pre-lock-in regime, the lower frequencies contain a relatively higher proportion of energy for both the C_L and C_D spectra (as compared to later regimes). The amplitudes of the primary peaks are observed to be substantially closer to the amplitudes of their neighboring minima: approximately 1 to 2 decades difference in the C_L spectra; and 3 to 4 decades difference in the C_D spectra, as shown in Figure 2.5 and Figure 2.6, respectively. One of the combination frequencies pointed out in Minewitsch [1], $f_g = |f_e - f_s|$, is visible as the peak prior to the primary peak. This particular peak is not visible again until the lock-in regime has passed, as during this regime, this frequency is indistinguishable from the shedding frequency itself.

As f' increases, entering lock-in, it is evident that the dynamics of the flow are more regular. All peaks become significantly more pronounced, growing to 4 and 5 decades larger than the amplitudes of their neighboring minima for the C_L and C_D spectra, again shown in Figure 2.5 and Figure 2.6, respectively. This is most apparent when comparing Figure 2.5c and 2.5d, as a slight increase in f' has yielded a significantly different power spectra. On account of the higher resolution of our spectra compared with those of Minewitsch [1], it is clear that the combination frequencies, f_n are also locked-in, remaining distinct and maintaining their energy proportionally. These peaks are most sharp/distinct as the locked-in shedding frequency aligns with the natural shedding frequency.

Once the shedding frequency reaches its maximum near $f' = 2.5$, the spectral characteristics begin to transition beyond the lock-in regime. Here the shedding frequency declines (eventually returning to $f_s = f_0$) and the characteristics of the spectra become a blend of lock-in and that of pre-lock-in. This transition is captured in Figure 2.5f as the dominant frequencies, while still pronounced, are growing more broad than previously seen during lock-in. This broadening continues until separating into multiple peaks. This behavior is distinctly different than the entrance into lock-in which began abruptly while here the transition occurs gradually; it transfers energy back into the lower frequencies and the amplitudes of the peak neighboring minima of the C_L spectra increase by approximately one decade. This is not seen in Figure 2.6 for the C_D spectra, however, due to the dominant impact of the forcing. Once more, the combination frequency, f_g, emerges as

a secondary peak along with a series of similar secondary peaks according to $f_m = |mf_e - f_s|$ for some positive integer, m.

2.4.3 Vortex Structure at Different Regimes

While prior works have characterized the shedding frequencies and integral quantities within the regimes we have identified, further insight is sought as to how the development of vortex-structures leads to these phenomena. The surface line integral convolution (LIC) technique[76] is employed which convolves noise with the velocity vector field, producing patterns which are similar to streamlines (in that they follow the velocity vector tangents). The steady flow case is first described, establishing a basis for comparison using vorticity contours. Using the same method, representative cases within four different regimes are then qualitatively reviewed, changes in their behavior noted, and then they are related to the aforementioned statistics whenever possible. The regimes are as follows:

1. steady flow ($f' = 0$);
2. pre-lock-in regime ($0 < f' < 1.6$; representative case: $f' = 1.618$);
3. lock-in regime ($1.6 < f' < 2.4$; representative case: $f' = 1.619$);
4. transition out of lock-in regime ($2.4 < f' < 2.5$; representative case: $f' = 2.463$); and
5. post-lock-in regime ($f' > 2.5$; representative case: $f' = 2.940$).

2.4.3.1 Steady Flow ($f' = 0$)

The steps within a single shedding cycle in the case of steady flow are illustrated in Figure 2.7. Discussion of this and future cycles will require the use of some common nomenclature, in particular: *SV*, or 'side vortex', refers to a vortex structure which has developed from the 'side' of the square cylinder; *RV*, or 'rear vortex', refers to a vortex structure which develops downstream of the square cylinder, generally at some stage attaching to the rear face (either originating from this location or having previously been a *SV* structure); and superscripts, $\pm$, indicate the side of

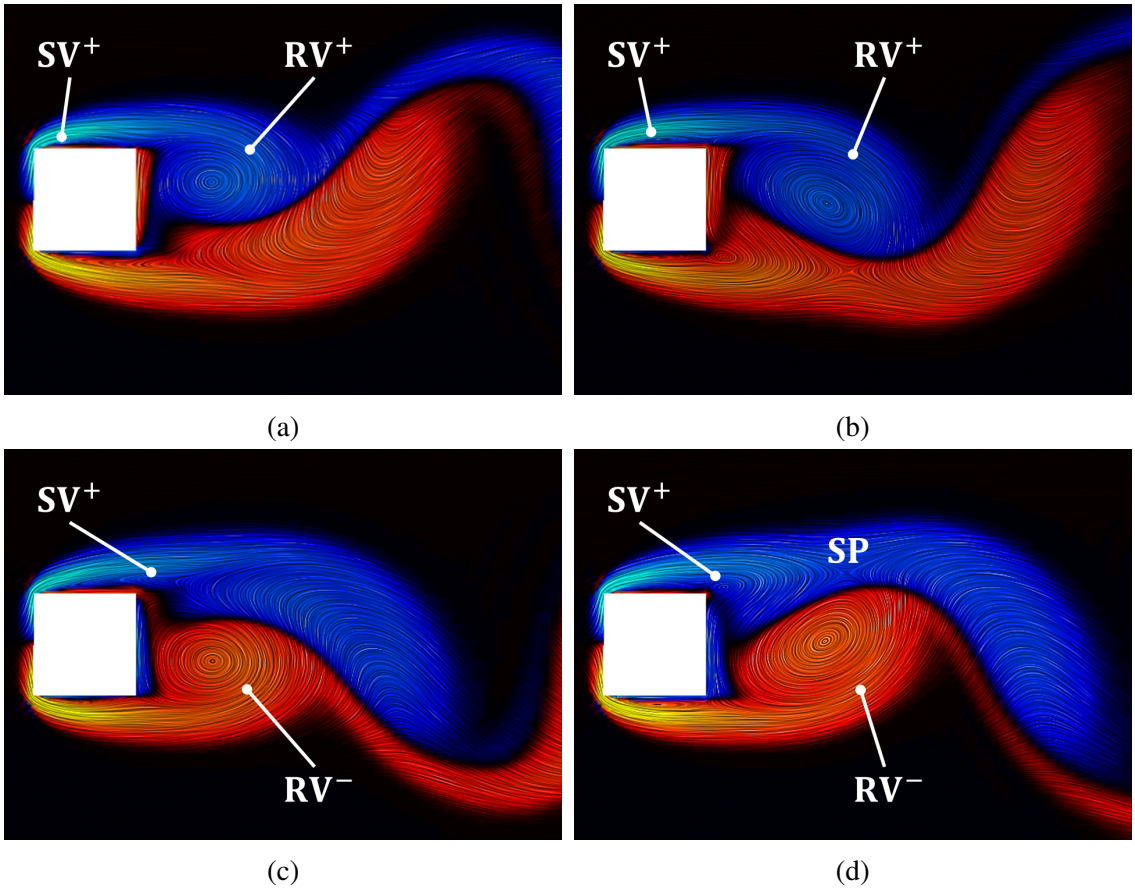

Figure 2.7: Z-vorticity contours illustrating the stages in a shedding cycle under steady flow conditions. SV^+ indicates a 'side vortex' which originated from the top face; $RV^{\pm}$ indicates a 'rear vortex' which was previously a $SV^{\pm}$ or otherwise developed from the top-rear (bottom-rear) corner; and SP indicates a saddle point which has formed between vortex structures of opposite sign.

origin, the 'top' face or 'bottom' face, respectively. The stages of the steady flow shedding cycle can then be broken down into the following:

Stage 1: An SV^+ develops from the frontward corner of the top face and expands towards the rear of the cylinder. Meanwhile, the RV^+ expands until it separates. [Figures 2.7(a-b)]

Stage 2: Having separated, the RV^+ is then deconstructed into the mean flow, forming the classical vortex street, allowing the SV^+ to be drawn backward. The SV^+ separates from the top face at this stage and its structure merges with the frontward tail of the RV^+. [Figures 2.7(b-c)]

Stage 3: As the converse vortex-structure, RV^-, grows larger, it begins to interact with the merged structure of SV^+ and RV^+. A saddle point (indicated as SP) appears between these structures, breaking them apart once more. The SV^+ then reforms, held at a 45° angle off the rear corner. [Figures 2.7(c-d)]

Stage 4: Once the RV^- separates, the SV^+ is then able to approach the rear face, reattaching itself there. It expands downward along the rear face and forms a new RV^+, thus beginning the cycle anew. [Figures 2.7(d-a)]

2.4.3.2 Pre-Lock-in Regime ($f' = 1.618$)

Spanning from the steady flow case to the lock-in regime ($0 < f' < 1.6$), the pre-lock-in regime features the lowest forcing frequencies and correspondingly the weakest forcing amplitudes. From Figure 2.4b it's clear that this regime does not affect the shedding frequency, remaining unchanged from the steady flow case. Contrastingly, in Figure 2.4a, the integral quantities increase slightly, but more significantly, in Figures 2.5(a-c) and Figures 2.6(a-c) a much broader range of frequencies exhibit activity. This is further explained by the lack of a consistent, truly 'cyclic' shedding cycle when reviewing the z-vorticity contours in time. In addition, with the implementation of a pulsating in-flow condition, effects on vortex-structure development can be seen. In the pre-lock-in regime, as the in-flow surges (referring to the period in which pulsating causes the in-flow velocity to be greater than its mean value), an inflection point (IP) appears in the flow. This change in curvature of the streamlines, or correspondingly, the change in the sign of the vorticity, generally disrupts the typical SV-structure development. While the shedding cycles within this regime can't be succinctly described, four instances are included in Figure 2.8 and explained below.

- Both SV's develop as in the steady flow case, expanding from the frontward corner towards the rear. However, the RV's are not always consistently located, and as such, alter the SV-development each cycle. For example, see the SV^-, which has grown significantly larger and expanded such that it could be mistaken for an RV^-. This inconsistency drives further inconsistency, reflecting in the spectra. [Figure 2.8(a-b)]

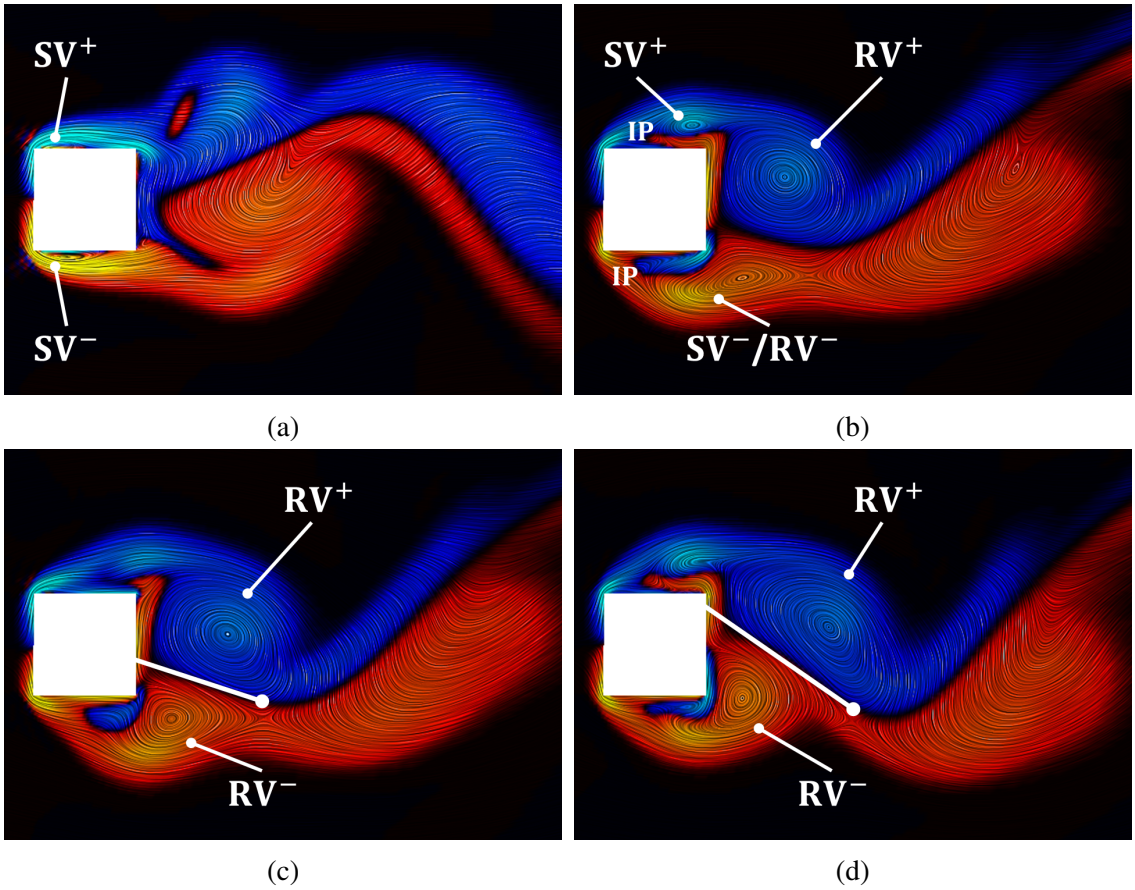

Figure 2.8: Z-vorticity contours illustrating key instances during shedding cycles within the pre-lock-in regime. $SV^{\pm}$ indicates a 'side vortex' which originated from the top (bottom) face; $RV^{\pm}$ indicates a 'rear vortex' which was previously a $SV^{\pm}$ or otherwise developed from the top-rear (bottom-rear) corner; and IP indicates an inflection point in the LIC, which is typically also highlighted by a change in the sign of vorticity, and indicates the effect of pulsations.

- The effect of the pulsating of the incoming flow is made apparent in the IP's seen disrupting the SV-structure development. Because of this, the SV^{+} remains tightly near the top face, leading to its collision with and merging/wrapping around the RV^{+}. [Figure 2.8(b-c)]

- Comparing different instances of these cycles, it's clear that within the pre-lock-in regime vortex-structures do not form consistently. The two RV^{-} structures develop near the backward face quite differently, enacting a sequence of events regarding the placement and development of the RV^{+} and therein the SV^{+} structures. [Figure 2.8(c-d)]

In the pre-lock-in regime, it is clear that the weak pulsations disrupt the vortex-structure development, both on the sides and to the rear of the cylinder. The surge in the flow caused by the pulsations appears to be just enough to push *SV*'s ahead of their natural shedding cycles, causing the *RV*'s to form irregularly and inconsistently. This in turn prohibits future *SV*'s from developing naturally, leading to an indefinite cycle where each iteration influences the next. This clearly illustrates why additional frequencies are active in Figures 2.5(a-c) and 2.6(a-c), as each cycle may have additional/varied structures which impose forces on the body outside of the primary (natural) shedding frequency.

2.4.3.3 Lock-in Regime ($f' = 1.619$)

Upon entering the lock-in regime ($1.6 < f' < 2.4$), distinct changes are noted in the shedding frequency (Figure 2.4b), C'_L (Figure 2.4a), and the characteristics of the spectra (Figure 2.5(d,e) and Figure 2.6(d,e)). Due to the latter, one would expect a clear vortex shedding pattern to emerge. In particular, due to the dependence noted of the shedding frequency, f_s, upon the forcing frequency, f_e, for every vortex shedding cycle, two forcing cycles should occur. This is clearly shown upon review of the z-vorticity contours in time, and accordingly, a representative shedding cycle within the lock-in regime can then be broken down into the following stages:

Stage 1: An SV^+ develops similarly to past regimes, with the new exception that now the recession of the flow (the period in which pulsating causes the in-flow velocity to be less than its mean value) will cause the developing structure to protrude upstream toward the front of the cylinder, expediting further growth. The surge then follows (as indicated by an *IP*), ejecting SV^+ away from the top face. Its structure then merges with the frontward tail of the RV^+, as an RV^- grows. Once the RV^- has grown sufficiently large, it introduces an *SP*, splitting the SV^+ from the RV^+ once more (resembling the shedding cycle exhibited in the steady flow case). [Figure 2.9(a-b)]

Stage 2: Due to the presence of the *SP*, the SV^+ remains along a 45° angle off the rear corner as the RV^- continues its development (again similar to the steady flow case). [Figure 2.9(b-c)]

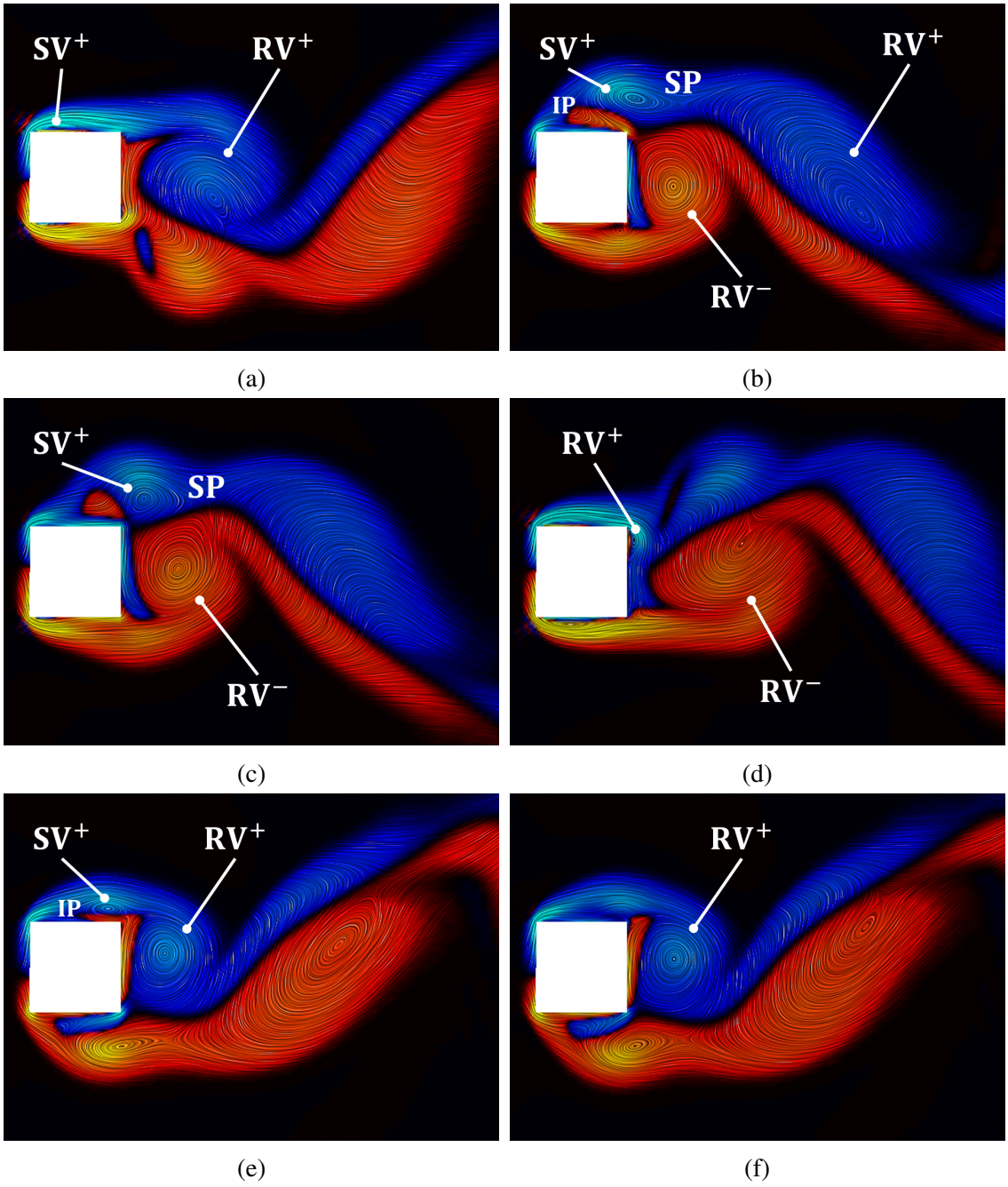

Figure 2.9: Z-vorticity contours illustrating a representative shedding cycle within the lock-in regime. SV^{+} indicates a 'side vortex' which originated from the top face; $RV^{\pm}$ indicates a 'rear vortex' which was previously a $SV^{\pm}$ or otherwise developed from the top-rear (bottom-rear) corner; *SP* indicates a saddle point which has formed between vortex structures of opposite sign; and *IP* indicates an inflection point in the LIC, which is also highlighted by a change in the sign of vorticity, and indicates the effect of pulsations.

Stage 3: With the RV^- still occupying the area rearward of the cylinder, the SV^+ shrinks down along this 45° angle, and effectively seeds the next RV^+ which then grows once the RV^- grows sufficiently large and separates. [Figure 2.9(c-d)]

Stage 4: The new RV^+ expands while another SV^+ develops and approaches the rear corner. [Figure 2.9(d-e)]

Stage 5: Due to the surge of the flow (hallmarked by another *IP*) and the influence of the large RV^+ still near, the SV^+ shrinks into the rear corner, dissipating the structure. [Figure 2.9(e-f)]

Stage 6: The RV^+ will then separate (due to this surge and/or the interaction of the former SV^+ with the corner which it was anchored) and a new SV^+ will then begin to form, repeating the cycle. [Figure 2.9(f-a)]

As can be seen from Figure 2.9, *SV*-structure development is desynchronized, unlike the pre-lock-in regime which exhibited *SV*'s developing nearly simultaneously. This behavior causes greater swings in C_L as the forcing will alternatingly be amplified by the ejection of one *SV* while the other, having developed slightly later, will end up pressed into the rear corner. The C_L' curve in Figure 2.4a is then explained by this phenomenon. With regard to the spectra shown in Figure 2.5(d,e) and Figure 2.6(d,e), the regularity and periodicity of the cycles shown in Figure 2.9 clearly illustrate why only key frequencies (along with their harmonics) remain active while this phenomenon occurs.

2.4.3.4 Transition out of Lock-in Regime ($f' = 2.463$)

Differing from the distinct shift when entering the lock-in regime, a transitional regime exists between lock-in and post-lock-in ($2.4 < f' < 2.5$). Here characteristics of pre-lock-in seem to reemerge, both integral quantities decrease substantially in this regime (as shown in Figure 2.4a), but the increased frequency and strength of pulsations appear to help stabilize this effect as suggested by the spectra shown in Figure 2.5(f,g) and Figure 2.6(f,g) and a clear pattern remains. In the former, lift spectra indicate a breakdown of the lock-in regime, however active frequencies

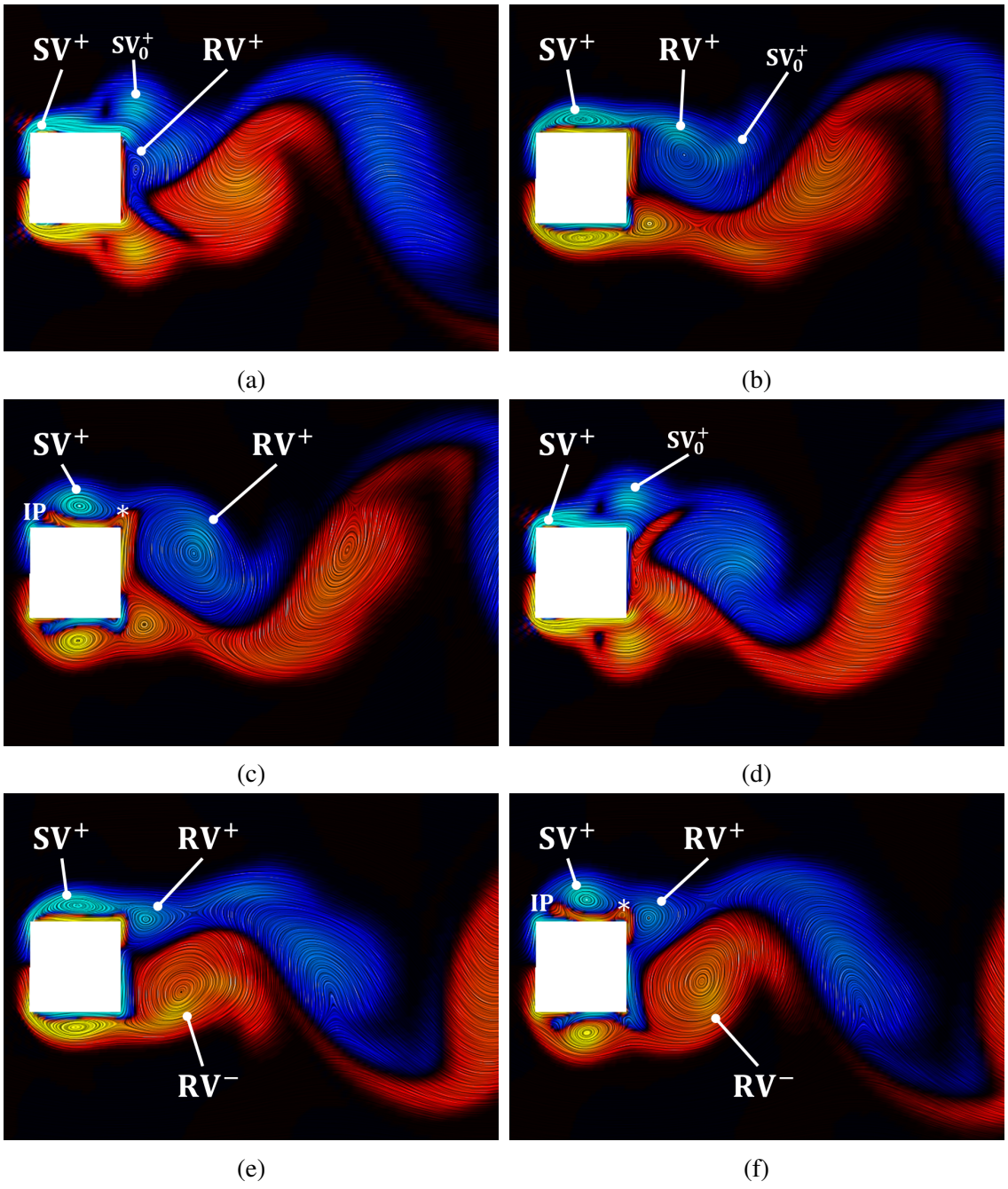

Figure 2.10: Z-vorticity contours illustrating a representative shedding cycle as f' transitions out of the lock-in regime. SV^+ indicates a 'side vortex' which originated from the top face; SV_0^+ indicates the remnant of a SV^+-structure which has been dissipated/disrupted by the surge period of a pulsation; $RV^\pm$ indicates a 'rear vortex' which was previously a $SV^\pm$ or otherwise developed from the top-rear (bottom-rear) corner; $*$ indicates a 'pinched' region between SV^+ and RV^+, which has an opposing curvature/opposite-signed vorticity; and IP indicates an inflection point in the LIC, which is typically also highlighted by a change in the sign of vorticity, and indicates the effect of pulsations.

remain centralized about those peaks previously 'locked-in'; and in the latter, drag spectra give credence to the strength of pulsation argument with forcing frequencies remaining dominant and all other frequencies lacking significant energy content. In each of the past regimes, the growing pulsations have had some additional impact upon the development of SV-structures. For this transitional regime, that new phenomenon is the deconstruction of these structures mid-development, leaving a remnant vortex structure (SV_0) within the flow, as indicated by a substantial peak in the vorticity field. Upon review of the z-vorticity contours in time, a new cycle can be identified, as follows:

Stage 1: As an SV^+ develops, similarly to other regimes, an atypically-shaped RV^+ develops too. The odd shape of this RV^+ owing directly to the passing and merging of a vortex-structure remnant, SV_0^+. [Figure 2.10(a-b)]

Stage 2: Again, the recession of the flow causes the developing SV^+-structure to protrude upstream, expediting further growth. When the surge comes, the SV^+ is then ejected outward from the top face, as well as downstream, making the IP pronounced. It is also of note that rather than an SP appearing between the upcoming SV^+ and the RV^+, there exists a 'pinched' region between the SV^+ and the RV^+, which has an opposing curvature/opposite-signed vorticity. [Figure 2.10(b-c)]

Stage 3: As the pulsation continues to surge forward, it causes the mean flow to press the SV^+ back into the cylinder face, largely dissipating it. Only an SV^+-structure remnant (SV_0^+) in the flow, visualized as a peak in the vorticity field, remains. [Figure 2.10(c-d)]

Stage 4: Another SV^+ begins development (as before), while a new RV^+ grows, expedited by the presence of an SV_0^+. Due to the presence of the RV^-, the shape of the RV^+ is more triangular and expands more upward than outward from the cylinder (reminiscent of the behavior seen in the pre-lock-in regime). [Figure 2.10(d-e)]

Stage 5: Once more, recession of the flow enables added growth by first drawing the SV^+ forward before ejecting it backward and outward (again, an IP hallmarking this effect). Again, the

'pinched' region between the SV^+ and the RV^+ is evident, rather than an *SP*. [Figure 2.10(e-f)]

Stage 6: Differing from earlier in the cycle, since the RV^- is much larger than the RV^+, the RV^+ shrinks back into the corner it came from and then expands across the back face, further distorting from its typical circular shape, and pressing back on the upcoming SV^+, as well. As the surge passes this region, the SV^+ is disrupted, largely dissipating it, and again leaving a remnant structure, SV_0^+, and repeating the cycle. [Figure 2.10(f-a)]

Similar to the pre-lock-in regime, in Figure 2.10, it is again seen that *SV*-structures develop above and below the cylinder simultaneously. This synchronization leads to the decline in C_L', as shown in Figure 2.4a, as this shift in the shedding cycle pattern leads toward a greater cancellation of the forces upon the body. However, the alternating dissipation of these *SV*-structures – mitigated by the increasing strength of the pulsations – translates to an alternating influence upon the *RV*-structures. In turn, this influence diminishes the impact which the *RV*-structures can have on future *SV*-structures. This further supports our analysis regarding the assessment of Figure 2.5(f,g) and Figure 2.6(f,g).

2.4.3.5 Post-Lock-in Regime ($f' = 2.940$)

The shedding frequency in the post-lock-in regime ($f' > 2.5$) approaches the natural shedding frequency, as shown in Figure 2.4b, similar to that of pre-lock-in. While numerous peaks emerge in the C_L spectra, seen in Figure 2.5(g,h), the secondary frequencies in the C_D spectra continue to be suppressed, seen in Figure 2.6(g,h). As the transitional regime suggests, any stability exhibited by the shedding cycle in the post-lock-in regime derives from the strong pulsations dominating the flow physics. Because of this factor, the shedding cycle does not repeat consistently, however, the z-vorticity contours are analyzed and representative instances within a shedding period identified as follows:

Stage 1: An SV^+ begins forming and is drawn forward strongly by the recession of the flow, as indicated by an *IP*. Likewise, an SV^- develops, returning to a symmetrical/synchronized

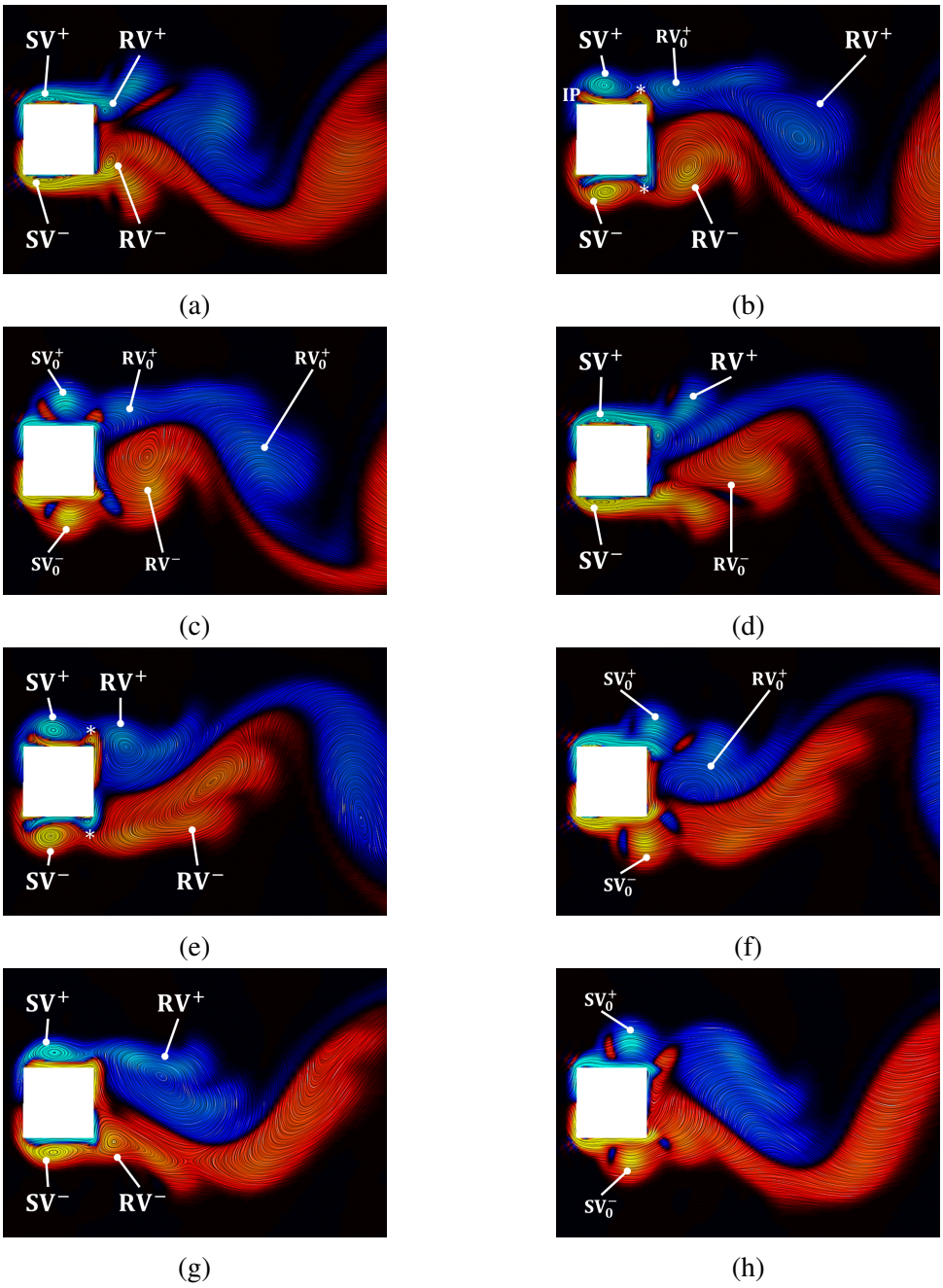

Figure 2.11: Z-vorticity contours illustrating a representative shedding cycle within the post-lock-in regime. [$SV^{\pm}$ indicates a 'side vortex' which originated from the top face; $SV_0^{\pm}$ indicates the remnant of a $SV^{\pm}$-structure which has been dissipated/disrupted by the surge period of a pulsation; $RV^{\pm}$ indicates a 'rear vortex' which was previously a $SV^{\pm}$ or otherwise developed from the top-rear (bottom-rear) corner; $RV_0^{\pm}$ indicates the remnant of a $RV^{\pm}$-structure which has been dissipated/disrupted by the surge period of a pulsation; $*$ indicates a 'pinched' region between $SV^{\pm}$ and $RV^{\pm}$, which has an opposing curvature/opposite-signed vorticity; and IP indicates an inflection point in the LIC, which is typically also highlighted by a change in the sign of vorticity, and indicates the effect of pulsations.]

pattern. Again, as in the transitional regime, there exists a 'pinched' region between the upcoming *SV*'s and *RV*'s (instead of the *SP* seen in other regimes). However, with the added intensity of the pulsations, this 'pinched' region has now developed into a reversed-sign vortex-structure, formed by the fluid being drawn back over the rear corner. The strength/size of the RV^- pushes the developing RV^+ away from the rear of the cylinder, where its structure is disrupted by the mean flow. Furthermore, the strength and speed of pulsations causes downstream structures to reconstitute. [Figure 2.11(a-b)]

Stage 2: As the surge accelerates the flow, it appears to dissipate the SV^+ and the SV^- leaving only the structure remnants, SV_0^+ and SV_0^-, in their place. Similarly, the reversed-sign vortex structure is dissipated, leaving a region of opposite-signed vorticity in the near-wake, further disrupting the other typical structures. Furthermore, the *RV* structures which had reformed downstream are once more deconstructed, leaving their own remnants behind (RV_0^+ and RV_0^-). [Figure 2.11(b-c)]

Stage 3: After the RV^- is carried downstream, a new RV^+ forms from the corner and another pair of *SV*'s begin forming. [Figure 2.11(c-d)]

Stage 4: The RV^- has merged with other partial structures near the rear corner, and as such, stretches, distorting the development of an RV^+. Again, both *SV*'s protrude forward with the recession of the flow and the reversed-sign vortex-structures appear symmetrically. [Figure 2.11(d-e)]

Stage 5: As the pulsation accelerates, both the SV^+ and the SV^- are dissipated, leaving only the remnants, SV_0^+ and SV_0^-, in the flow, along with regions of opposite-signed vorticity from those dissipated structures, as well. [Figure 2.11(e-f)]

Stage 6: The vortex remnant, RV_0^+, merges with other remnants, and is able to reform as an RV^+, inhibited only by the RV^- below which has developed and merged with SV_0^-. Meanwhile another pair of *SV*'s begin forming. [Figure 2.11(f-g)]

Stage 7: Again, pulsation surges the flow, dissipating the SV^+ and the SV^- leaving only their remnant structures behind (SV_0^+ and SV_0^-). No clear RV structures remain. [Figure 2.11(g-h)]

In the post-lock-in regime, SV's continue to behave symmetrically in a synchronized manner, as can be seen in Figure 2.11. While these structures may impart strong forces on the body, which would normally result in lift, these forces are simultaneously being negated by the forces imparted by the opposing side. This explains the drop and overall consistency of C_L' in Figure 2.4a as f' continues to increase. Based upon the drag spectra in Figure 2.6(g,h), it is clear that the strength of pulsations dominates the forces in the streamwise direction. SV's are no longer able to interact with RV development and so their interactions with each other become decoupled, decreasing their influence on the fluctuations of body forces. While the SV's have something of a cyclic pattern, the interactions between RV's, RV_0's and SV_0's lead to significant inconsistencies as were present in pre-lock-in. These in combination with the added presence of reverse-signed, small vortex-structures which form during the recession of the pulsation and then are dissipated by the surge, all cause the near-wake to tend towards a more chaotic behavior, leading to a more broadband character manifesting in the spectra seen in Figure 2.5(g,h).

2.4.4 Correlation between Vorticity Field and Lift

In the previous sections, the quantitative behavior of each regime has been analyzed, comparing the $\overline{C_D}$ and C_L', and the shedding frequencies exhibited (Section 2.4.1), along with the behavior of C_L and C_D spectra (Section 2.4.2), as well as the qualitative behavior of these regimes by means of the vortex-structures formed over a vortex shedding cycle (Section 2.4.3). In this section, we seek to correlate the two by use of probes near the rear corners of the square cylinder. These regions capture changes in the vorticity field that lead to the development of an inflection point, 'IP', in the flow which has been previously identified to distinguish oscillatory flow from steady flow. Analysis within this region should then provide physical insight into the phenomena which drives the lock-in mechanism. As the lock-in regime exhibits the most periodicity, it will be the focus of this section, specifically the case of $f' = 1.619$, with only minor comments on the characteristics

of the pre- and post-lock-in regimes, which may warrant further work in the future.

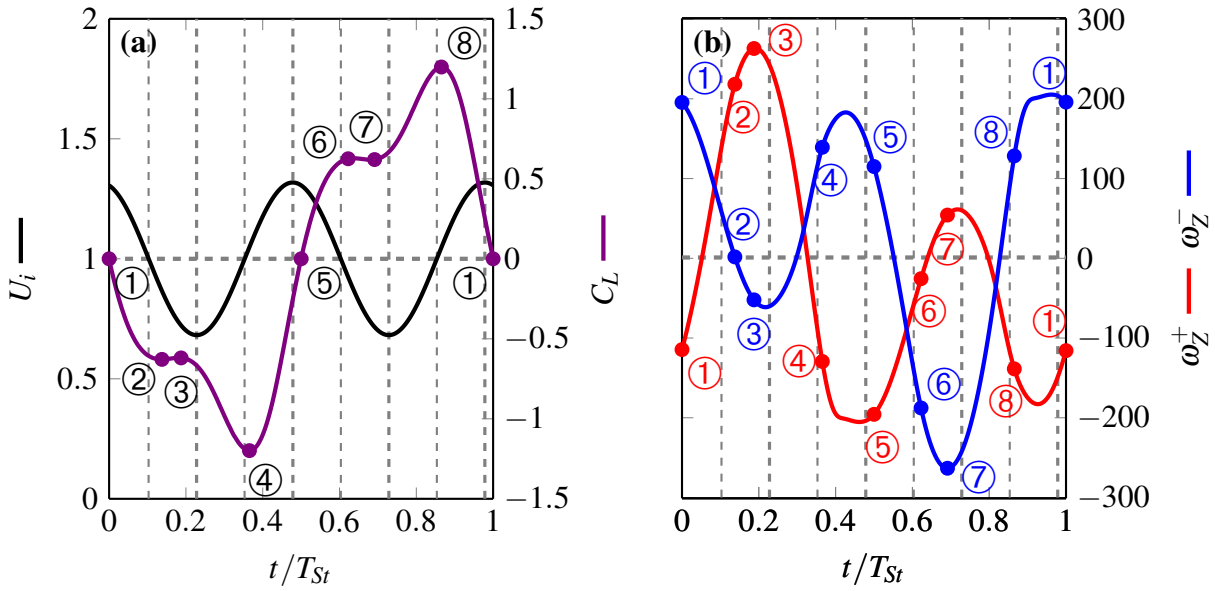

Figure 2.12: Time histories of (a) inlet-velocity, lift coefficient, and (b) z-vorticity at two locations near the surface of the square cylinder, as performed on the P-grid (2D), within the lock-in regime ($f' = 1.619$). Each occur over the same shedding cycle period and have been divided up into 8 stages based on the lift coefficient history, indicated by the circled numbers as follows: ① $C_L = 0$ (trending negative); ② C_L at a local minimum (beginning negative plateau region); ③ C_L at a local maximum (end of negative plateau region); ④ C_L at a global minimum (negative peak in the cycle); ⑤ $C_L = 0$ (trending positive); ⑥ C_L at a local maximum (beginning positive plateau region); ⑦ C_L at a local minimum (end of positive plateau region); ⑧ C_L at a global maximum (positive peak in the cycle).

The histories of inlet-velocity, lift coefficient (C_L) of the square cylinder, and the z-vorticity (ω_Z) at probe locations near the rear corners of the square cylinder are shown in Figure 2.12 over the course of one shedding cycle period. Figure 2.13 shows the power spectra for C_L and ω_Z of the upper probe (e.g. $[x, y] = [0.016, 0.022]$m). As expected, the primary peak in the C_L spectra occurs at f_s (by definition), which corresponds with $f_e/2$, with odd multiples of f_s then accounting for all later peaks in the spectra. The primary peak in the ω_Z spectra similarly occurs at f_e, with a peak of similar magnitude occurring at f_s, and all later peaks in the spectra aligning with higher harmonics

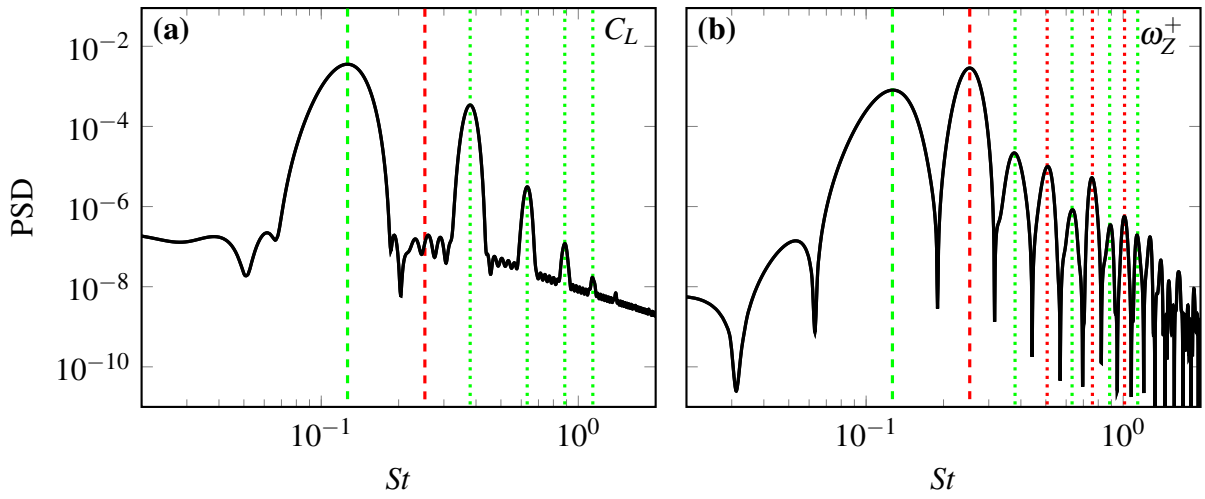

Figure 2.13: Power spectra of (a) lift coefficient and (b) z-vorticity probe (located at $[x/D, y/D] = [0.40, 0.55]$), as performed on the P-grid (2D), within the lock-in regime($f' = 1.619$). In each plot, from left to right, dashed lines indicate the shedding frequency, f_s, [- - -] and the forcing frequency, f_e, [- - -], and dotted lines are indicative of their respective harmonics [·····] and [·····], respectively.

of these two frequencies. The signals for ω_Z are very periodic, as can be seen in the spectra, as there is much less energy contained in the lower frequencies, and the energy contained decreases as frequency increases beyond f_e.

To better understand the significance of the histories shown in Figure 2.12, eight stages are identified within a shedding cycle based upon behavior of C_L. The z-vorticity contours at each of these instants is then shown in Figure 2.14 and explained below. Additionally, a white, dashed line is overlaid on the contours shown in Figure 2.14 which represent an 'equivalent shape' as created by the vortex-structures near the body. These will primarily be referenced when discussing Stages 4 and 8, but represent an approximate geometry which would have comparable flow dynamics to that of the square cylinder and these structures in concert.

Stage 1: Identified as $C_L = 0$; transitions from positive to negative. At this instance, a single larger SV^+ imparts equal force as that of the smaller SV^- and RV^- upon the square cylinder. This instance occurs slightly after the moment that the inlet-velocity, U_i, reaches its maximum (i.e. when $Ui = U\infty + U_A$).

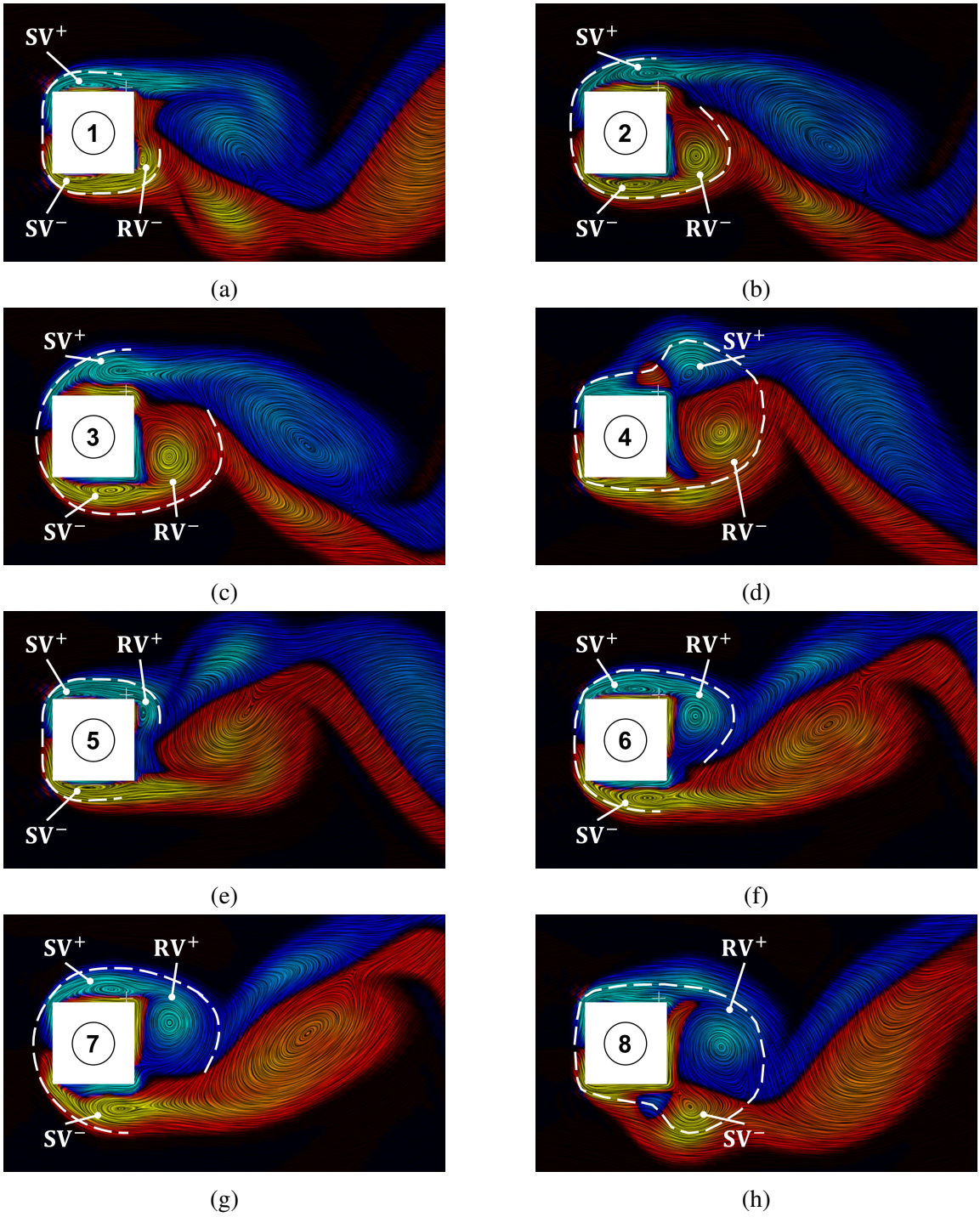

Figure 2.14: Z-vorticity contours illustrating the first half of a representative shedding cycle within the lock-in regime ($f' = 1.619$) as shown in Figure 2.12. A dashed line indicates the approximate 'equivalent shape' which the vortex-structures form near the body. These represent an approximate geometry which would have comparable flow dynamics to that of the square cylinder and these structures in concert. As before, SV^+ indicates a 'side vortex' which originates from the top face; RV^- indicates a 'rear vortex' which was previously an SV^-.

Stage 2: Identified when C_L reaches a local minimum, or rather, the first local extrema of the plateau. This feature begins slightly lagging when $U_i \leq U_\infty$ (i.e. when $U_i = U_\infty$, trending toward decreased velocity). This then coincides with the beginning of the recession of the pulsation, which allows for all vortex structures to continue expanding, rather than proceeding with shedding. Furthermore, a region of opposite-signed vorticity near the body expands from the rear corner upstream and outward on the upper surface. This effect is present on the opposite surface, but its size and magnitude are lesser.

Stage 3: Identified when C_L reaches a local maximum, or rather, the last local extrema of the plateau. This feature ends slightly before U_i reaches its minimum (i.e. when $U_i = U_\infty - U_A$), coinciding with the passing of the upper vorticity probe's maximum, which is opposite-signed than its surrounding vorticity field. This is indicative that the region of opposite-signed vorticity near the body has further expanded from the rear corner upstream and can be seen to have branched further outward from the upper surface. Additionally, it should be noted that this formation in the vorticity field is precedent to the '*IP*' which was identified in Section 2.4.3. Previously, this effect was less pronounced on the opposite surface, but its size and magnitude have grown. Otherwise, the overall shape of the various vortex-structures has remained quite similar, merely growing in place as the recession of the flow permits.

Stage 4: Identified as C_L reaching a global minimum for the cycle. This occurs slightly after when $U_i \geq U_\infty$ (i.e. when $U_i = U_\infty$, trending toward increased velocity). The acceleration of the mean flow has swept all *SV*s toward the rear of the cylinder, dissipating SV^- and ejecting SV^+ where it is prohibited from traveling downstream by the presence of the enlarged RV^-, which has only just detached from the body, being shed into the wake. What remains of the region of opposite-signed vorticity near the body (subsequent of the '*IP*') is now separated from the body, in some sense, redirecting the flow around SV^+. This leads to the 'equivalent body shape' created between the dominant vortex-structures and the square cylinder to become 'airfoil-like', allowing a higher rate of flow below the square cylinder and causing

impeded flow above, translating to lower pressure and higher pressure regions respectively, and overall resulting in the lift minimum exhibited in the C_L history.

Stages 5 through 8 then repeat the phenomena exhibited in Stages 1 through 4, completing the asymmetric nature of the lock-in regime. Between Stages 4 and 5, the continued acceleration of the mean flow presses SV^+ downward, causing it to reattach to the rear face of the square cylinder and seed the next RV^+, further pushing RV^- away where it is carried downstream. Overall, trends are comparable to the first four stages, excepting that now the lower vorticity probe will reach its minimum (again being opposite-signed than its surrounding vorticity field) at Stage 7, indicating that the region of opposite-signed vorticity near the body has further expanded from the rear corner upstream and can be seen to have branched further outward from the lower surface. Furthermore, C_L, having transitioned to being positive, reaches its maximum at Stage 8, when the 'equivalent body shape' forms the mirror-opposite as was formed in Stage 4.

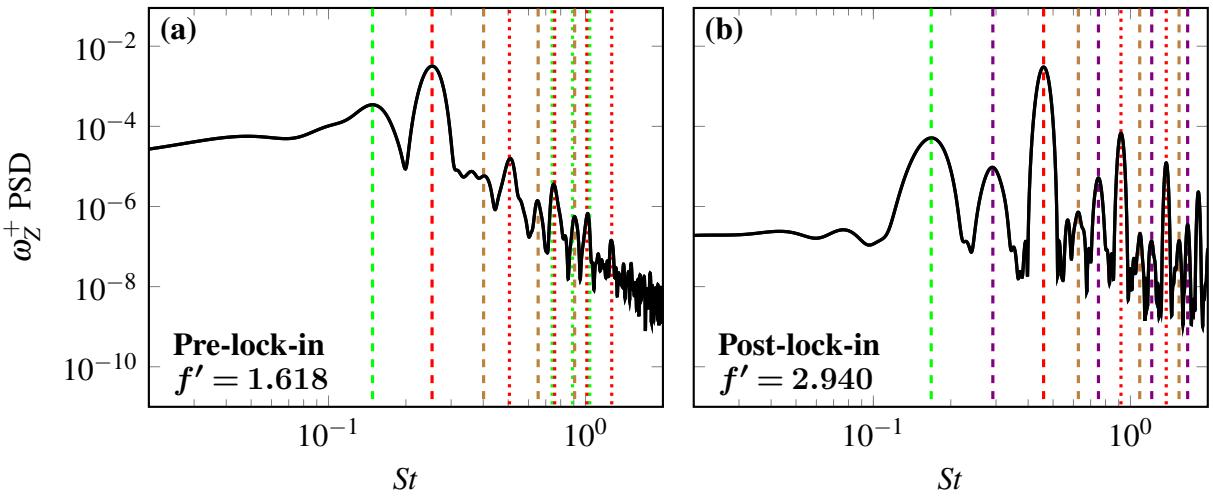

Figure 2.15: Power spectra of z-vorticity probe (located at $[x/D, y/D] = [0.40, 0.55]$) for (a) Pre-Lock-in ($f' = 1.618$) and (b) Post-Lock-in ($f' = 2.940$), as performed on the P-grid (2D). In each plot, from left to right, dashed lines indicate the shedding frequency, f_s, [- - -] and the forcing frequency, f_e, [- - -], and dotted lines are indicative of their respective harmonics [·····] and [·····], respectively. In addition, combination frequencies $f_n = |f_s + nf_e|$ and $f_m = |mf_e - f_s|$ are indicated [- - -] and [- - -], respectively.

Having analyzed how C_L varies over a shedding cycle within the lock-in regime and how vortex-structures develop and vary in accordance with the shedding frequency (f_s), forcing frequency (f_e), and their harmonics, a baseline relationship for each of these has been established. In Figure 2.15, power spectra for the z-vorticity (ω_z) of the upper probe (e.g. $[x,y] = [0.016, 0.022]$m) are shown for representative cases of the pre-lock-in ($f' = 1.618$) and post-lock-in ($f' = 2.940$) regimes. Similarly to the lock-in regime both exhibit primary peaks at f_e, but the character of the peak occurring at f_s differs. For pre-lock-in, the peak at f_s is much broader than the other regimes owing to the overall higher energy content of the low frequencies in pre-lock-in. Beyond f_e, the magnitudes decrease quickly as frequency increases, with other peaks less sharp than other regimes; those peaks including harmonics of f_e, much higher harmonics of f_s (i.e. $5f_s, 6f_s$, and $7f_s$), and some instances of $f_n = |f_s + nf_e|$, as seen in the C_L spectra in Figure 2.5. For post-lock-in, the peak at f_s is more distinct, however, it isn't consistently the second highest peak, instead the second harmonic of f_e is. Harmonics of f_e have significantly greater magnitudes than any frequencies near them, further suggesting the dominance of forcing in this regime. Harmonics of f_s have disappeared, giving way to combination frequencies such as f_n and $f_m = |mF - e - f_s|$, as also seen in Figure 2.5. Overall, the characteristics of these z-vorticity probe spectra are consistent with the behavior thus far established: pre-lock-in is the most aperiodic of the regimes, giving rise to low frequencies with its asymmetric, irregular vortex-structure development; and post-lock-in which is symmetric and periodic to an extent, only due to the dominant influence of the forcing, but tending toward frequent, smaller structures which are regularly dissipated by said forcing.

2.4.5 Influence of Three-Dimensionality

The majority of the work previously done in this area is limited to two-dimensional computations, reasonably assuming that the three-dimensional effects are negligible. Preliminary three-dimensional studies are performed in this work so as to verify the validity of this assumption. As can be seen in Figure 2.4, 3D simulations agree well with the 2D simulations performed on both the P- and ER-grids included in this work. As Figure 2.16 further indicates, this is the case with the force coefficient spectra as well. Identically to Figure 2.5, for these C_L spectra the natural shedding

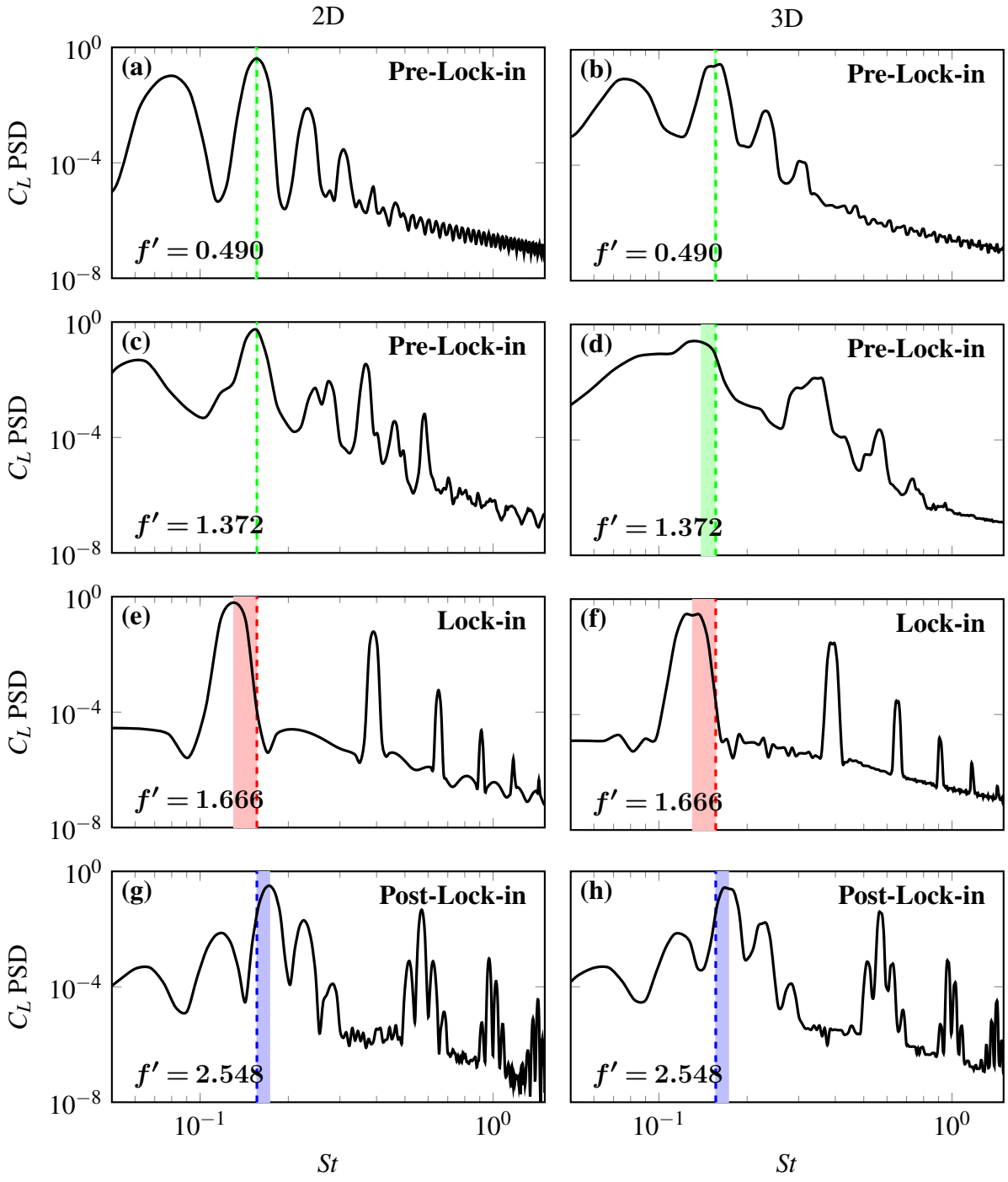

Figure 2.16: Spanwise-averaged lift coefficient power spectra for inline oscillating flow over a square cylinder, as simulated in 2D (left column) and 3D (right column), for a sampling of f': (a,b) $f' = 0.5$; (c,d) $f' = 1.4$; (e,f) $f' = 1.7$; (g,h) $f' = 2.6$. The natural shedding frequency, f_0 is indicated by a dashed line in each plot and the range between f_s and f_0 is highlighted for reference.

frequency, f_0, is indicated by a dashed line and colored: green if the shedding frequency, $f_s \approx f_0$, red if $f_s < f_0$, and blue if $f_s > f_0$. The range between f_s and f_0 is highlighted in the same color. In the pre-lock-in cases it is apparent that the 3D simulations have output smoother spectra, with neighboring peaks tending to become indistinguishable from one another. This is not unexpected as the spanwise-averaging inherent in the C_L calculation will smooth the resulting spectra. This also permits a broader range of frequencies to simultaneously be active and explains why more energy appears to be contained in the frequencies shown. However, the 2D simulations capture the main features of the spectra well, indicating the same peak frequencies excepting the $f' = 1.372$ case, which still exhibits strong similarities between the 2D and 3D spectra. The higher forcing frequencies would also indicate that the agreement of the 2D cases improves with increasing f' as the lock-in and post-lock-in cases are able to capture the various combination frequencies too.

2.5 Conclusions

We performed direct numerical simulations of pulsating flow over a square cylinder for the following parameters: $Re = 200$; $x_e/D = 0.20$; and $0 \leq f_e/f_0 \leq 4$. Over this range of forcing frequencies, the force coefficients and spectra are examined in the three forcing regimes: pre-lock-in, lock-in and post-lock-in. During pre-lock-in, the shedding frequency, f_s, remains equal to the natural shedding frequency, f_0. The corresponding peak in the C_L PSD is one decade larger than that of the neighboring minima, and combination frequencies are observed. The onset of lock-in is very sharp and the corresponding excitation frequency is identified. The lock-in phenomenon reported in literature is observed for $1.6 \leq f_e/f_0 \leq 2.4$. Both the shedding and combination frequencies become functions of the forcing frequency within the lock-in regime, and the corresponding C_L PSD peaks are four decades larger than that of their neighboring minima. In this regime, the $\overline{C_D}$ and C_L' values are notably higher than other regimes. The transition beyond the lock-in regime is shown to be more gradual, with peaks of the spectra broadening until separating into multiple discrete peaks. Here, combination frequencies reemerge. Z-vorticity contours establish a qualitative explanation of the development of the vortex-structures in each regime of interest, providing further insight into the aforementioned statistics. In the pre-lock-in regime, the pulsations interrupt

the natural shedding cycle behavior, being accelerated forward by the surge period of the pulsations. As the sizes and shapes of structures vary greatly due to these influences being out of sync, the shedding frequency remains the same. Upon entering the lock-in regime, the pulsations grow sufficiently strong, causing the SV-structures to be affected by both the recession and surge periods of the pulsations. Although one might expect this to further destabilize the vortex shedding cycle, it instead establishes a natural rhythm in which the structures shed above and below in alternating sequence, amplifying their effect upon the body. As f' increases, the SV-structures are gradually decoupled from interacting with the RV-structures. This leads to a decrease in the effects of forcing in the transitional regime, plateauing in the post-lock-in regime and returning the shedding frequency to the natural shedding frequency. Through the use of probes located off the rear corners of the square cylinder, these qualitative observations of vortex-structure development are then quantitatively linked to the previously described spectra. This then explains the C_L behavior during lock-in. It is also shown that three-dimensionality effects do not significantly affect the frequency range of the three regimes. While two- and three-dimensional spectra do exhibit some differences, the overall flow mechanisms do not appear to be very different. These findings are important for many engineering applications in which structures experience flow-induced vibrations.

3. PARTIALLY-AVERAGED NAVIER-STOKES SIMULATIONS OF TURBULENT FLOW PAST A SQUARE CYLINDER: COMPARATIVE ASSESSMENT OF STATISTICS & COHERENT STRUCTURES AT DIFFERENT RESOLUTIONS

Scale-resolving simulations of the turbulent wake behind a square cylinder are performed at $Re = 22,000$ *using the partially-averaged Navier-Stokes (PANS)* k-ω *closure model at different degrees of resolution (cut-off scales) corresponding to unresolved-to-total kinetic energy ratio* $f_k \in [0.10, 0.50]$. *The two principle objectives of the study are to (i) establish the degree of resolution required for accurate computation of different quantities of interest (QoI) ranging from flow statistics to coherent structures; and (ii) develop a protocol for quantitative assessment and comparison of the large-scale coherent structures simulated at different degrees of resolution. Straight forward use of proper orthogonal decomposition (POD) to assess and compare large-scale coherence at different resolution levels can prove difficult as small-scale features can affect the POD mode shape and amplitude. To overcome this difficulty, two methods of quantifying coherent structures in the wake are proposed. These methods are based upon the incorporation of Fourier and Chebyshev decompositions with spectral proper orthogonal decomposition (SPOD), respectively. We examine first-mode energy spectra and corresponding streamwise mode shapes using the results generated from PANS simulations at different degrees of resolution. It is demonstrated that increasingly finer resolutions are needed for: integral quantities, one-point statistics, frequency spectra and coherent structures, in that order. The underlying physics is explicated.*

3.1 Introduction

The computational effort required to simulate turbulent flows for engineering applications depends upon many factors, including: (i) the inherent complexity of the flow; (ii) the quantities of interest (QoI), which can range from simple integral metrics (for example, coefficient of lift or drag of aerodynamic bodies) to large-scale vortical structures in the wake of an aircraft; and (iii) the prescribed degree of accuracy of QoI prediction. In simple cases such as channel flows and

flat plate boundary layers, many of the key flow statistics of engineering interest can be reasonably computed using elementary turbulence models such as RANS (Reynolds-averaged Navier-Stokes). However, in vortex-dominated flows – including jets, wakes, mixing layers and flows of complex geometry – more refined simulation methodologies are needed. Such flows exhibit intrinsic instabilities, separation, coherent structures and other complicated spatio-temporal features. Accurate computation of these phenomena entails that the large scales of motion be adequately resolved. It is now well understood that direct numerical simulations (DNS) and large eddy simulations (LES) may require excessive computational effort, and are indeed unnecessary if only elementary flow statistics are needed for the application of interest. On the other hand, RANS models are inherently inadequate even for computing elementary statistical features of these complex flows. The scale-resolving simulation (SRS) approach is well suited for these engineering applications wherein the optimal degree of resolution is strongly flow- and application-dependent.

The SRS methodology is founded on the premise that the required computational accuracy of various flow features (QoI) can be accomplished at different degrees of scale-resolution. It is reasonable to expect that satisfactory simulation of coherent structures will require much finer scale-resolution than adequately accurate computation of the mean flow profiles only. The partially-averaged Navier-Stokes (PANS) approach is an SRS method that adapts RANS closure models for subgrid closure for any degree of scale-resolution [77, 78, 79]. The cut-off length-scale (or equivalently the implied filter width) is controlled by the fractions of unresolved-to-total kinetic energy and dissipation. Along with the partially integrated transport modeling (PITM) method [80], PANS is classified as a bridging-SRS method that, in principle, offers the ability to simulate turbulent flows at any degree of resolution between DNS and RANS. Thus, PANS offers a precision-on-demand capability that can be tailored for the flow of interest and the required level of accuracy. As previously mentioned, the degree of resolution (cut-off length-scale) required to adequately capture various flow features is strongly contingent upon the flow under consideration. For different flow categories, it is of much interest to establish the resolution requirements for capturing various flow features.

The first objective of the study is to assess the resolution requirements for QoI of different degrees of complexity in a statistically two-dimensional wake flow. The benchmark case of a flow past a square cylinder at $Re = 22,000$ is considered. Wake flows exhibit important flow phenomena of interest in engineering applications such as massive separation, vortex shedding, secondary instabilities and coherent structures. Experiments and high-fidelity simulations of the flow show a wide variation in the findings rendering the case particularly challenging. Four classes of QoI are considered: (i) integral quantities; (ii) one-point statistics; (iii) temporal (frequency) spectra at important probe locations; and (iv) large-scale coherent structures. PANS simulations at different degrees of resolution (and equivalently different levels of computational effort) are performed. The minimum resolution requirements for each QoI is sought.

The second and equally important objective of the study is to develop a quantitative procedure to assess and compare large-scale coherent structures computed from simulations of different cut-off length-scales. Specifically, we seek a quantitative description of their spatio-temporal characteristics. The standard proper orthogonal decomposition (POD) technique commonly used in other studies of wake-flow coherent structures [81, 82, 83, 84, 85, 86] is not well-suited for this purpose. POD, while able to classify modes on the basis of energy content, does not provide the spatial scale or dynamic description sought in this study. Oftentimes the most energetic modes can contain sizeable contributions from smaller scales of motion obfuscating the large-scale structures. We therefore propose an adaptation of the spectral proper orthogonal decomposition (SPOD) technique [87]. The main novelty is the use of a Chebyshev filter in the cross-stream direction to filter out the contributions of the small scales.

The organization of this paper is as follows: Section 3.2 describes the PANS equations and closure features. Section 3.3 presents a description of the computational approach, problem set-up, flow domain, and details of the grids used. Section 3.4 examines the integral flow parameters, one-point statistics and frequency spectra. The results obtained from simulations of different resolutions are compared against a suite of available data. In Section 3.5, a procedure for the characterization of the coherent structures is proposed. This is followed by a comparison of the key features

of the structures obtained from different simulations of increasing degree of resolution. The paper concludes in Section 3.6 with a brief summary of the main findings.

3.2 Partially-Averaged Navier-Stokes Method

In the PANS method, the instantaneous velocity and pressure fields, V_i and p, are partitioned into resolved fields, U_i and $\langle p \rangle$, and residual fields, u_i and p_u. From the Navier-Stokes equations, the evolution equations can be derived for the resolved quantities [88],

$$\frac{\partial U_i}{\partial t} + U_j \frac{\partial U_i}{\partial x_j} + \frac{\partial \tau(V_i, V_j)}{\partial x_j} = -\frac{\partial \langle p \rangle}{\partial x_i} + \nu \frac{\partial^2 U_i}{\partial x_j \partial x_j}, \tag{3.1}$$

$$\frac{\partial^2 \langle p \rangle}{\partial x_i \partial x_i} = -\frac{\partial U_i}{\partial x_j} \frac{\partial U_j}{\partial x_i} - \frac{\partial^2 \tau(V_i, V_j)}{\partial x_i \partial x_j}, \tag{3.2}$$

where $\tau(V_i, V_j)$ is the generalized central second moment or sub-filter stress (SFS) tensor. This tensor embodies the cumulative effect of the modeled/unresolved/residual scales on the resolved fields. Many levels of closure are possible for the SFS tensor. In this work we employ the Boussinesq approximation [78]:

$$\tau(V_i, V_j) = -2\nu_u S_{ij} + \frac{2}{3} k_u \delta_{ij}, \tag{3.3}$$

where ν_u is the unresolved eddy viscosity, S_{ij} is the resolved strain-rate tensor ($S_{ij} = \frac{1}{2}\left(\frac{\partial U_i}{\partial x_j} + \frac{\partial U_j}{\partial x_i}\right)$), and k_u is the unresolved turbulent kinetic energy.

The PANS cut-off scale is characterized in terms of the filter parameters, f_k and f_ε, which represent the ratio of unresolved-to-total kinetic energy and dissipation, respectively. Equivalently, the unresolved-to-total specific dissipation rate, f_ω, can be defined in terms of these two parameters:

$$f_k \equiv \frac{k_u}{k}; \quad f_\varepsilon \equiv \frac{\varepsilon_u}{\varepsilon}; \quad \text{and} \quad f_\omega = \frac{\omega_u}{\omega} = \frac{f_\varepsilon}{f_k}. \tag{3.4}$$

It is the filter parameter f_k which effectively enables a bridging between DNS and RANS solutions. When $f_k = 1$, the entirety of the turbulent field is modeled (equivalent to a RANS solution). As f_k approaches zero, the unresolved turbulent kinetic energy diminishes and the resolved component

increases. In principle, a fully-resolved DNS can be obtained provided the numerical schemes and spatial resolution are adequate. In this investigation, the value of f_k is varied in the range $f_k \in [0.10, 0.50]$, while f_ε is maintained at unity ($f_\varepsilon = 1$), as dissipation is assumed to be dominant only at the smallest scales for the Reynolds number under consideration.

The PANS k-ω model equations for the unresolved kinetic energy, k_u, and unresolved specific dissipation rate, ω_u, are as follows [89]:

$$\frac{\partial k_u}{\partial t} + U_j \frac{\partial k_u}{\partial x_j} = \tau(V_i, V_j) \frac{\partial U_i}{\partial x_j} - \beta^* k_u \omega_u + \frac{\partial}{\partial x_j} \left[\left(\nu + \frac{\nu_u}{\sigma_{k_u}} \right) \frac{\partial k_u}{\partial x_j} \right]; \tag{3.5}$$

$$\frac{\partial \omega_u}{\partial t} + U_j \frac{\partial \omega_u}{\partial x_j} = \frac{\alpha}{\nu_u} \tau(V_i, V_j) \frac{\partial U_i}{\partial x_j} - \left(\alpha \beta^* - \alpha \frac{\beta^*}{f_\omega} + \frac{\beta}{f_\omega} \right) \omega_u^2 + \frac{\partial}{\partial x_j} \left[\left(\nu + \frac{\nu_u}{\sigma_{\omega_u}} \right) \frac{\partial \omega_u}{\partial x_j} \right]; \tag{3.6}$$

where: $\sigma_{k_u} = \frac{f_k}{f_\omega} \sigma_k$, $\sigma_{\omega_u} = \frac{f_k}{f_\omega} \sigma_\omega$, and the unresolved eddy viscosity, $\nu_u = k_u / \omega_u$. The closure coefficients, as in the standard RANS k-ω model [90], are: $\beta^* = 0.09$, $\alpha = 5/9$, $\beta = 0.075$, $\sigma_k = 2.0$, and $\sigma_\omega = 2.0$. Note that similar equations have been derived for the k-ε model and have been used by others for the flow of interest [91]. However, utilization of the k-ε model necessitates empirical near-wall treatment. Due to its robust near-wall features, the k-ω model was chosen for this work.

The unresolved eddy viscosity can also be rewritten using Eqn. 4.4 (taking $f_\varepsilon = 1$):

$$\nu_u = f_k^2 \frac{k}{\omega} = f_k^2 C_\mu \frac{k^2}{\varepsilon} = f_k^2 \nu_T; \tag{3.7}$$

where ν_T represents the eddy viscosity as would be calculated by RANS schemes.

Ref. [92] shows that PANS can be considered equivalent to DNS of a non-Newtonian fluid, with its spatially-varying viscosity given by $(\nu + \nu_u)$. This lowers the effective Reynolds number with increasing f_k:

$$Re_{eff} = \frac{V_\infty D}{\nu + \nu_u} = \frac{V_\infty D}{\nu + f_k^2 \nu_T}. \tag{3.8}$$

Using Kolmogorov scaling, the smallest resolved scales in a PANS calculation can be estimated as

[92]:

$$\eta_u = \left(\frac{(\nu + f_k^2 \nu_T)^3}{\varepsilon} \right)^{1/4} \quad \text{and} \quad \frac{\eta_u}{L} \sim Re_{eff}^{-3/4}. \tag{3.9}$$

Here, η_u represents the computational Kolomogorov length-scale and L is the characteristic length scale. As f_k decreases, Re_{eff} tends towards Re and η_u is reduced. The key then to a sufficiently accurate PANS simulation becomes ensuring that the filter parameter, f_k, is selected appropriately such that sufficient range of scales are resolved dependent upon QoI and the flow under consideration. Accordingly, it is imperative that Re_{eff} be monitored in regions of interest so as to ensure that the underlying instabilities are resolved [93].

It is important to note that the grid requirement is dependent on the f_k value:

$$f_k \geq 3 \left(\frac{\Delta}{\Lambda} \right)^{2/3}, \tag{3.10}$$

where Δ represents the grid size and $\Lambda = k^{3/2}/\varepsilon$ as shown in Ref. [94]. As mentioned in Section 3.1, a key objective of the work is to determine the value of f_k (and therein Δ) at which different QoI can be computed accurately.

Several studies have assessed the capability of PANS simulations in practical wake flow applications, including: wind turbines [95], marine vessels [96, 97, 98], aircraft landing gear [99], and ground transportation [100, 101, 102]. PANS simulations have proved well suited for capturing QoI in canonical wake flows like those past a circular cylinder [89, 103, 93, 104, 105], a square/rectangular cylinder [91, 106, 107, 108, 109, 110, 111], or a sphere [112]. Many of these studies compare the accuracy of PANS to that of RANS and LES (among other methods) investigating integral quantities and one-point statistics. While some also compare the effects of increasing scale-resolution, a detailed analysis of the resolution requirements of different QoI is not established in literature. Such is the objective of this work.

3.3 Problem Setup and Computational Approach

The benchmark case of flow past a square cylinder is considered at $Re = V_\infty D/\nu = 22{,}000$, where V_∞ is the freestream velocity and D is the cylinder diameter/side length. This statisti-

cally two-dimensional wake flow is analogous to common engineering geometries and features important flow phenomena including: separation, vortex shedding, secondary instabilities, and coherent structures. In a companion study, flow past a sphere is considered [112]. As explained in Section 3.2, it is key for PANS simulations that f_k is sufficiently low so as to facilitate the resolution of the characteristic instabilities. For this work, these instabilities are: (i) the von Kármán vortex-shedding frequency, f_{VS} (typically reported as the Strouhal number, St); and (ii) the Kelvin-Helmholtz (KH) frequency, f_{KH}. The vortex-shedding instability is known to manifest when $Re \geq 50$, whereas the KH instability is known to appear when $Re \geq 1,000$ [24]. In this section, we present details of the computational and numerical issues.

3.3.1 Computational Setup

The flow domain is comprised of a cuboid measuring $30D \times 14D \times 4D$. A schematic of the physical domain is shown in Figure 3.1. The domain utilizes a Cartesian-coordinate system such that the x-, y-, and z-axes align with the streamwise, cross-stream, and spanwise directions, respectively. The origin is located at the center of the square cylinder, while the inlet and outlet are located at $X/D = -10$ and $X/D = 20$, respectively. A spanwise dimension of $4D$ is chosen, consistent with established literature [21, 17, 22, 20, 13, 16, 23, 18]. Furthermore, to investigate the frequency response of the flow, we introduce streamwise velocity probes in eight locations, shown in Figure 3.2. These locations are chosen strategically to investigate the vortex-shedding and KH instabilities.

Uniform freestream velocity, V_∞, is prescribed at the inlet. Zero-normal derivative for pressure and boundary conditions for k_u, ν_u, and ω_u are prescribed at the inlet as follows:

$$k_u = \frac{3}{2}(0.01V_\infty)^2 f_k; \qquad \nu_u = 10\nu\frac{f_k^2}{f_\varepsilon}; \qquad \omega_u = k_u/\nu_u. \tag{3.11}$$

At the surface of the square cylinder, no-slip and no-penetration conditions are applied for the velocity field. Similarly, k_u and ν_u are prescribed at near-zero values and the normal derivative for pressure is taken to be zero. The unresolved specific dissipation at the first grid point at the surface

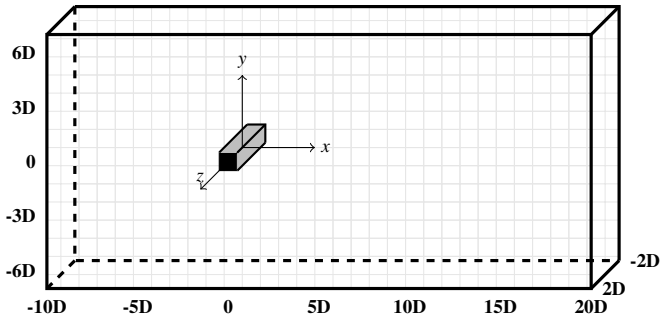

Figure 3.1: Non-dimensional schematic of the physical domain used for all f_k cases for flow past a square cylinder. The domain measures $30D \times 14D \times 4D$; further details are provided in Table 3.1 regarding the computational mesh.

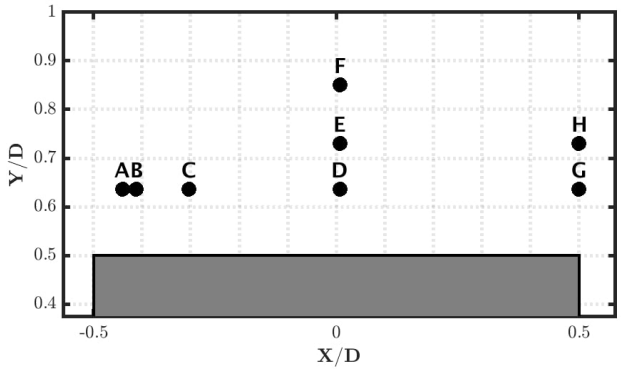

Figure 3.2: Grid convergence study probe locations.

is defined as,

$$\omega_u = \frac{96\nu}{\beta_0 d_{wall}^2} f_\omega, \tag{3.12}$$

following Ref. [113]. A convective boundary condition is applied to the velocity at the outlet, while a fixed-value is applied to the pressure field, and zero-normal derivatives are prescribed for all other variables. For the cross-stream and spanwise planes, slip and periodic boundary conditions are used, respectively.

The finite-volume code OpenFOAM [72] is used for the PANS simulations. Second-order accurate schemes are selected for the spatial discretization, along with a second-order implicit backward scheme for the temporal discretization. The Pressure-Implicit with Splitting of Operators

(PISO) algorithm [73] is used for the coupling of pressure and velocity.

3.3.2 Grid Independence

Given the nature of the PANS technique, a grid which is sufficient for a specific f_k value is also suitable for higher f_k (see Eqn 3.10). For this reason, we first perform a grid independence study for the $f_k = 0.10$ case, employing two meshes: Mesh A and Mesh B. Mesh B implements approximately twice as many degrees of freedom as Mesh A, reducing the cell height from $(\Delta y_A^+)_{min} \approx 9.8$ to $(\Delta y_B^+)_{min} \approx 4.3$ (based upon a priori calculation [114]). Resolution in the spanwise direction is held constant ($\Delta z/D = 0.12$), concentrating the added resolution to the streamwise and cross-stream directions in the near-wake. Representative slices of these meshes are provided in Figure 3.3 with specific details given in Table 3.1. In this section, one-point statistics and frequency spectra are compared to assess grid independence.

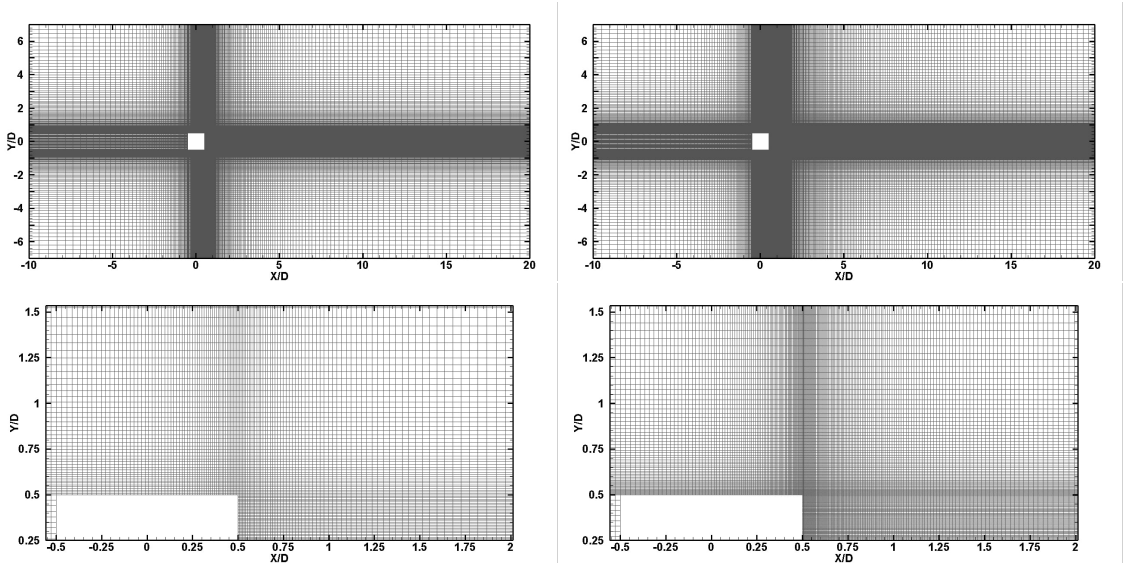

Figure 3.3: XY-plane cross-sections of Mesh A (left column) and Mesh B (right column). Mesh B implements approximately twice as many degrees of freedom than Mesh A; details regarding the computational domain parameters are provided in Table 3.1.

In Figure 3.4, we see reasonable agreement between the two meshes for the mean (spanwise- and time-averaged) one-point statistics shown. The mean streamwise velocity profiles match well,

Table 3.1: Summary of computational domain parameters as compared with literature. L_{X_U} is indicative of the upstream distance from the center of the square cylinder to the inlet-plane; NDOF is the number of degrees of freedom; and $(\Delta y/D)_{min}$ is the minimum cell height tangential to the square cylinder surface.

Reference	Method	Domain	L_{X_U}/D	NDOF$/10^6$	$(\Delta y/D)_{min}$
Mesh A	PANS	$30D \times 14D \times 4D$	10	2.1	8.0×10^{-3}
Mesh B	PANS	$30D \times 14D \times 4D$	10	4.5	3.5×10^{-3}
Trias et al. [16]	DNS	$30.5D \times 54D \times \pi D$	10.5	322.5	1.44×10^{-3}
Verstappen & Veldman [17]	DNS	$27.5D \times 14D \times 4D$	7	3.7	5×10^{-3}
Cao et al. [18]	DNS	$32D \times 25D \times 4D$	9.5	26.7-160.3	7×10^{-4}
Minguez et al. [13]	LES	$19.5D \times 14D \times 4D$	4.5	5.1	1×10^{-1}
Sohankar et al. [22]	LES	$24.2D \times 15.7D \times 4D$	7.9	0.5	8×10^{-3}
Cao & Tamura [23]	LES	$28D \times 24D \times 4D$	8	6.8	5.6×10^{-4}
Fureby et al. [20]	LES	$20D \times 14D \times 4D$	5	0.3	
Rodi [21]	LES	$20D \times 14D \times 4D$	5	0.1-1.5	
Ochoa & Fueyo [19]	LES	$20.5D \times 14D \times 4D$	4.5	0.2	

although the recirculation length decreases slightly from 1.10 to 1.05, from Mesh A to Mesh B, respectively. Similarly, for the normal stress components we see good agreement which improves downstream. It should be noted, however, that the peak streamwise normal stress as calculated on Mesh A does overshoot that of Mesh B by approximately 12%.

We then compare eight streamwise velocity probe spectra which are located above the square cylinder (see Figure 3.2). The results from this comparison show excellent agreement for all probe locations, with the exception of the characteristics of the KH frequency (f_{KH}) seen in Figures 3.5(a-c). The Mesh A results tend toward a slightly lower f_{KH}, with a more gradual decline beyond this threshold.

Overall, it seems that the results of the $f_k = 0.10$ simulations performed using Mesh A and Mesh B are in accordance. All other simulations ($f_k = 0.20, 0.30, 0.50$) are performed using Mesh A and the results of the $f_k = 0.10$ simulation performed on Mesh B will be used throughout the remainder of this work.

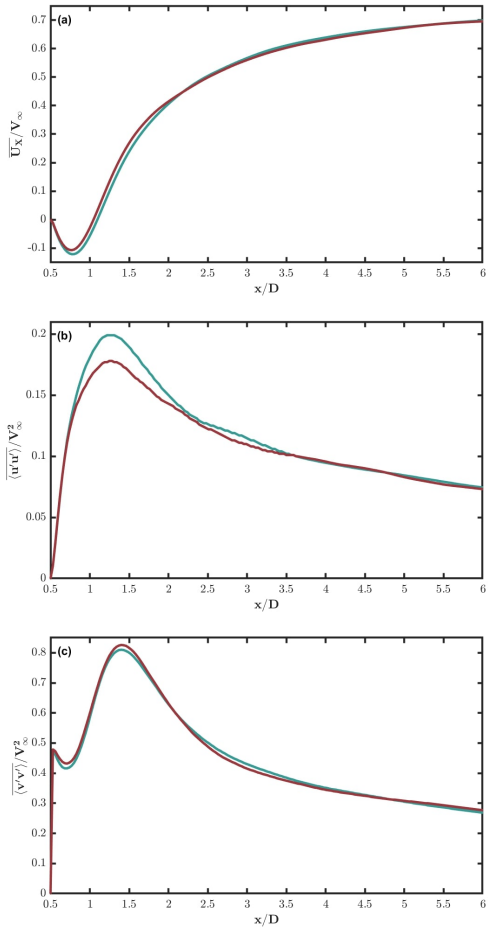

Figure 3.4: Grid independence study using $f_k = 0.10$ performed on Mesh A [–] and Mesh B [–]. Mean streamwise centerline profiles are plotted for: **(a)** streamwise velocity, $\overline{U_X}$; **(b)** streamwise normal Reynolds stress, $\overline{\langle u'u'\rangle}$; and **(c)** cross-stream normal Reynolds stress, $\overline{\langle v'v'\rangle}$.

3.4 Statistical Analysis

The first objective of the study is to assess the resolution requirements for various QoI of different degrees of complexity in this statistically two-dimensional wake flow. For the benchmark case of flow past a square cylinder at $Re = 22{,}000$, experiments and high-fidelity simulations show a wide variation in their findings rendering the flow particularly challenging (see Table A.1). Literature commonly offers three QoI categories which are directly compared in this section: (i) integral quantities; (ii) one-point statistics; and (iii) frequency spectra at important probe locations. The largest permissible f_k value for each QoI is sought.

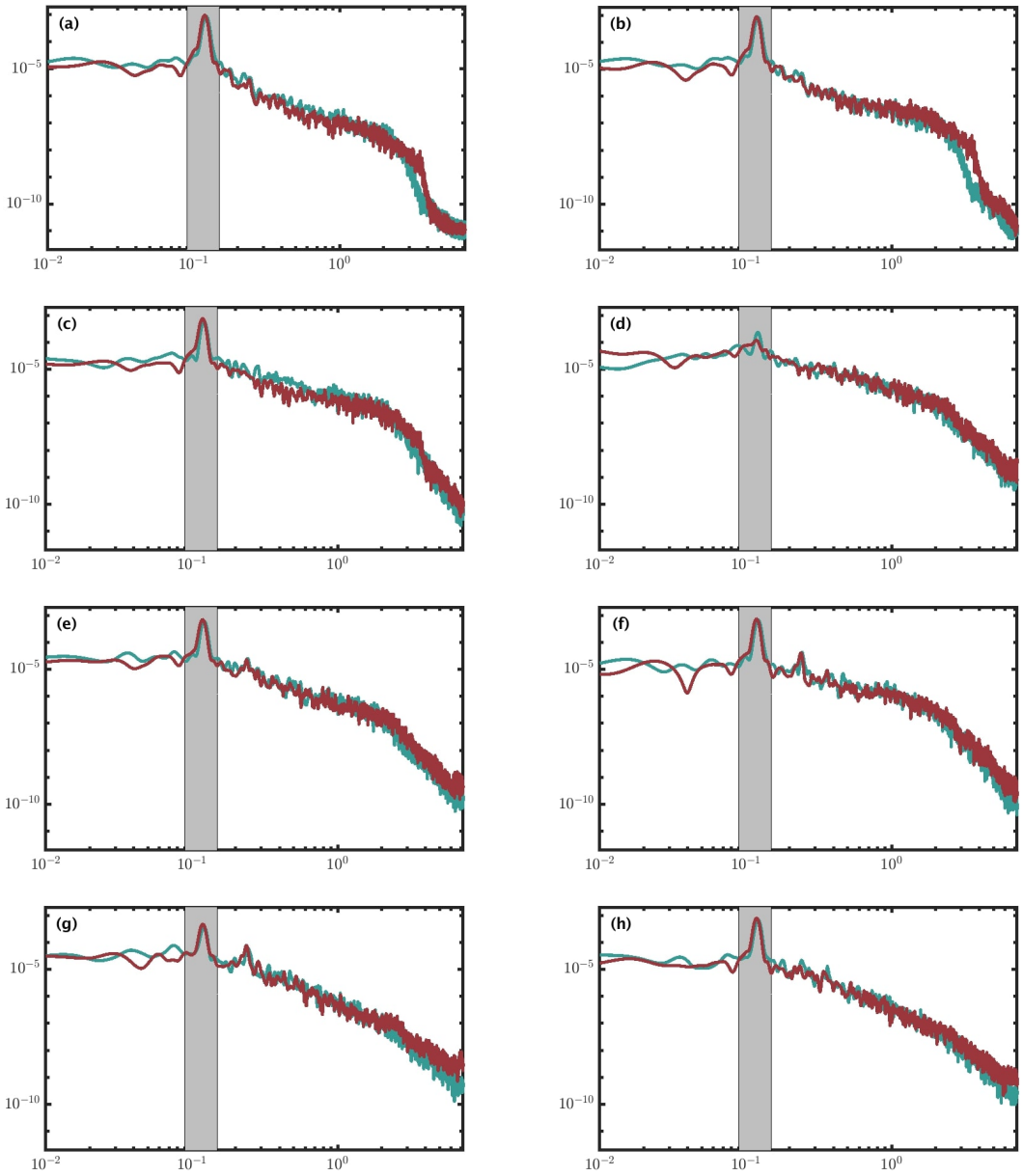

Figure 3.5: Grid independence study using $f_k = 0.10$ performed on Mesh A [–] and Mesh B [–]. Select probe spectra calculated from the fluctuating streamwise velocity are shown for: **(a-h)** probe locations A-H, respectively, as shown in Figure 3.2. The light grey band highlights the reported values for *St* as can be found in Table A.1.

3.4.1 Integral Quantities

Throughout literature, five integral quantities are typically reported: (i) Strouhal number, St; (ii) mean drag coefficient, $\overline{C_D}$; (iii) root-mean-square lift coefficient, C_L'; (iv) root-mean-square drag coefficient, C_D'; and (v) the recirculation length, L_R (based upon the mean streamwise velocity). Each QoI provides important insight into forces and frequencies experienced by the body. Figure 3.6 illustrates the variation in the values of these QoI along with the ranges of comparable literature. A complete tabulation of the integral quantities shown in this study is provided in Table A.1 (Appendix A.1).

All of the cut-off scales analyzed in this study provide sufficient accuracy for the integral quantities assessed. Minimal deviation is observed for St for all cases sharing a vortex-shedding frequency near $St = 0.12$, well within the range seen by LES ($St = 0.09$-0.15), and only slightly less than that seen in experiments and DNS ($St = 0.123$-0.134). In Figure 3.6a and Figure 3.6b, we see that the integral quantities relating to the streamwise forces upon the body ($\overline{C_D}$, C_D') reach some maximum for $0.30 \leq f_k \leq 0.50$. The remaining integral quantities in Figure 3.6 vary monotonically with increased scale-resolution; Figure 3.6c and Figure 3.6d (C_L' and L_R) each appear to asymptotically approach the highest and lowest values of the range seen by DNS studies, respectively.

Overall, $f_k \leq 0.50$ exhibits sufficient accuracy for the aforementioned QoI. This suggests that integral quantities depend largely on the vortex-shedding phenomenon. As long as vortex-shedding is resolved, the quantities are adequately estimated.

3.4.2 One-Point Statistics

We now turn our attention to first- and second-order one-point statistics along the centerline. Figure 3.7 contains results from all PANS simulations for mean (spanwise- and time-averaged) (a) streamwise velocity, $\overline{U_X}$, (b) streamwise normal Reynolds stress, $\overline{\langle u'u' \rangle}$, and (c) cross-stream normal Reynolds stress, $\overline{\langle v'v' \rangle}$. The PANS results are compared against the experimental results of Ref. [12] and the DNS results of Ref. [16].

In Figure 3.7a, we see good agreement with DNS for the streamwise velocity in the near-

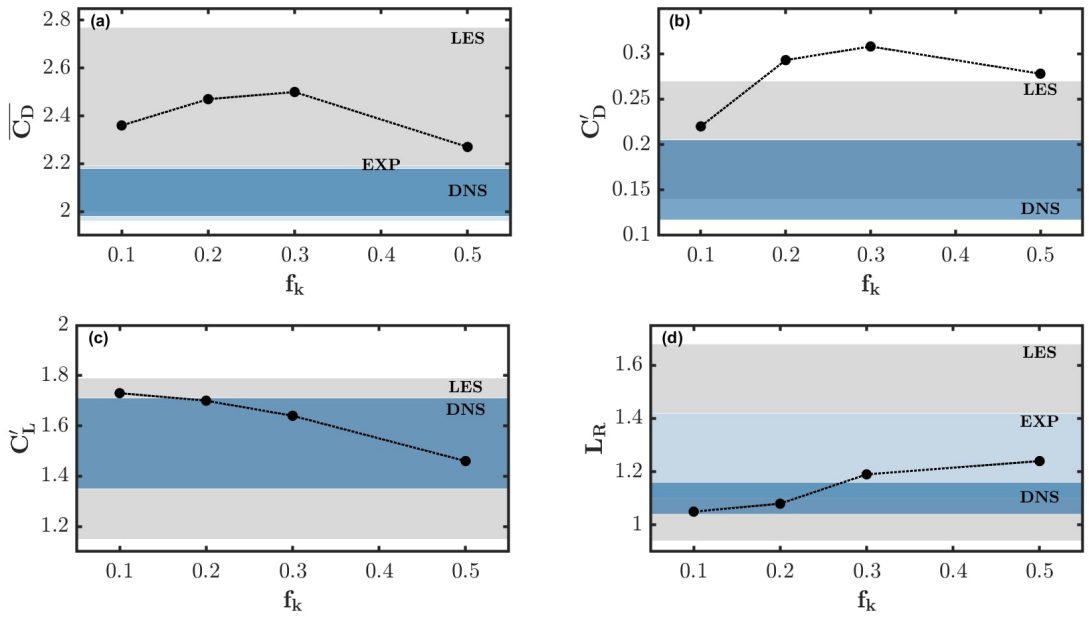

Figure 3.6: Integral quantities as a function of scale-resolution, including: **(a)** mean drag coefficient, $\overline{C_D}$; **(b)** root-mean-square drag coefficient, **(c)** C'_D; root-mean-square lift coefficient, C'_L; and **(d)** the recirculation length, L_R. Results of this study are compared with experiments [11, 12, 13, 14, 15] [ ], DNS [16, 17, 18] [ ], and LES [19, 20, 13, 21, 22, 23] [ ]. A detailed tabulation of these values is included in Appendix A.1 (Table A.1).

wake region ($0.50 < X/D < 1.25$) for $f_k \leq 0.20$. Similar trends are seen for $f_k \geq 0.30$, but with expanding recirculation regions (as detailed in Table A.1). Continuing downstream, streamwise velocity recovery behaves consistently for $f_k \leq 0.30$, with recovery occurring more quickly with increased scale-resolution. These results, however, still fall within the acceptable range between DNS and experiment. This remains the case for $1.5 < X/D < 4$, beyond which PANS simulations begin to overshoot the DNS values, likely owing to the increasing coarseness of the grid. For reference, the cell size for Mesh A and Mesh B is $\Delta x/D = 0.039, 0.021$ at $X/D = 1.5$ and $\Delta x/D = 0.117, 0.067$ at $X/D = 4$, respectively.

In Figure 3.7b and Figure 3.7c we see similar trends for simulations of $f_k \leq 0.30$. While the PANS results overshoot the peak for $\overline{\langle u'u' \rangle}$, the peaks do converge toward the DNS solution with increasing scale-resolution. The peak for the $f_k = 0.10$ case being approximately 15% greater than that of DNS, as opposed to 43-57% for $f_k \geq 0.20$. Likewise, for $\overline{\langle v'v' \rangle}$ we see that with increasing

scale-resolution, the solutions trend toward the representative DNS, showing much better agreement in the near-wake than its streamwise counterpart. While the peak of the $f_k = 0.10$ simulation agrees quite well with DNS, for all $f_k \leq 0.30$ the peak value is within 7%.

The distinct change in behavior for $f_k \leq 0.30$ from the $f_k = 0.50$ simulation is evident upon review of the first- and second-order one-point statistics. In each of the profiles shown, trends appear consistent for $f_k \leq 0.30$, continuing to approach DNS with further scale-resolution. Again, this suggests that the increased scale-resolution which triggers the KH instability is the key factor in the change in these profiles. Development of KH vortices accelerates the transition into turbulence and thereby reduces the resulting recirculation region.

3.4.3 Probe Spectra

We now directly assess the resolution of underlying instabilities. Again, the primary instabilities for the flow past a square cylinder are the von Kármán vortex-shedding and the Kelvin-Helmholtz (KH) instabilities. For reference, the inflection lines of the mean streamwise velocity are shown in Figure 3.8 for each f_k case along with the probe locations used in Figure 3.9 (and shown relative to probe locations found in literature [16, 13, 23]).

At all probe locations included in Figure 3.9, excellent agreement is seen for all f_k values at the primary peak in the spectra, indicative of the vortex-shedding frequency (f_{VS}). The value captured in each also lies well within the bounds of the values seen throughout the literature. The probe spectra shown in Figure 3.9(a-c) come from points at $X/D = -0.44, -0.41, -0.30$ and $Y/D = 0.64$, corresponding with similarly placed probes from Refs. [16, 13], and are centered about the inflection line of all cases, as can be seen in Figure 3.8. There is clear evidence of the KH instability in these spectra, indicated by the sharp decline in energy. For the $f_k = 0.10$ simulation, this would indicate $f_{KH} \approx 3.6$, which is in agreement with a broadband frequency peak reported in Ref. [13] using LES. The $f_k = 0.20, 0.30$ simulations indicate $f_{KH} \approx 2.1$, which agrees better with the other LES results of Refs. [13, 23], reporting $f_{KH} = 2$ and $f_{KH} \approx 1.92 - 2.21$, respectively. The value of f_{KH} reported in literature is quite varied. The DNS results of Ref. [16] report a slightly higher value of $f_{KH} \approx 8$, and similarly the experimental results of Ref. [13] with

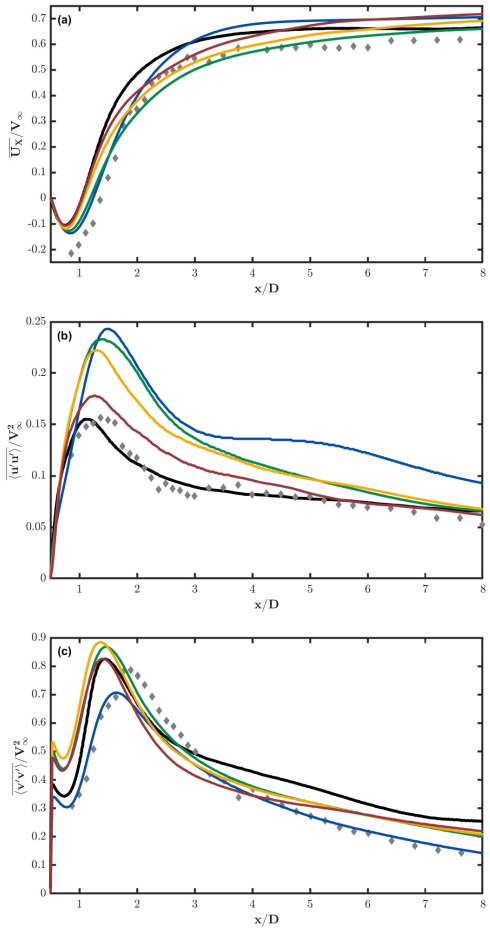

Figure 3.7: Mean streamwise centerline profiles for: **(a)** streamwise velocity, $\overline{U_X}$, **(b)** streamwise normal Reynolds stress, $\overline{\langle u'u'\rangle}$, and **(c)** cross-stream normal Reynolds stress, $\overline{\langle v'v'\rangle}$. All f_k values are represented as follows: $f_k = 0.50$ [–]; $f_k = 0.30$ [–]; $f_k = 0.20$ [–]; $f_k = 0.10$ [–]; and are compared against DNS [16] [–] and experiment [12] [♦].

$f_{KH} \approx 6$ (although for $Re = 27{,}000$). Figure 3.9d and Figure 3.9g also correspond with probes provided in Ref. [16], however, these results show influences of the KH instability, while this is not noted in the compared literature.

The ability of the PANS simulations to capture KH breakdown is dependent on the computational (effective) Reynolds number resulting from the prescribed value of f_k. By reviewing the inflection line of each simulation (shown in Figure 3.8), it is seen that the different f_k simulations behave in a similar fashion (above and below the square cylinder) until $X/D = 0$, corresponding to the streamwise center of the cylinder. The laminar-like flow in this region indicates that the

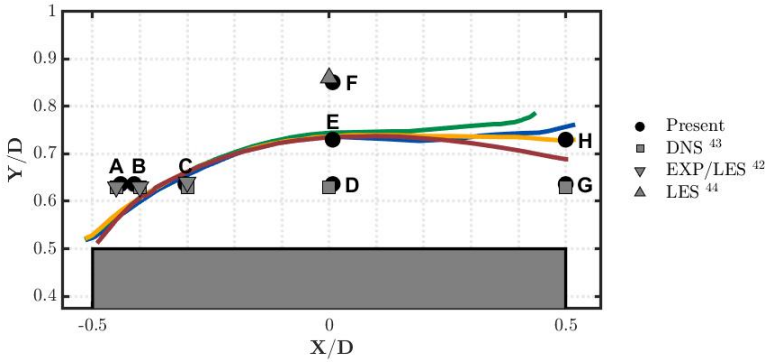

Figure 3.8: Inflection lines $\left(\frac{\partial^2 \overline{U_X}}{\partial y^2} = 0\right)$ for all f_k values as follows: $f_k = 0.50$ [–]; $f_k = 0.30$ [–]; $f_k = 0.20$ [–]; $f_k = 0.10$ [–]. Probe locations of the present study are shown along with those from available literature [16, 13, 23].

KH instability has not yet set in. Beyond this point, the KH instability breaks down at different locations for different f_k simulations. Due to the lower computational (effective) Reynolds number in the higher f_k-value simulations, the KH instability sets in rapidly. In the lower f_k-value simulations, the various stages of perturbation growth are resolved in greater detail leading to a more gradual and physically reasonable development of the various stages of breakdown. This is further corroborated by the Re_{eff} contours included in Appendix A.2 (Figure A.1).

Overall, good agreement is exhibited for low frequencies, especially f_{VS}, for $f_k \leq 0.50$. For higher frequencies we see the direct effect of the increased scale-resolution. At every probe location, there is increased energy in the higher frequencies (smaller time-scales), in addition to the KH instability. In order to clearly capture f_{KH}, $f_k < 0.30$ is required. This is also supported by the review of the Re_{eff} contours in Figure A.1 which has been included in Appendix A.2.

3.5 Analysis of Coherent Structures

The second objective of the study is to develop a quantitative procedure to assess and compare large-scale coherent structures computed from simulations of different cut-off length-scales. Several variations of POD have been utilized to characterize coherent structures in wake flows over the decades [115, 116, 117, 118]. In particular, snapshot POD [119] can accomplish this quite

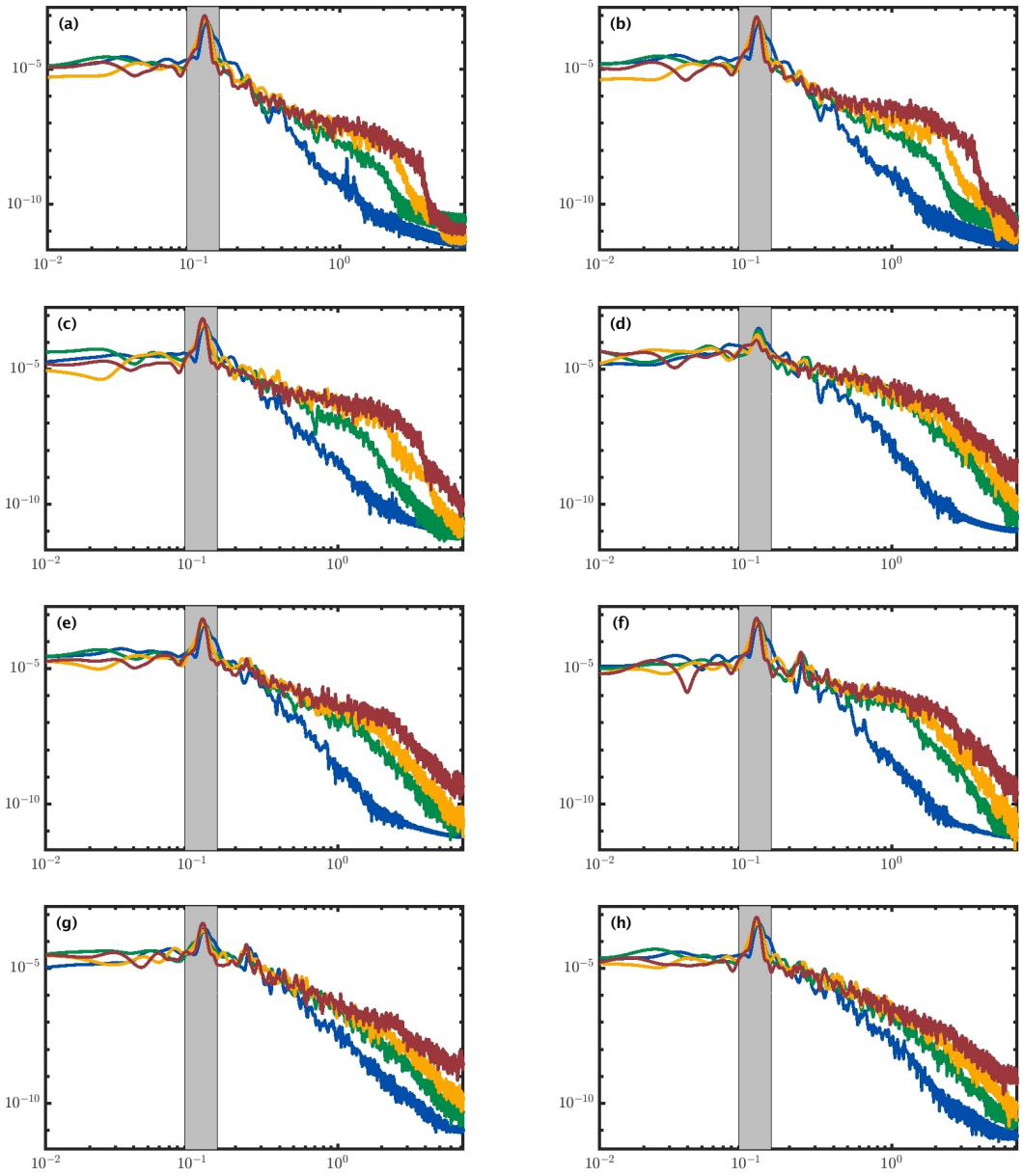

Figure 3.9: Select probe spectra calculated from the fluctuating streamwise velocity are shown for: **(a-h)** probe locations A-H, respectively, as shown in Figure 3.8. All f_k values are represented as follows: $f_k = 0.50$ [–]; $f_k = 0.30$ [–]; $f_k = 0.20$ [–]; $f_k = 0.10$ [–]. The light grey band highlights the reported values for St as can be found in Table A.1.

efficiently in both two- and three-dimensions [81, 82, 83, 84, 85, 86]. However, direct application of such techniques is not viable in this endeavor as the most energetic POD modes often contain contributions from smaller scales of motion obfuscating the large-scale structures. While the use of POD (and similar variants) is ideal for predictive reconstructions of various flows, use of modal analysis in this vein is beyond the scope of this work and will be addressed separately in the future. A quantitative description of the coherent structures is sought rather than a qualitative one.

A methodology which allows for greater specificity is spectral POD [87] (SPOD). SPOD is a variation which allows for the separation of frequencies within POD modes, partially resolving the issue of small-scale infiltration, via discrete Fourier transform (using a form of Welch's method [71]). In practice, this is similar to Dynamic Mode Decomposition [120] (DMD), although SPOD offers enhanced optimization due to the incorporation of Welch's method. In order to further isolate large-scale structures, we perform an additional transform in the cross-stream direction. This pre-filtering of the field in the cross-stream direction allows for isolation of structures of discrete wavelengths. This method has been adapted for the case of axisymmetric wakes by others [112], incorporating a Fourier filter in the azimuthal direction per the work of Ref. [121]. However, in this instance, use of a Fourier filter relies on the inherent periodicity afforded by this geometry. In this work, we seek to determine whether such a filtering procedure would be useful in identifying coherent structures. Additionally, novel use of a Chebyshev filter in the cross-stream direction is examined for comparison. For the purposes of this study, we will refer to these methods as Fourier- and Chebyshev-SPOD (FSPOD and CSPOD), respectively. This methodology allows for a more detailed analysis of scales – spatially and temporally – providing a quantitative description of structure, beyond the scope of traditional POD. Use of POD and DMD are still of value for reduced-order reconstruction and will be analyzed in future work.

3.5.1 Methodology

The large-scale coherent structure isolation and identification is now detailed.

Step 1: Collection of field data at representative XY-planes of the domain at regular intervals of

time. For this study, snapshots were collected for $\Delta t^* = \Delta t V_\infty / D = 0.06875$ over a window of $T^* \approx 400 - 550$, depending on the value of f_k.

Step 2: Interpolation of the field to a uniform grid and removal of the mean field. The uniform grid in this study spanned the area immediately behind the cylinder, $0.5 \leq X/D \leq 7.5$ and $-7 \leq Y/D \leq 7$, in increments of $\Delta x/D = \Delta y/D = 0.05$.

Step 3: Calculation of either the Fourier decomposition (for FSPOD) or the Chebyshev polynomial decomposition [122] (for CSPOD) in the y-direction at every streamwise station and for each time step. These processes yield vectors $\hat{u}$ (Fourier) and $\breve{u}$ (Chebyshev) as follows:

$$\hat{u}(x,m,t) = \frac{1}{14D} \int_{-7D}^{7D} u(x,y,t) e^{-imy} dy; \tag{3.13}$$

$$u(x,y,t) = \sum_{m=0}^{M} \breve{u}_m(x,t) T_m(y); \tag{3.14}$$

where $T_m(y) = \cos(m \cos^{-1}(y))$ is a Chebyshev polynomial of the first kind.

Step 4: Generation of streamwise FSPOD/CSPOD mode shapes with respective energy content at various frequencies by inputting the content of $\hat{u}$ or $\breve{u}$ pertaining to a specified coefficient of the decomposition, m, into the SPOD algorithm [87].

3.5.2 FSPOD Results

Modal energy spectra and mode shapes for each specific frequency corresponding to cross-stream Fourier mode, m, are determined. Figure 3.10 shows the first-mode ($N = 1$) spectra for all f_k simulations for a set of wavelengths (length-scales). The following observations are made:

(i) for all f_k simulations, there is consistent agreement for the large time-scales ($St \leq \mathscr{O}(10^{-1})$) at each length-scale;

(ii) the primary peak at the vortex-shedding frequency (f_{VS}) is observed for most length-scales;

(iii) for a given length-scale, further small time-scales are resolved with decreasing f_k value; and

(iv) for a given small time-scale ($St \geq \mathcal{O}(10^{-1})$), energy content increases with decreasing length-scale and f_k value.

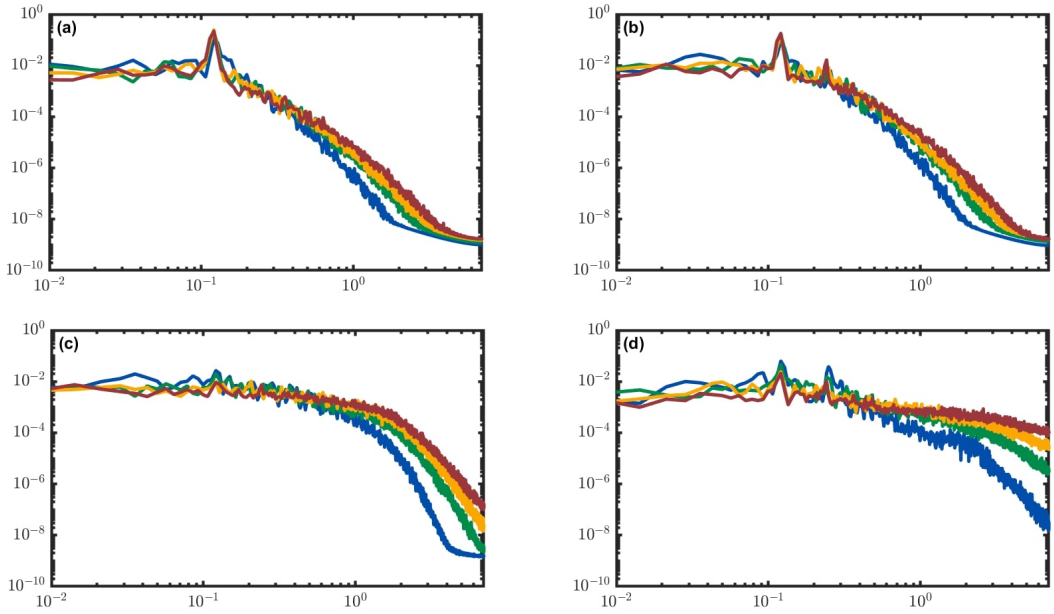

Figure 3.10: FSPOD first-mode ($N = 1$) energy spectra for different f_k simulations for wavelengths: **(a)** $\lambda/D = 14$; **(b)** $\lambda/D = 3.5$; **(c)** $\lambda/D = 0.5$; and **(d)** $\lambda/D = 0.125$. All f_k values are represented as follows: $f_k = 0.50$ [–]; $f_k = 0.30$ [–]; $f_k = 0.20$ [–]; $f_k = 0.10$ [–].

The vortex-shedding frequency (f_{VS}) is the most energetic at long wavelengths. We plot the streamwise mode shapes at f_{VS} for various wavelengths in Figure 3.11. From the largest wavelength, $\lambda/D = 14$ (Figure 3.11a), to $\lambda/D = 1.56$ (Figure 3.11d) we see excellent agreement for all f_k simulations with minimal variation downstream. Between $\lambda/D = 1.56$ and $\lambda/D = 1.27$ this agreement breaks down, although general peaks/trends remain consistent. This quantifies the intent behind the PANS methodology, substantiating the evidence seen in the energy spectra: large-scale structures are consistently captured across all f_k while small-scale structures manifest only as f_k is reduced.

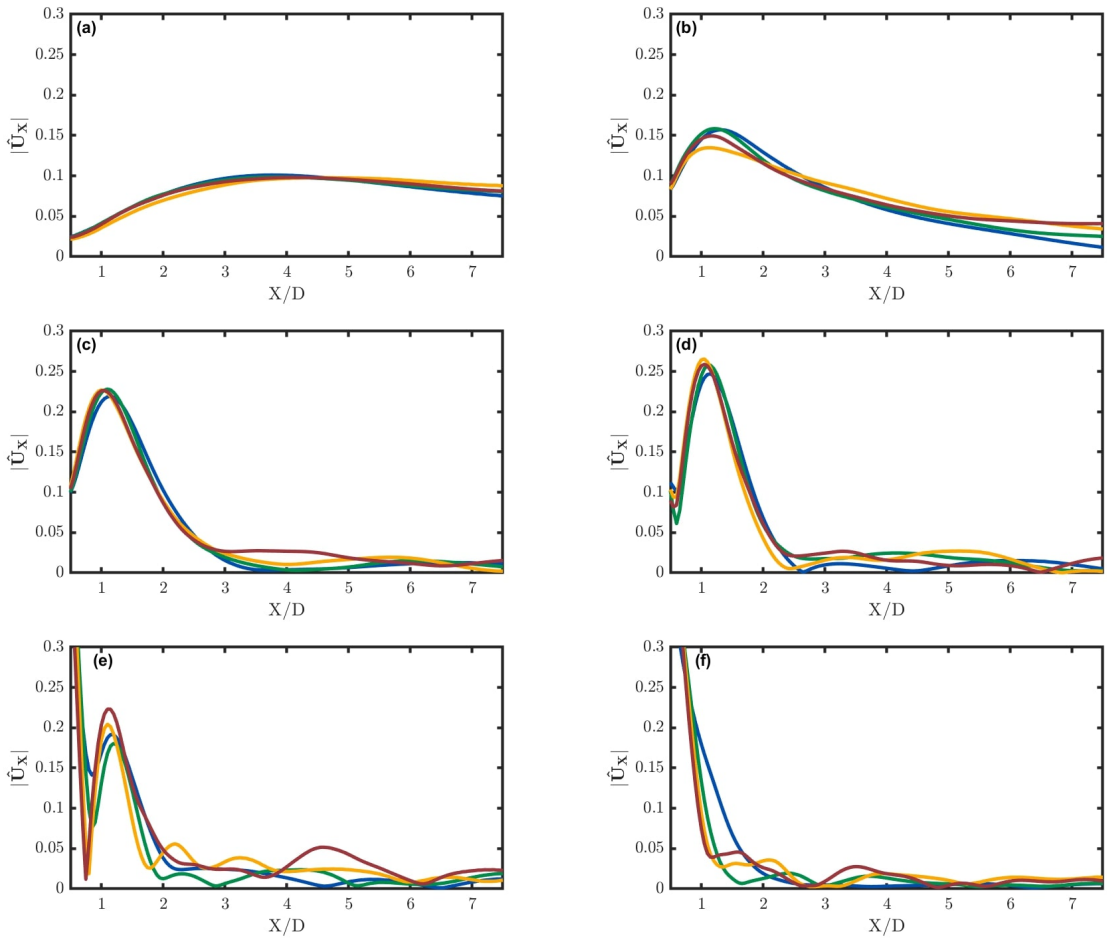

Figure 3.11: FSPOD first-mode ($N = 1$) shape at f_{VS} for different f_k simulations for wavelengths: **(a)** $\lambda/D = 14$; **(b)** $\lambda/D = 3.5$; **(c)** $\lambda/D = 2$; **(d)** $\lambda/D = 1.56$; **(e)** $\lambda/D = 1.27$; and **(f)** $\lambda/D = 1$. All f_k values are represented as follows: $f_k = 0.50$ [–]; $f_k = 0.30$ [–]; $f_k = 0.20$ [–]; $f_k = 0.10$ [–].

3.5.3 CSPOD Results

A key difference between the analogous Fourier and Chebyshev decompositions is the spatial variation of their basis functions. Fourier decomposition assumes that the field is inherently periodic, whereas Chebyshev analysis accounts for non-periodic finite-domain effects. Due to these distinctions, the spatial variation is not fixed for the Fourier basis functions, while those of the Chebyshev basis functions alternate between symmetry and asymmetry relative to the centerline. As the primary vortex-structures shed in an asymmetric pattern, the results for the symmetric- and asymmetric-basis functions of CSPOD have been included separately.

First-mode ($N = 1$) energy spectra are presented for symmetric- and asymmetric-basis functions (corresponding to similar wavelengths as those shown in the previous section) in Figure 3.12 and Figure 3.13, respectively. The symmetric-basis function spectra do not exhibit distinct peaks, although the second harmonic of f_{VS} does manifest intermittently. The asymmetric-basis function spectra, however, consistently show peaks at f_{VS} for all f_k values. Similar to the results seen from FSPOD, there is a clear range of frequency for which all f_k values exhibit excellent agreement (i.e. $St \leq \mathcal{O}(10^{-1})$ for $f_k \leq 0.50$), and beyond which energy increases with further scale-resolution.

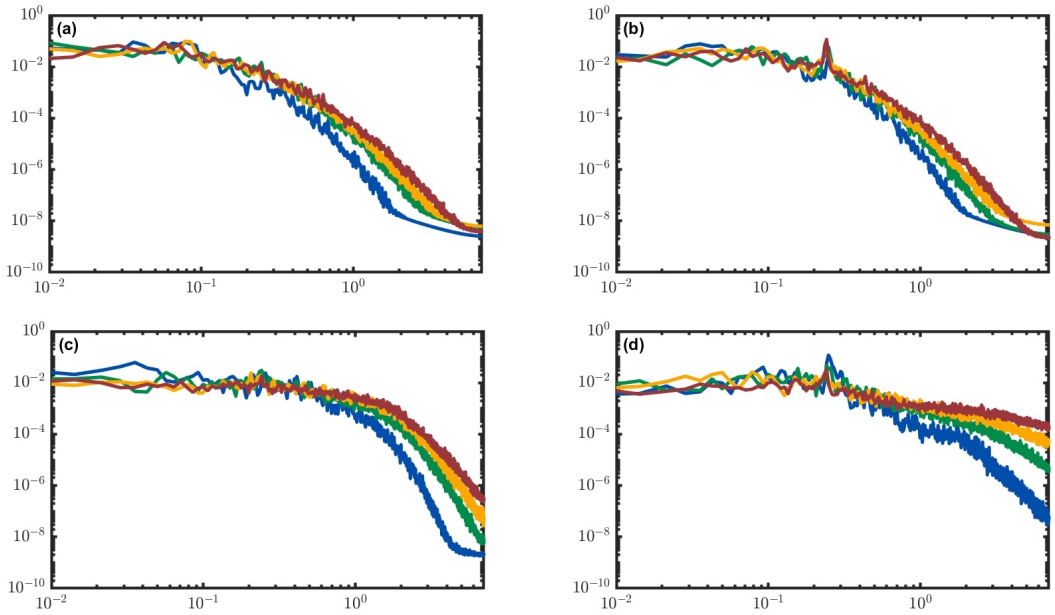

Figure 3.12: CSPOD first-mode ($N = 1$) energy spectra for different f_k simulations for symmetric-basis functions at various wavelengths: **(a)** $\lambda/D = 14$; **(b)** $\lambda/D = 3.5$; **(c)** $\lambda/D = 0.5$; and **(d)** $\lambda/D = 0.125$. The f_k values are represented as follows: $f_k = 0.50$ [–]; $f_k = 0.30$ [–]; $f_k = 0.20$ [–]; $f_k = 0.10$ [–].

We next review streamwise mode shapes at f_{VS} for various asymmetric-basis function wavelengths in Figure 3.14 (corresponding to the wavelengths shown in the previous section). Note that the symmetric-basis function wavelengths have not been included as the energy content at f_{VS} was significantly lower than their asymmetric-basis function counterparts. The mode shapes shown in

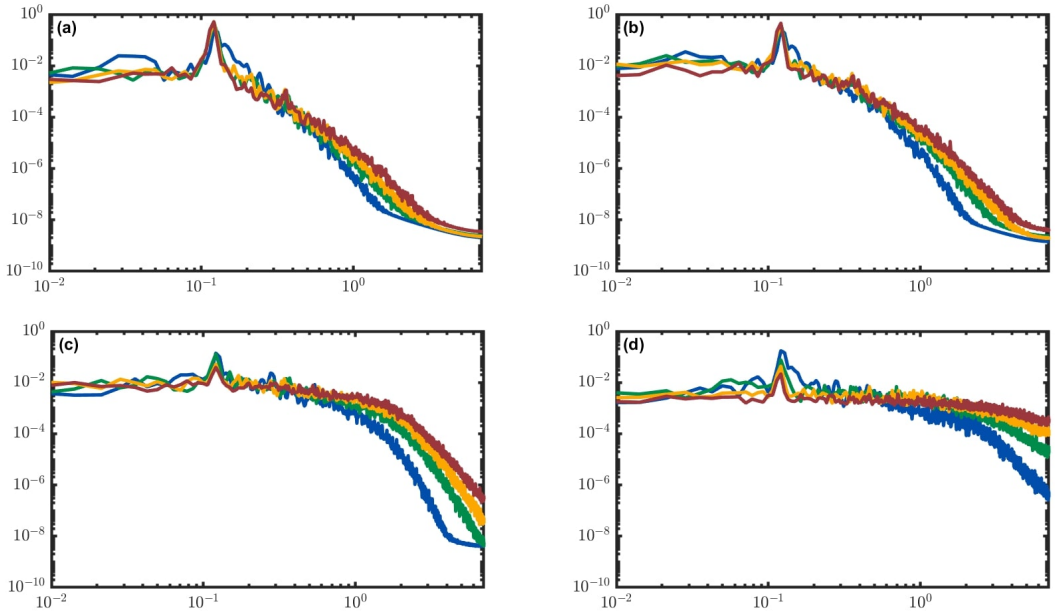

Figure 3.13: CSPOD first-mode ($N = 1$) energy spectra for different f_k simulations for asymmetric-basis functions at various wavelengths: **(a)** $\lambda/D = 9.33$; **(b)** $\lambda/D = 3.11$; **(c)** $\lambda/D = 0.49$; and **(d)** $\lambda/D = 0.124$. The f_k values are represented as follows: $f_k = 0.50$ [–]; $f_k = 0.30$ [–]; $f_k = 0.20$ [–]; $f_k = 0.10$ [–].

Figure 3.14 agree quite well across f_k, exhibiting trends which are similar to those shown in Figure 3.11 for FSPOD. For longer wavelengths, a consistent trend is observed converging to a particular form with decreasing f_k. Similar to the results of FSPOD, the asymmetric-basis function results of CSPOD seem to degrade near $\lambda/D \approx 1$, although Figure 3.14e shows similar mode shapes for $f_k \leq 0.30$. Again, we see the effect of the filter parameter, f_k, quantified by these results, demonstrating the consistency of the large-scale coherent structures with some degradation at smaller length-scales.

It is evident that the FSPOD and CSPOD approaches presented in this section are well suited to isolate and quantify the characteristics of large-scale coherent structures. It is also clearly established in this section that PANS simulations at various f_k values capture the large structures accurately. With decreasing f_k, even the small scale behavior is adequately represented.

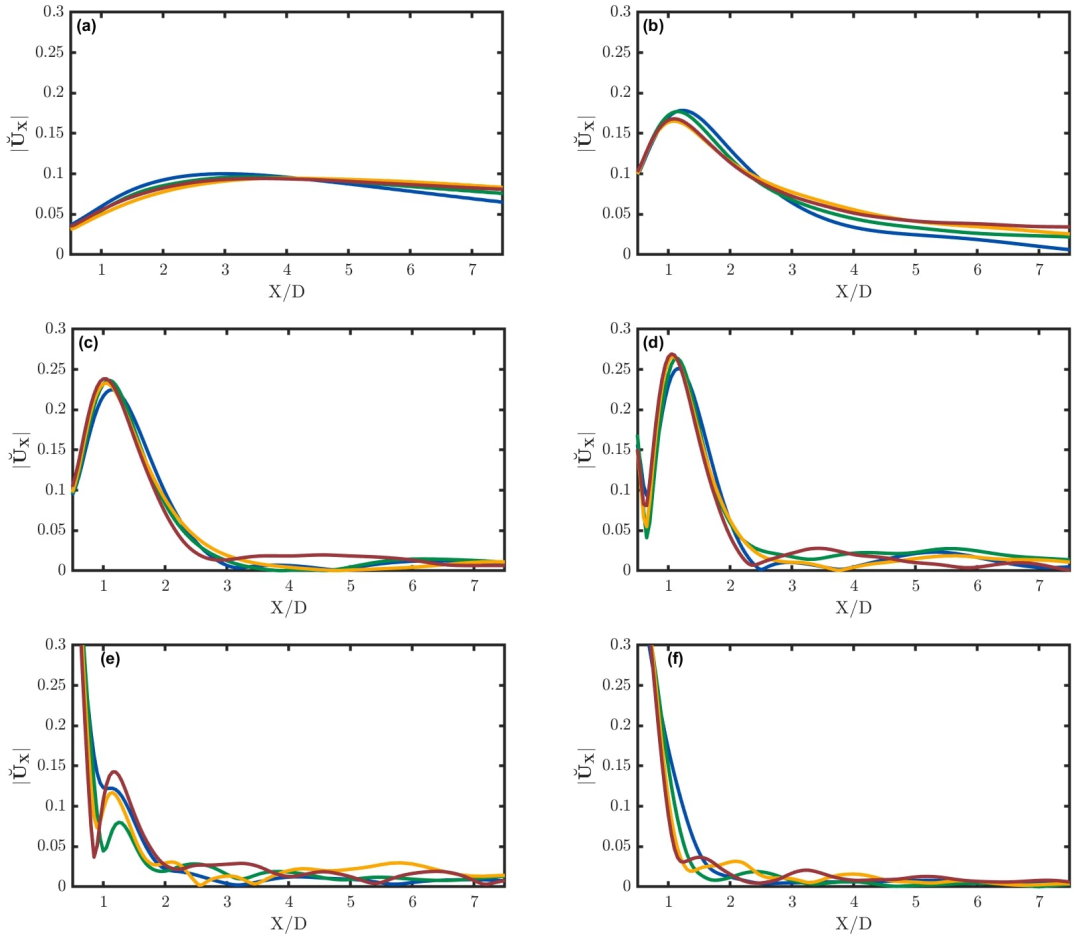

Figure 3.14: CSPOD first-mode ($N = 1$) shape at f_{VS} for different f_k simulations for asymmetric-basis function wavelengths: **(a)** $\lambda/D = 9.33$; **(b)** $\lambda/D = 3.11$; **(c)** $\lambda/D = 1.87$; **(d)** $\lambda/D = 1.47$; **(e)** $\lambda/D = 1.22$; and **(f)** $\lambda/D = 0.97$. All f_k values are represented as follows: $f_k = 0.50$ [–]; $f_k = 0.30$ [–]; $f_k = 0.20$ [–]; $f_k = 0.10$ [–].

3.6 Conclusions

Scale-resolving simulations (SRS) of turbulence aim to provide an optimal balance between computational effort and accuracy, depending upon the complexity of the flow physics and the prescribed degree of accuracy of QoI. The first objective of the study is to establish the optimal degree of resolution (cut-off scale) required for computing different QoI in an archetypal wake flow. The second objective of the study is to formulate a procedure for quantitative assessment of large-scale coherent structures enabling precise comparison of features from different SRS computations. This

study employs the partially-averaged Navier-Stokes (PANS) technique – a bridging-SRS approach – in which the degree of scale-resolution is controlled by the ratio of unresolved-to-total kinetic energy ratio, f_k. The flow past a square cylinder at $Re = 22,000$ serves as the benchmark wake flow. As is typical in most bluff body wakes, this flow exhibits two important instabilities – von Kármán vortex-shedding (VS) and Kelvin-Helmholtz (KH) – which drive further complexities in the flow. PANS simulations are performed employing the k-ω closure for a variety of cut-off scales characterized by $f_k \in [0.10, 0.50]$.

The main findings of the study are summarized:

(i) The global flow parameters such as the Strouhal number and the coefficients of drag and lift are first investigated. It is found that even the $f_k = 0.50$ simulation achieves results within the range seen for comparable LES, while the lower f_k simulations tend toward DNS results. Thus, accurate results are obtained at a very reasonable cost. The underlying reason is that these flow features are almost exclusively dependent on the vortex-shedding phenomenon. For adequately computing these parameters, it suffices to capture the vortex-shedding frequency (f_{VS}).

(ii) Mean streamwise velocity and normal Reynolds stress profiles along the centerline show gradual improvement with increasing scale-resolution. Evidently, these statistics are dependent upon flow phenomena other than vortex-shedding, such as the KH instability.

(iii) At all resolutions the vortex-shedding frequency, f_{VS}, is captured very accurately. Even the spectral energy density is similar for all simulations. However, the Kelvin-Helmholtz frequency is not well replicated by coarse resolution simulations ($f_k > 0.3$). The best agreement with LES [13] is found in the $f_k = 0.10$ simulation and reasonable agreement in the $f_k = 0.20$ and 0.30 simulations is found with other LES results [13, 23], as well. It is demonstrated that the effective (computational) Reynolds number for the coarse resolution simulations is below the critical value required for the onset of the KH instability.

(iv) Two methods for quantitative characterization of coherent structures are presented – Fourier-

SPOD and Chebyshev-SPOD. In FSPOD, Fourier decomposition is first performed in the cross-stream direction followed by SPOD in the streamwise direction. Alternatively, in the CSPOD approach, Chebyshev decomposition replaces Fourier decomposition in the cross-stream direction.

(v) The different FSPOD and CSPOD modes are identified at f_{VS} and in terms of the characteristic wavelength (λ) corresponding to their respective basis functions in the cross-stream direction. It is shown that for $\lambda/D \gtrsim 1$, the mode shape and energy content are captured consistently for all f_k simulations in the study. In order to similarly capture smaller length-scales, increased scale-resolution is required.

Overall, this work presents a systematic approach to evaluating the optimal degree of scale-resolution required for SRS computations of various features of complex flows.

4. TOWARD DATA-DRIVEN REDUCED-ORDER SPATIO-TEMPORAL RECONSTRUCTION OF WAKE FLOWS USING MODAL ANALYSIS

Judiciously constructed reduced-order representations have the potential to efficiently convey the knowledge and insight contained in large datasets while significantly alleviating challenges of memory allocation and data transfer. The objective of this work is to formulate a general methodology for optimal reduced-order spatio-temporal representation which can be applied to a wide variety of flows. Using a benchmark square cylinder wake flow dataset, we develop a low-order representation of the coherent structures using well-established modal analysis building blocks. Proper orthogonal decomposition (POD) is used to identify the spatial characteristics of the flow field and dynamic mode decomposition (DMD) is employed to simplify the temporal behavior while maintaining physical interpretation. The work investigates three important reduction steps: (i) comparative assessment of POD and normalized POD (NPOD) for the spatial description of the coherent structures; (ii) DMD-based filtering of temporal (and hence spatial) scales to isolate large-scale structures of interest; and (iii) optimal sampling rate of the high-fidelity data for capturing specific flow features. The accuracy of the reconstructed field is investigated as a function of the order of the representation.

4.1 Introduction

Major advances in computer hardware capabilities and computational sciences have enabled large-scale simulations of complex scientific phenomena leading to large volumes of high-fidelity data. Especially in the field of fluid turbulence, enormous computational effort has been invested in performing high-fidelity simulations to accumulate large volumes of valuable data. While these datasets have led to important scientific progress, in many instances processing massive volumes of data poses many challenges in memory allocation and storage. The degree of detail incumbent in these massive datasets is not of practical utility for many applications where only certain features contained in the data are relevant. Lower-order representations that capture only the required

features and can be rendered rapidly is of significant value for real-world utility. Apart from traditional engineering applications, many emerging and novel technologies can benefit from such development. For example, in multi-disciplinary optimization, it is difficult, and indeed not necessary, to have a high-fidelity model for each of the contributing processes. For digital twins and decision dashboards, reduced-order representation of flow fields is highly sought-after.

There is a compelling need to extract select features from large volumes of data and construct a low-dimensional model of the phenomenon under consideration. By assimilating techniques used for data compression and physics-based analysis, highly complex scientific phenomena can be approximated by lower-order representation. It is also desirable to maintain physical interpretation rather than exclusively depend on data-driven techniques such as neural networks and similar deep learning techniques. In the field of complex flows, proper orthogonal decomposition (POD) [115, 123] has often been used to examine various modes of the flow field [117, 118, 81, 82, 83, 84, 85, 86]. Known to other fields as principal component analysis (PCA) [124] or Karhunen-Loève expansion [125, 126], POD is well-established as a means of characterizing spatial flow patterns which are optimized regarding their energy content. More recently, dynamic mode decomposition (DMD) [120] has gained interest as a means of identifying similar mode shapes but maintaining their direct correspondence to discrete, pre-defined frequencies/temporal behavior [127, 128, 129, 130, 131, 132, 133]. For low-dimensional models of complex fluid flows, which is the principal interest of this study, POD and DMD offer the requisite analytical building blocks for achieving the dimensionality reduction.

The objective of this work is to formulate a general methodology for optimal reduced-order spatio-temporal representation which can be applied to a wide variety of flows. Toward this end, well-established modal analysis techniques are used to develop a low-order representation of the large-scale coherent structures using a large, high-fidelity square cylinder wake flow dataset. Three important reduction aspects are investigated: (i) comparative assessment of POD and normalized POD (NPOD) for the spatial description of the coherent structures; (ii) DMD-based filtering of temporal (and hence spatial) scales to isolate large-scale structures of interest; and (iii) optimal

sampling rate of the high-fidelity data for capturing specific flow features.

In this paper, a reduced-order reconstruction is undertaken for the benchmark case of wake flow past a square cylinder. Turbulent wakes manifest in many engineering fields and thorough understanding and monitoring are required to ensure safety and efficiency. For example: optimizing safety and efficiency on congested airports runways [40, 41, 42, 43]; efficient operation of wind farms [44, 45, 46, 47]; mitigating detectable wakes of submersibles [48, 49, 50]; safe operation of offshore platforms [51, 52, 53, 54]; each of these instances is subject to catastrophe if not provided sufficient consideration. While a straightforward solution would be the application of direct numerical simulations of such cases in real-time, both the computational time and memory required would prove astronomical. Regarding wake flow simulations, reduced-order representations enable a multitude of applications through sufficiently accurate 'real-time CFD'. End-users – whether human operators or automated processes – would be able to adjust the physical fidelity of these reconstructions according to predetermined specifications. Based upon these reduced-order analogs of the system, important flow metrics can then be integrated as part of higher-level system analysis.

This work is organized as follows: Section 4.2 introduces the square cylinder wake flow dataset used to demonstrate and assess the methodology. This includes the governing equations and computational setup implemented for its acquisition. In Section 4.3, the modal analysis techniques (namely POD and DMD) and their roles in the proposed methodology are discussed. Section 4.4 presents the effects of the three reduction steps under assessment along with the accuracy of integral quantities as a function of the order of the representation. Conclusions from this work are then discussed in Section 4.5.

4.2 Wake Flow as Test Case

The focus of this work is upon developing a general methodology for optimal reduced-order spatio-temporal representation which can be applied to a wide variety of flows. The concept is independent of the flow geometry used in this study and applicable irrespective of how the dataset is acquired/generated. For sake of demonstration, we consider the canonical flow past a square

cylinder at $Re = 22,000$. This statistically two-dimensional benchmark case provides insight into many wake flow phenomena of engineering interest: massive separation; vortex shedding (the von Kármán vortex-shedding (VS) instability), free shear-layer instability (the Kelvin-Helmholtz (KH) instability), and coherent structures. In a previous study [56], a Partially-Averaged Navier-Stokes (PANS) simulation was used to generate a high-fidelity dataset for this benchmark case. That dataset is now used in this study and, for the sake of completeness, the details regarding its generation are included in this section.

4.2.1 Governing Equations

Following the PANS methodology, V_i and p are decomposed into the following components: resolved fields, U_i and $\langle p \rangle$, and residual fields, u_i and p_u. Evolution equations for the resolved quantities can then be derived from the Navier-Stokes equations, as follows [88],

$$\frac{DU_i}{Dt} + \frac{\partial \tau_{ij}}{\partial x_j} = -\frac{\partial \langle p \rangle}{\partial x_i} + \nu \frac{\partial^2 U_i}{\partial x_j \partial x_j}, \tag{4.1}$$

$$\frac{\partial^2 \langle p \rangle}{\partial x_i \partial x_i} = -\frac{\partial U_i}{\partial x_j}\frac{\partial U_j}{\partial x_i} - \frac{\partial^2 \tau_{ij}}{\partial x_i \partial x_j}, \tag{4.2}$$

where τ_{ij} is the generalized central second moment or sub-filter stress (SFS) tensor. We employ the Boussinesq approximation [78] such that:

$$\tau_{ij} = -\nu_u \left(\frac{\partial U_i}{\partial x_j} + \frac{\partial U_j}{\partial x_i} \right) + \frac{2}{3} k_u \delta_{ij}, \tag{4.3}$$

where ν_u is the unresolved eddy viscosity and k_u is the unresolved turbulent kinetic energy.

Within the PANS paradigm, scale-resolution is controlled by the filter parameters, f_k and f_ε, which are the ratio of unresolved-to-total kinetic energy and dissipation, respectively. Similarly, the unresolved-to-total specific dissipation rate, f_ω, can be defined in terms of these two parameters:

$$f_k \equiv \frac{k_u}{k} \quad \text{and} \quad f_\varepsilon \equiv \frac{\varepsilon_u}{\varepsilon}; \quad f_\omega \equiv \frac{\omega_u}{\omega} = \frac{f_\varepsilon}{f_k}. \tag{4.4}$$

For this study, $f_k = 0.10$ and $f_\varepsilon = 1$ are selected. This means that 90% of the turbulent kinetic energy is resolved, leaving the remaining 10% to be modelled. The turbulent dissipation is wholly modelled, as dissipation is dominant only at the smallest scales at the Reynolds number used.

The PANS k-ω model [89] for the k_u and ω_u are as follows:

$$\frac{Dk_u}{Dt} = \tau_{ij}\frac{\partial U_i}{\partial x_j} - \beta^* k_u \omega_u + \frac{\partial}{\partial x_j}\left[\left(\nu + \frac{\nu_u}{\sigma_{k_u}}\right)\frac{\partial k_u}{\partial x_j}\right]; \tag{4.5}$$

$$\frac{D\omega_u}{Dt} = \frac{\alpha}{\nu_u}\tau_{ij}\frac{\partial U_i}{\partial x_j} - \left(\alpha\beta^* + \frac{\beta - \alpha\beta^*}{f_\omega}\right)\omega_u^2 + \frac{\partial}{\partial x_j}\left[\left(\nu + \frac{\nu_u}{\sigma_{\omega_u}}\right)\frac{\partial \omega_u}{\partial x_j}\right] \tag{4.6}$$

where: $\sigma_{k_u} = \frac{f_k}{f_\omega}\sigma_k$, $\sigma_{\omega_u} = \frac{f_k}{f_\omega}\sigma_\omega$, and $\nu_u = k_u/\omega_u$. The closure coefficients (β^*, α, β, σ_k, σ_ω) used are those of the standard RANS k-ω model [90].

4.2.2 Computational Setup

A three-dimensional flow domain is used, measuring $30D \times 14D \times 4D$. A schematic of this domain is shown in Figure 4.1 along with representative slices of the mesh shown in Figure 4.2. A Cartesian coordinate system is utilized such that the streamwise-, cross-stream- and spanwise-directions coincide with the x-, y-, and z-directions, respectively, with the origin located at the center of the square cylinder.

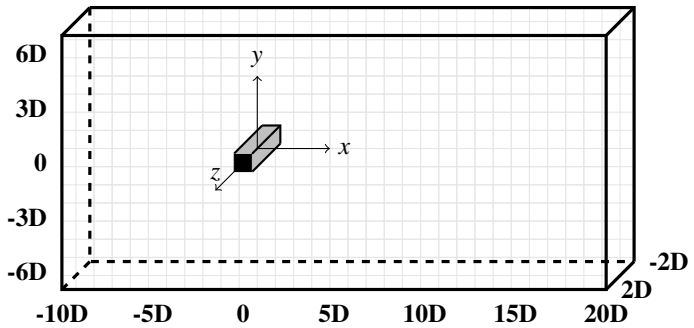

Figure 4.1: Non-dimensional schematic of the physical domain, which measures $30D \times 14D \times 4D$.

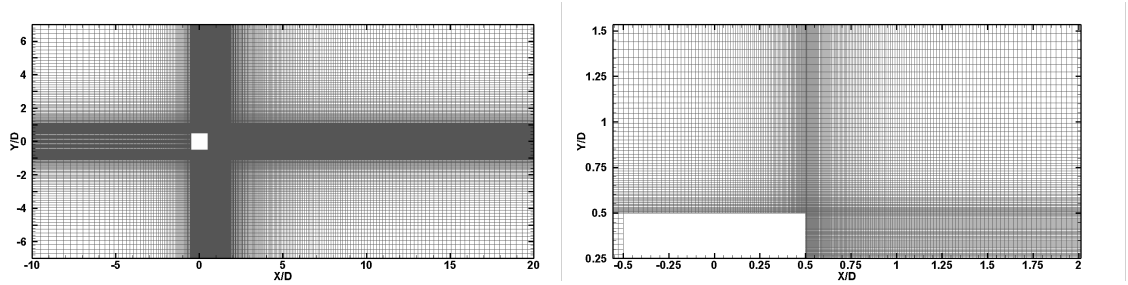

Figure 4.2: **(a)** Full domain-view of a representative slice of the mesh; and **(b)** zoomed-in view of the cells surrounding the square cylinder.

At the inlet-plane, uniform freestream velocity, V_∞, is prescribed, along with zero-normal derivative for pressure. The remaining quantities at the inlet are prescribed as follows:

$$k_u = \frac{3}{2}(0.01V_\infty)^2 f_k; \qquad \nu_u = 10\nu\frac{f_k^2}{f_\varepsilon}; \qquad \omega_u = k_u/\nu_u. \tag{4.7}$$

At the square cylinder surface: no-slip and no-penetration conditions are applied; k_u and ν_u are also prescribed at near-zero values, in kind; and zero-normal derivative for pressure. The unresolved specific dissipation is defined at the surface as:

$$\omega_u = \frac{96\nu}{\beta_0 d_{wall}^2} f_\omega, \tag{4.8}$$

following [113]. At the outlet-plane, a convective boundary condition is applied to the velocity field, the pressure field is prescribed as zero, and zero-normal derivatives are prescribed for all remaining variables. Slip and periodic boundary conditions are used for the cross-stream and spanwise planes, respectively.

Computations are performed using an open source, finite-volume code, OpenFOAM [72]. The Pressure-Implicit with Splitting of Operators (PISO) algorithm [73] is employed for the coupling of pressure and velocity fields. Second-order accurate schemes are used for the spatial and temporal discretizations.

In a previous work [56], a grid independence study was performed along with validation against established literature. Integral quantities, first- and second-order one-point statistics, and stream-

wise velocity probe spectra were found to be in good agreement with said literature. In this study, the accuracy of these quantities of interest (QoI) was found to largely depended upon resolution of the VS instability. Only for more complex QoI (i.e. probe spectra and smaller-scale coherent structures) did the full resolution of the KH instability become more critical. The frequencies reported for the VS and KH instabilities used in the current work are 0.12 and 3.6, respectively.

A key objective of that study was to quantitatively characterize coherent structures. Expounding upon similar work for the case of axisymmetric wakes [112], which incorporated a Fourier filter in the azimuthal direction [121], two methodologies were demonstrated. These methods enable the isolation of modes corresponding to specific length- and time-scales for highly descriptive characterizations of the coherent structures in the wake. While such techniques are appropriate for fully describing the coherent structures quantitatively, the degree which the field has been decomposed to facilitate this is not ideal for full field reconstruction.

4.3 Reconstruction Methodology

As mentioned in Section 4.1, the objective of this work is to develop a general and robust procedure for reduced-order reconstruction of flows with coherent structures from high-fidelity data. For the modal decomposition techniques which follow, state-variables, q, are obtained at regular intervals in time, t_i, for all state-coordinates in the desired domain, mapped by $\vec{x}$. This data is formatted as a column vector and stored in matrix, Q, as shown in Eqn. 4.9a. The mean field ($\overline{\mathrm{Q}}$) is then separated from the fluctuating field (Q'), as follows:

$$\mathrm{Q} = \{q(\vec{x},t_0), q(\vec{x},t_1), \ldots, q(\vec{x},t_N)\}; \tag{4.9a}$$

$$\mathrm{Q} = \overline{\mathrm{Q}} + \mathrm{Q}' = \overline{\mathrm{Q}} + \{q'(\vec{x},t_0), q'(\vec{x},t_1), \ldots, q'(\vec{x},t_N)\}. \tag{4.9b}$$

Separation of the mean field is not strictly necessary for the modal decompositions discussed in this section. However, depending upon the nature of the state-variable under analysis, leaving the mean field in the dataset can obfuscate other physics. For example, for the flow considered in this

study, the mean streamwise velocity field contains a significant portion of the energy in the flow field. Conversely, the mean cross-stream velocity field contains much less energy. By leaving the mean field present in the data, it obfuscates earlier modes to represent the bulk of energy it entails, complicating analysis. As the objective of this work is to develop a low-order representation of the large-scale coherent structures, it is sensible to take this precursory step for consistency and convenience.

4.3.1 Proper Orthogonal Decomposition

Introduced to the field of turbulence by Lumley [115, 123], POD has become a popular means of characterizing coherent structures in a wide variety of flows [117, 118, 81, 82, 83, 84, 85, 86]. In this work, we more specifically use the 'snapshot' POD algorithm of Sirovich [119] which, using the snapshot matrix defined above, can be represented as follows:

$$\mathrm{Q}'(\vec{x},t_i) = \sum_{m=0}^{N} \psi_m(\vec{x})\alpha_m(t_i), \tag{4.10}$$

where the fluctuating component, $\mathrm{Q}'(\vec{x},t_i)$ can be decomposed as a summation of modes comprised of a mode shape, $\phi_m(\vec{x})$, and a temporal coefficient, $a_m(t_i)$. This is typically computed using a compact singular value decomposition (SVD) [134], such that:

$$\mathrm{Q}' = \mathrm{U}\Sigma\mathrm{V}^*, \tag{4.11}$$

where the columns of U are the POD mode shapes, $\psi(\vec{x})$, the diagonal of Σ contains the modal amplitudes, σ, and the columns of V are the corresponding temporal coefficient vectors/signals, $\mathscr{V}(t)$. It should be noted that since the mean field is removed previously, this is equivalent to PCA [135].

Later in this study (Section 4.4.1), the effect of locally normalizing the flow field prior to the calculation of POD is assessed. This variation of POD, known as normalized POD (NPOD) [136],

normalizes each state-coordinate signal by its local standard deviation, producing Q'_N as follows:

$$\mathrm{Q}_{SD}(x) = \sqrt{\frac{1}{N}\sum_{i=0}^{N} |q'(x,t_i)|^2}; \tag{4.12a}$$

$$\mathrm{Q} = \overline{\mathrm{Q}} + \mathrm{diag}(\mathrm{Q}_{SD})\mathrm{Q}'_N. \tag{4.12b}$$

The preconditioning of the snapshot matrix ensures that the flow structures in the entire flow domain are equally weighted irrespective of energy content. Often, large fluctuations occur in the near-wake with lesser variation downstream. Because the order of POD mode shapes is determined by energy contribution, this means that structures in the far-wake might be disregarded to better capture structures in the near-wake. As we seek to capture an accurate spatial description of all large-scale coherent structures within the domain, a comparative assessment is needed to determine whether impeding the optimal decomposition of POD in this manner leads to improved representation of these structures.

While POD categorizes modes according to energy content, it cannot distinguish different scales of the flow. Although POD excels at capturing spatial features, the temporal aspects essential for reconstruction are not sufficiently addressed.

4.3.2 Dynamic Mode Decomposition

More recently, DMD has been introduced to the field of fluid dynamics by Schmid [120] and has been used for examining temporal features of a wide assortment of flows [127, 128, 129, 130, 131, 132, 133]. Rather than seek modes spatially according to their energy content like POD, DMD determines modes based on frequency. The evolution of the q' field can be expressed as:

$$q'(\vec{x},t_{i+1}) = \mathrm{A}q'(\vec{x},t_i) \quad \text{or} \quad \mathrm{Q}'_2 = \mathrm{A}\mathrm{Q}'_1. \tag{4.13}$$

Here A is the linear operator which evolves the state at $t = i$ to $t = i+1$, and Q'_1 and Q'_2 are as follows:

$$\begin{aligned} \mathrm{Q}_1' &= \{q'(\vec{x},t_0), q'(\vec{x},t_1), \ldots, q'(\vec{x},t_{N-1})\}, \\ \mathrm{Q}_2' &= \{q'(\vec{x},t_1), q'(\vec{x},t_2), \ldots, q'(\vec{x},t_N)\}. \end{aligned} \tag{4.14}$$

Following the algorithm of Tu et al. [137], we then apply Eqn. 4.11 to Q_1' where the output matrices can be truncated to r-modes depending on the rank of Q_1'. Using this decomposition, we then seek A which will enable mapping from one time step to the next. However, it is more computationally efficient to solve for the $r \times r$ projection of A onto POD modes ($\tilde{\mathrm{A}} = \mathrm{U}^* \mathrm{A} \mathrm{U}$), as follows [137]:

$$\mathrm{A} = \mathrm{Q}_2' \mathrm{V} \Sigma^{-1} \mathrm{U}^*; \tag{4.15a}$$

$$\tilde{\mathrm{A}} = \mathrm{U}^* \mathrm{Q}_2' \mathrm{V} \Sigma^{-1}. \tag{4.15b}$$

We then compute the eigen-decomposition of $\tilde{\mathrm{A}}$,

$$\tilde{\mathrm{A}} \mathrm{W} = \mathrm{W} \Lambda. \tag{4.16}$$

Using this eigen-decomposition, we can obtain the DMD mode shapes contained in the columns of Φ:

$$\Phi = \mathrm{Q}_2' \mathrm{V} \Sigma^{-1} \mathrm{W}. \tag{4.17}$$

These can then be used to reconstruct a low-rank approximation of the solution for any time, t:

$$q'(\vec{x},t) \approx \sum_{k=1}^{r} \phi_k(\vec{x}) \exp(\omega_k t) b_k = \Phi \exp(\Omega t) \mathrm{b}; \tag{4.18a}$$

$$\omega_k = \ln(\lambda_k)/\Delta t; \tag{4.18b}$$

$$\mathrm{b} = \Phi^{\dagger} q'(\vec{x},t_0); \tag{4.18c}$$

where the eigenvalues, λ_k, are rewritten in the form of ω_k, which make up Ω according to $\Omega = \mathrm{diag}(\omega)$, and $\Phi^{\dagger}$ is the Moore-Penrose pseudoinverse of Φ, used to calculate the initial amplitude of the DMD modes, b [137].

It has been well demonstrated that DMD can be used for interpolation within the original dataset, as well as extrapolation to future instances. While this forecasting ability is a significant advantage over POD, this comes at the cost of energy distribution across a much larger number of spatial modes. As an analytical tool, directly correlating spatial structures to specific frequencies is greatly beneficial and worth the 'inefficiency'. For a reduced-order representation of the flow field, however, this feature impedes the primary objective of this work.

4.3.3 Proposed Solution: POD-DMD

While POD optimally extracts key spatial modes, it offers little in the way of forecasting, relying on a temporal coefficient vector to reconstruct the solution. Alternatively, DMD provides precise temporal information, differentiating modes by specific individual frequencies. It is natural to propose a combination of these two methods such that each could be utilized according to their specialty. The Chronos-Koopman spectral decomposition [138] develops this concept, applying POD and then utilizing DMD to evolve only the temporal coefficients derived from POD.

The objective of this work is to formulate a general methodology for optimal reduced-order spatio-temporal representation which can be applied to a wide variety of flows. Toward this end, we extend the methodology of [138] to include additional aspects that incorporate improved accuracy,

filtering, and efficiency using fundamental modal analysis building blocks. These aspects are (i) a priori local normalization for a more accurate spatial description of the coherent structures; (ii) DMD-based pre-filtering of temporal (and hence spatial) scales to isolate the large-scale structures of interest; and (iii) optimal sampling rate of the high-fidelity data for capturing specific flow features.

This methodology is undertaken in three key steps (outlined in Figure 4.3), as follows:

Step 1: Pre-Filtering of Dataset (DMD)

In turbulence, it is well known that there is a strong correlation between spatial and temporal scales. As the focus of this work is upon capturing large-scale structures, it stands to reason that filtering out small time-scales (high-frequency information) would correspond to removing small-scale structures from the flow field. Because DMD identifies modes corresponding to specific frequencies, it can be effectively applied to the flow field as a low-pass filter.

Accordingly, the DMD algorithm is applied to Q' as described in Eqns. 4.14-4.18c. This results in DMD mode shapes, $\phi_k(\vec{x})$, initial modal amplitudes, b_k, and modal frequencies, ω_k. It should be noted that the number of frequencies, and therein modes, that are produced will be capped by the rank of Q'. This is because the initial POD modes calculated within the algorithm (according to Eqn. 4.11) are best truncated for efficiency and the rank of Q' is naturally the highest, reasonable limit. Depending upon the desired fidelity, a threshold frequency, ω_T, is selected and all modes corresponding to $\omega_k > \omega_T$ are removed. The effect of this reduction aspect is assessed in greater detail in Section 4.4.2.

As the temporal character of all DMD modes is fixed, the behavior of modes at intermediate and future instances in time can be approximated. When reconstructing the flow field according to Eqn. 4.18a, the sampling rate can artificially be reduced according to ω_T based upon the Nyquist criterion. By reducing the number of time steps saved for subsequent calculation, the efficiency of the method is improved. The impact of this aspect is assessed in

Section 4.4.3.

Step 2: Spatial Compression (POD or NPOD)

We now seek to spatially compress the dataset. In terms of memory, the spatial aspect of the state-coordinates is the most expensive and by identifying important modes, we reduce the amount of data stored from the number of time steps saved to the number of modes needed to represent them.

Using the filtered Q' (Q'_{filt}) from the previous step, the POD mode shapes, $\psi_m(\vec{x})$, amplitudes, σ_m, and temporal coefficient signals, $\mathscr{V}_m(t)$, are computed as described in Eqn. 4.11.

Similarly, these components can be computed instead with NPOD according to the normalization described in Eqn. 4.12a and Eqn. 4.12b. The a priori local normalization introduced by NPOD equally distributes the significance of state-coordinates throughout the entirety of the flow field. The improvement in accuracy this provides is assessed in Section 4.4.1.

Prior to reconstruction, it is important to determine the desired number of modes, ρ, to be stored. This is most commonly selected using an 'energy-recovery' argument, described by:

$$\frac{\sum_{m=1}^{\rho} \sigma_m^2}{\sum_{m=1}^{M} \sigma_m^2} \equiv \varepsilon_\rho > E, \tag{4.19}$$

where ε_ρ is defined as the accumulative energy content recovered by ρ-modes and E is the desired energy-recovery percentage.

The temporal coefficient matrix, V, is truncated to r-modes, where r is the rank of Q'. Note that most likely, $r > \rho$.

Step 3: Synthesizing Temporal Coefficient Functions (DMD)

Finally, we seek to extract information from the temporal coefficient signals output by POD and synthesize them as functions of time. Again, in terms of memory, the spatial aspect of the state-coordinates dwarfs that of the corresponding temporal information. However, by

synthesizing these functions, the flow field can be evolved to intermediate instances in time, as well as those beyond the collected sample. The predictive capability enabled by this step is what makes such reduced-order reconstructions truly powerful in advanced higher-level systems analysis.

First transposing $\mathrm{V}^{(r)}$ to obtain a similar form as Eqn. 4.9a (i.e. $\mathscr{V}^{(r)} = [\mathrm{V}^{(r)}]^*$), the DMD algorithm (as described in Eqns. 4.14-4.18c) is again applied. This transforms $\mathscr{V}^{(r)}$ from a static collection of signals into concatenated functions in time, as follows:

$$\mathscr{V}(t) \approx \sum_{k=1}^{r} \phi_k \exp(\omega_k t) b_k = \Phi \exp(\Omega t) \mathrm{b}. \tag{4.20}$$

This concatenation is then further truncated to match the previously stored ρ-POD modes, resulting in a final reduced-order spatio-temporal reconstruction:

$$\mathscr{Q}' = \mathrm{U}^{(\rho)} \Sigma^{(\rho)} \left[\mathscr{V}^{(\rho)}(t) \right]^* \tag{4.21}$$

This outlined methodology expands upon previous work [138] and expands it toward a more accurate, filtered, and efficient framework for reduced-order spatio-temporal representation of wake flows, per the objectives of this work. Three important reduction aspects are investigated: (i) comparative assessment of POD and normalized POD (NPOD) for the spatial description of the coherent structures (Section 4.4.1); (ii) DMD-based filtering of temporal (and hence spatial) scales to isolate large-scale structures of interest (Section 4.4.2); and (iii) optimal sampling rate of the high-fidelity data for capturing specific flow features (Section 4.4.3).

4.4 Results & Discussion

In this study, data originating from a PANS $f_k = 0.10$ simulation is utilized to investigate aspects of the reduced-order spatio-temporal reconstruction methodology proposed using POD and DMD. The results in this section are based on the spanwise vorticity on an XY-plane. Regular snapshots are collected at regular non-dimensional time steps ($\Delta t^* = \Delta t V_\infty / D = 0.06875$). The

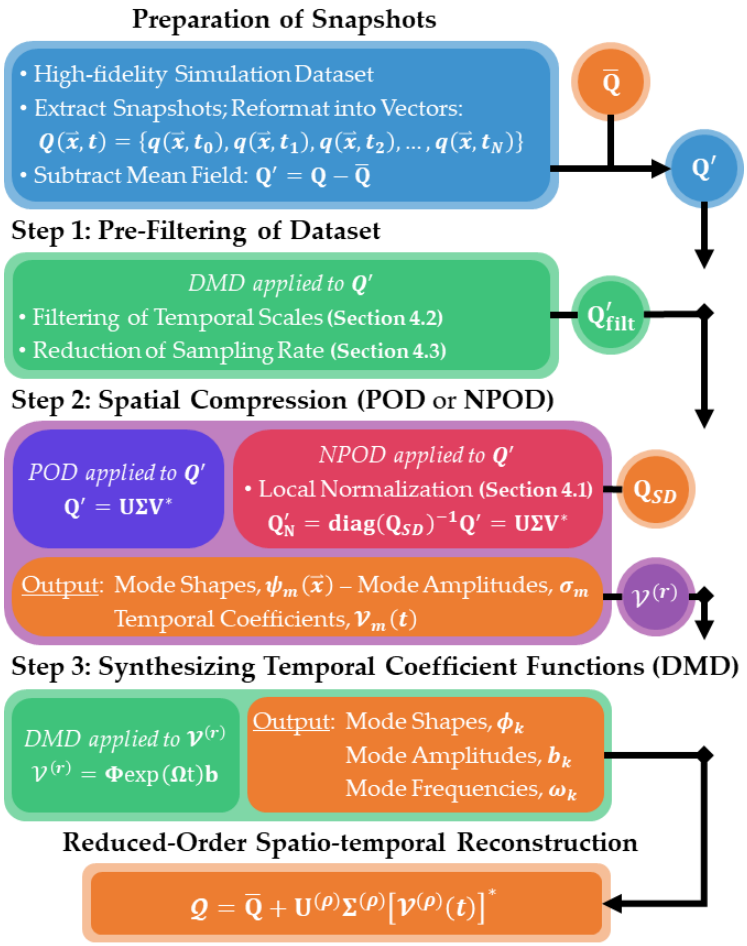

Figure 4.3: Data flow of the proposed methodology described in Section 4.3.3. High-fidelity data is extracted, formatted appropriately, and the mean field is subtracted (blue). An optional pre-filtering step is applied using DMD (green), followed by spatial compression step (purple) performed using POD (blue) or NPOD (red). The temporal coefficient signals are then processed using DMD to generate a reduced-order spatio-temporal reconstruction. All components which are used in the final reconstruction are indicated in orange.

subset of this data used in the following results contains over $89,000$ state-coordinates per snapshot over a window of nearly $5,800$ snapshots.

4.4.1 Local Normalization of the Field

The first aspect of the proposed methodology we seek to assess is a priori local normalization of the flow field. As mentioned in Section 4.3.1, this process utilizes NPOD [136], a variant of POD in which each state-coordinate is normalized by its standard deviation, the range of which

can be seen in Figure 4.4. Although this interferes with the optimal nature of the POD modes concerning energy-content, this weights all parts of the flow field equally throughout the domain.

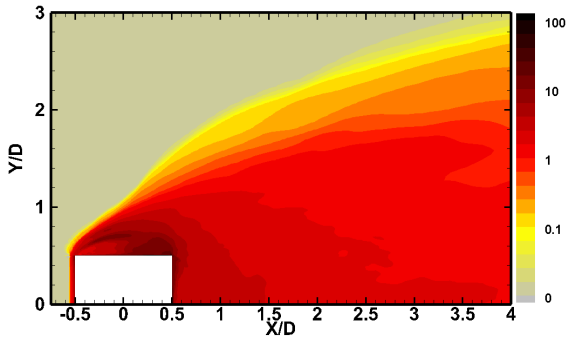

Figure 4.4: Contour plot of the local standard deviation of the z-vorticity flow field. Each state-coordinate is normalized by its respective local standard deviation within NPOD.

We first compare the components of the first four modes (m = 1-4) of POD and NPOD. The temporal coefficient signals, $\mathscr{V}_m$, are shown in Figure 4.5; the mode shapes, U_m, in Figure 4.6; and their accumulative modal energy content, ε_ρ, in Figure 4.7. From the temporal coefficient signals, it is clear that the first mode ($m = 1$) shows strong agreement between both methods, due to the dominance of the VS frequency in each. However, POD also incorporates many higher frequencies, differing strongly from NPOD which appears nearly sinusoidal. It is clear that the early NPOD signals are dominated by the frequency which affect the majority of the domain. These types of behavior are confirmed upon review of the early mode shapes. Again, the first modes ($m = 1$) of both methods bear a strong resemblance to one another, but the similarities wane quickly thereafter. In general, NPOD mode shapes exhibit much larger structures with greater intensity throughout the domain. Lastly, it is clear that the reorganization of energy caused by prior normalization leads to increased energy content in the early modes. This in concert with predominantly low-frequency content in the early temporal coefficient signals results in reconstructed flow fields that appear stronger and smoother than its POD counterparts which exhibit a 'jittery' behavior (see Video S2 and Video S3, provided in the Supplementary Materials).

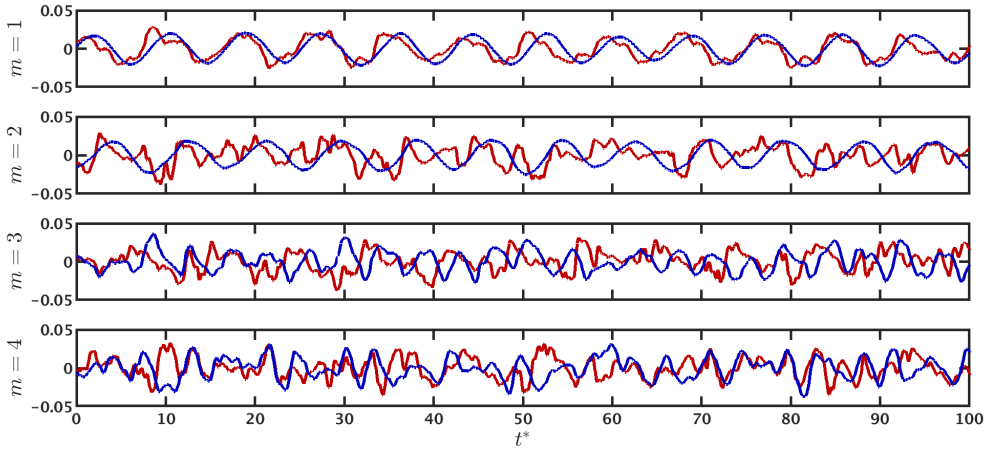

Figure 4.5: A priori normalization comparison: temporal coefficient signals, $\mathscr{V}_m$, corresponding to the first four output modes (m = 1-4) for: POD [—]; and NPOD [—].

We then compare the components of four higher-order modes (m = 93-96), shown as follows: temporal coefficient signals, $\mathscr{V}_m$, in Figure 4.8; mode shapes, U_m, in Figure 4.9; and (normalized) individual modal energy content, σ_m^{2*}, in Figure 4.10. Upon review of the signals, it is difficult to identify many features in agreement; both methods at higher-order modes produce signals with significant higher-frequency content. Likewise, the mode shapes lack much in common, however, NPOD mode shapes still exhibit larger structures that span a wider (and longer) area downstream than their POD counterparts. We then assess the individual modal energy contributions. While the early modes of NPOD carried greater overall weight, this declines sharply after the first two modes and by the eleventh mode reaches a steady rate of decline in energy content. Alternatively, after the first two modes, the POD modes contain more energy individually until the eighteenth mode where it also reaches a steady rate of decline, much steeper than that of NPOD. For sake of reconstruction, this means that POD will continue to offer increasingly lesser information with the addition of more modes as opposed to NPOD (although at the cost of needing more modes to have equivalent energy recovery). There is little discernible difference between POD and NPOD reconstructions using a higher number of modes (as can be seen by comparing Video S4 and Video S5, provided in the Supplementary Materials).

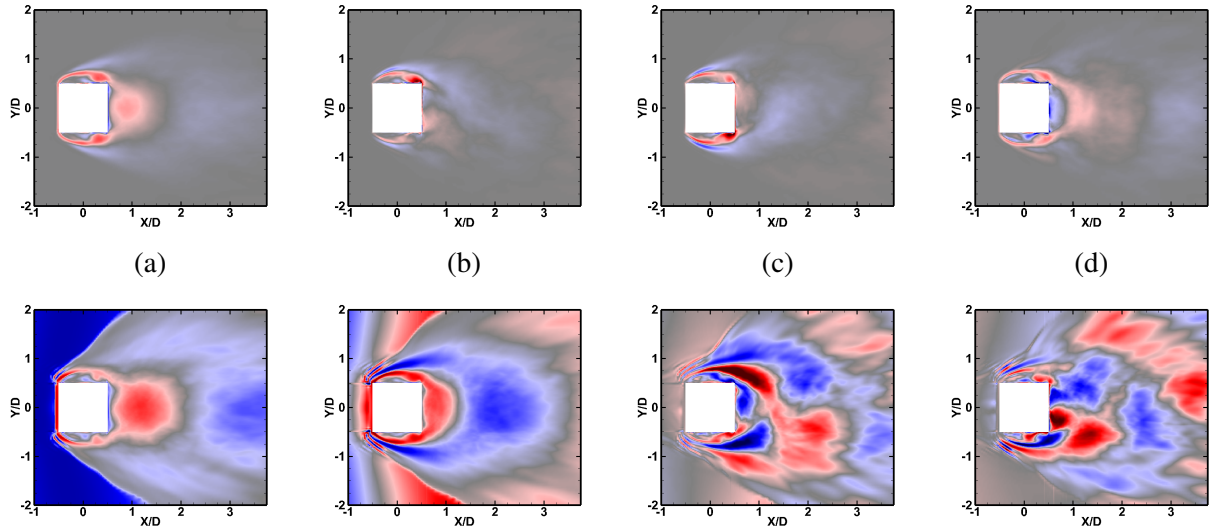

Figure 4.6: Normalization comparison: mode shapes, U_m, corresponding to the first four output modes (m = 1-4) for: **(a-d)** POD; and **(e-h)** NPOD, respectively.

Overall, normalization of the flow field prior to modal decomposition has two main effects. The first is that by emphasizing each state-coordinate, priority is given to frequencies that impact the entire domain. For the case of turbulent flow past a square cylinder, this is the VS frequency (f_{VS}) and as such this makes early NPOD modes more readily explicated. The second effect is increased clarity (amplitude) of the structures beyond the near-wake region. Again, because equal weighting is provided throughout the domain, structures carried downstream into the far-wake do not disappear as readily as with a POD-based reconstruction.

4.4.2 Pre-filtering of Higher Frequencies

Next, we assess the use of DMD to remove higher-frequency information from the data prior to performing POD. As can be seen in Figure 4.11, a frequency spectrum can be created using ω_k [$St_k = (\omega_k/2\pi)D/V_\infty$] and the corresponding magnitude of b_k. Implemented as a low-pass filter, two cut-offs are compared, the first based on the KH frequency ($f_{KH} = 3.6$) and the second on the second harmonic of the VS frequency ($2f_{VS} = 0.24$). This correlates to equivalently passing $\sim 51\%$ or $\sim 3.5\%$ of the original frequencies output by the DMD algorithm. As turbulent wakes

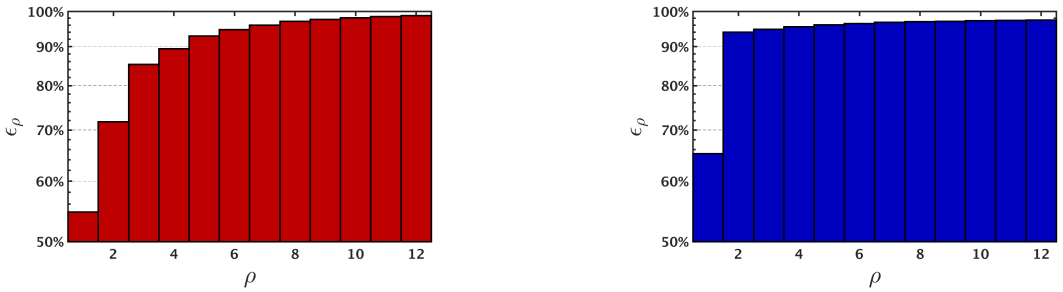

(a) (b)

Figure 4.7: A priori normalization comparison: accumulative modal energy content, ε_ρ, up to 12-modes using **(a)** POD, and **(b)** NPOD.

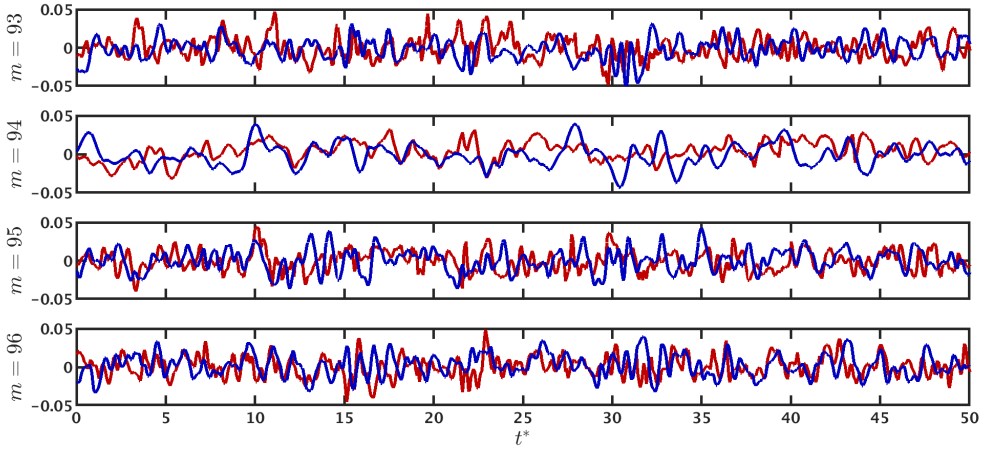

Figure 4.8: A priori normalization comparison: temporal coefficient signals, $\mathscr{V}_m$, corresponding to four higher-order modes ($m =$ 93-96) for: POD [—]; and NPOD [—].

are highly spatio-temporal, such a filter aims to better isolate large-scale structures and determine how this affects reconstruction. Video S6 and Video S7 demonstrate the immediate effects of the f_{KH}-based and $2f_{VS}$-based pre-filtered flow fields, provided in the Supplementary Materials.

We begin by comparing the components of the original first four POD modes ($m =$ 1-4) with those which have been subjected to the f_{KH}-based or $2f_{VS}$-based pre-filter. The temporal coefficient signals, $\mathscr{V}_m$, are shown in Figure 4.12 and the mode shapes, U_m, in Figure 4.13. The signals resulting from the f_{KH}-based pre-filter are indiscernible from those of the original POD signals,

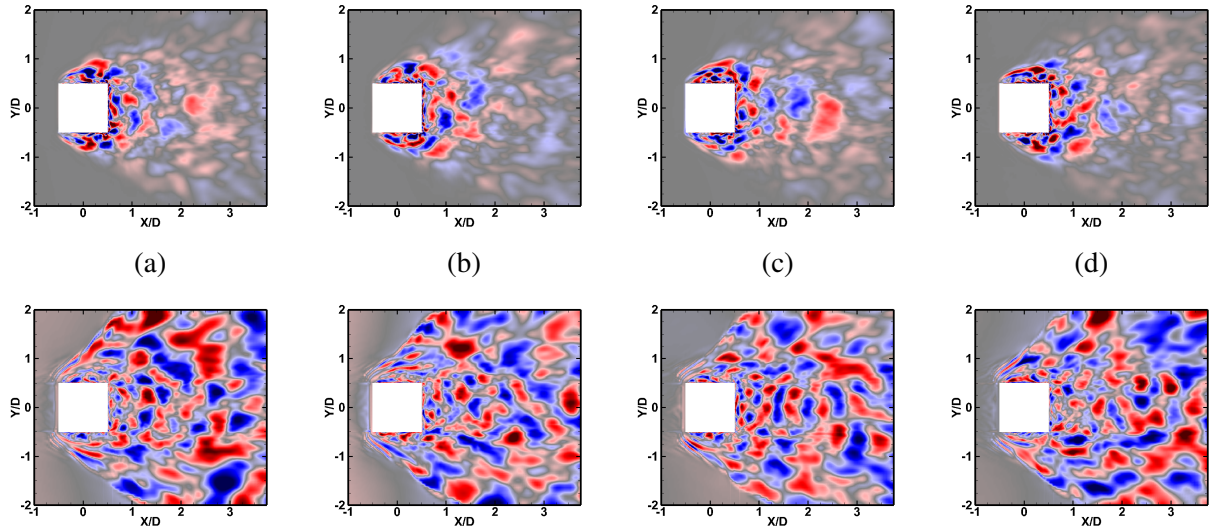

Figure 4.9: A priori normalization comparison: mode shapes, U_m, corresponding to four higher-order modes ($m = 93$-96) for: **(a-d)** POD; and **(e-h)** NPOD, respectively.

as such high-frequency content does not strongly manifest in the primary modes. The $2f_{VS}$-based pre-filter signals, although approximating the first few modes well, show moderate deviations by $m = 4$. This is similarly reflected in the early mode shapes. The f_{KH}-based pre-filter mode shapes are practically identical to their unfiltered counterparts. Those of the $2f_{VS}$-based pre-filter, however, while maintaining strong similarity until $m = 4$, exhibit structures/regions of higher amplitude near the square cylinder. This translates well when used for a low-mode reconstruction, as can be seen in Video S8 and Video S9 (for the f_{KH}-based pre-filter and $2f_{VS}$-based pre-filter, respectively, provided in the Supplementary Materials). The 12-mode reconstruction using f_{KH}-based pre-filter inherits the same jittery behavior seen in the unfiltered equivalent, owing to the higher frequencies still present in the lower modes. Meanwhile, the 12-mode reconstruction using $2f_{VS}$-based pre-filter exhibits much smoother evolution of its structures, and the VS coherent structures are more pronounced (larger magnitude, less quickly dissipated downstream).

This behavior continues for higher-order POD modes (as can be seen by reviewing $m = 93$-96). As shown in Figure 4.14, although deviating occasionally, the f_{KH}-based pre-filtered signal

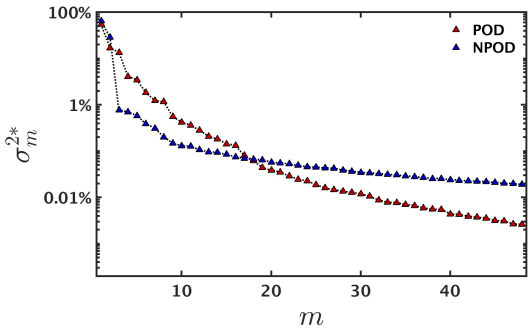

Figure 4.10: A priori normalization comparison: (normalized) individual modal energy content, σ_m^{2*}, up to 48-modes.

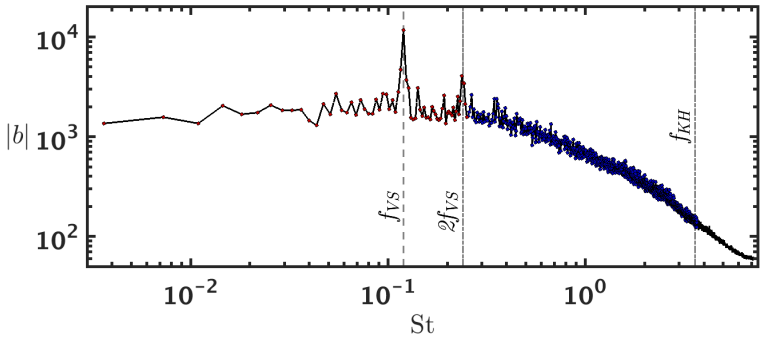

Figure 4.11: DMD-based, non-dimensionalized frequency spectrum. Dashed lines denote the primary and secondary instability frequencies (f_{VS} and f_{KH}) along with the second harmonic of f_{VS} which is used as a cut-off. The $2f_{VS}$-based pre-filter incorporates frequencies indicated by [•], while the f_{KH}-based pre-filter incorporates frequencies indicated by [•] and [•].

matches well with the original unfiltered signals. At such high levels, however, higher frequencies are inherent and there is little to no agreement with the $2f_{VS}$-based pre-filtered signal. Once more, this is reflected in the corresponding mode shapes provided in Figure 4.15. Parallels can still readily be drawn between the f_{KH}-based pre-filtered mode shapes [Figure 4.15(a-d)] and the unfiltered equivalents [Figure 4.9(a-d)], despite growing discrepancies. Alternatively, the $2f_{VS}$-based pre-filtered mode shapes bear little to no resemblance to the unfiltered modes, tending toward larger, elongated structures. When fully reconstructed using a greater number of modes, it is clear that the added information corrects the low-mode f_{KH}-based pre-filtered reconstruction's jittery-nature,

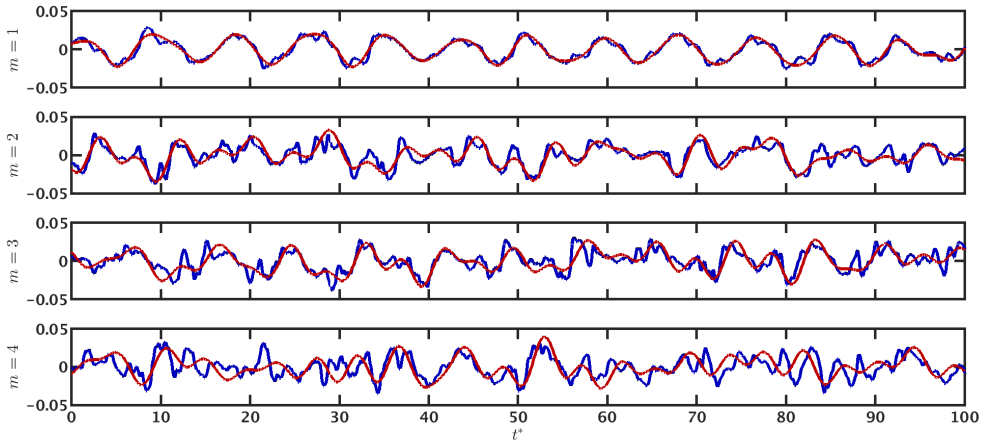

Figure 4.12: Pre-filtering comparison: temporal coefficient signals, $\mathscr{V}_m$, corresponding to the first four output modes (m = 1-4) for: unfiltered POD [—]; POD pre-filtered by f_{KH} [—]; and POD pre-filtered by $2f_{VS}$ [—].

but reintroduces the small-scales structures. Similarly, the addition of higher modes leads to added noise to the $2f_{VS}$-based pre-filtered reconstruction, leaving gaps and atypical patterns of decay. This is expected upon review of the individual modal energy content, shown in Figure 4.16; while the f_{KH}-based pre-filter POD energy is nearly the same as that of the unfiltered POD, the first few $2f_{VS}$-based pre-filter POD modes have significant energy with energy content declining much more rapidly. (These findings are highlighted by the 96-mode f_{KH}-based and $2f_{VS}$-based pre-filtered POD-based reconstructions included in the Supplementary Material as Video S10 and Video S11, respectively).

The aim of applying a pre-filter to the proposed POD-DMD reconstruction methodology was to (i) simplify the complexity of the final reconstruction and (ii) isolate large-scale structures. A conservative degree of filter, like that of the f_{KH}-based pre-filter, reduces the number of active frequencies nearly in half while maintaining nearly the full complexity of the flow field. However, if only large-scale structures are desirable, the aliasing of high-frequency activity permeates the lower modes preventing this feature. A much more aggressive filter, like the $2f_{VS}$-based pre-filter, significantly reduces the number of active frequencies (by a factor of nearly 30) and performs much better at isolating large-scale structures in the lower modes, making low-order reconstruction more

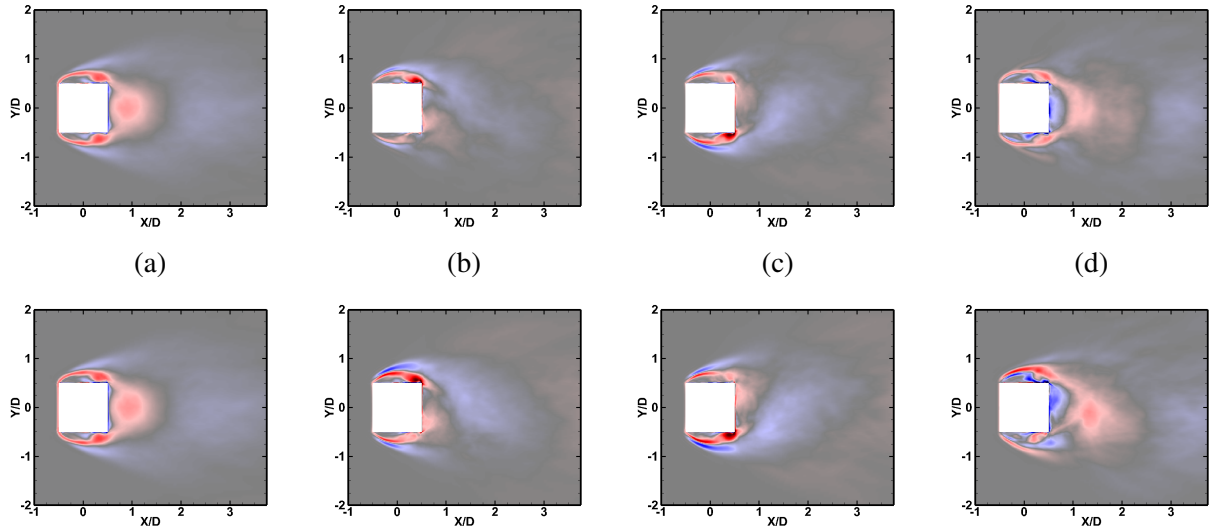

Figure 4.13: Pre-filtering comparison: mode shapes, U_m, corresponding to the first four output modes (m = 1-4) for: **(a-d)** POD pre-filtered by f_{KH}; and **(e-h)** POD pre-filtered by $2f_{VS}$, respectively.

feasible. However, this comes at the cost of forfeiture of the full complexities of the flow field.

4.4.3 Sampling Rate Reduction

Lastly, we assess the (artificial) reduction of the sampling rate on the reconstruction methodology. The Nyquist criterion states that a sampling rate double that of the highest frequency to be sampled can capture a signal effectively. Because of the pre-filtering performed in the previous subsection, it is simple to artificially alter the sampling rate used to input into POD while reconstructing the flow field. Accordingly, the sampling rate of the original dataset ($St_S = 14.55$) is reduced to $St_{S,KH} = 7.27$ and $St_{S,2VS} = 0.48$ for the f_{KH}-based and $2f_{VS}$-based pre-filters, respectively. The period over which these samples are collected is maintained the same, meaning the original number of snapshots are reduced by $\sim 50\%$ and $\sim 97\%$, accordingly.

From Figure 4.17 and Figure 4.18 it is clear that for early modes (m = 1-4) reducing the sampling rate according to the Nyquist criterion has no significant impact. The mode shapes shown in Figure 4.19 reflect the same (although small variations are noted by $m = 4$ for the $2f_{VS}$-based pre-

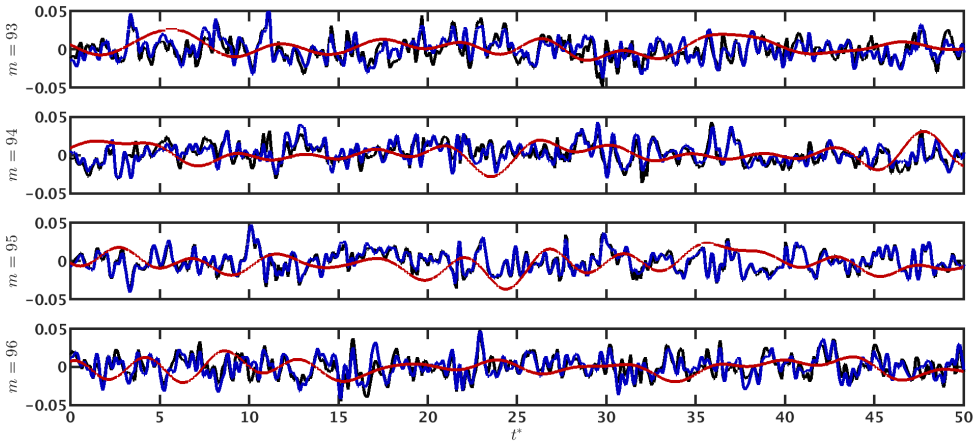

Figure 4.14: Pre-filtering comparison: temporal coefficient signals, $\mathcal{Y}_m$, corresponding to four higher-order modes ($m = 93$-96) for: unfiltered POD [—]; POD pre-filtered by f_{KH} [—]; and POD pre-filtered by $2f_{VS}$ [—].

filter mode shape from its unmodified sampling rate equivalent). The most dominant signals/modes are captured consistently regardless.

At higher modes ($m = 93$-96), the f_{KH}-based pre-filter with reduced sampling exhibits only minor discrepancies, as seen in Figure 4.20. Similarly, the structures present in the corresponding mode shapes, shown in Figure 4.21, match very consistently with their higher sampling frequency counterpart, exhibiting only minor variations in magnitude. Additional analysis of the $2f_{VS}$-based pre-filter with reduced sampling have been omitted for these modes, due to the findings of the previous subsection.

4.4.4 Integral Quantity Recovery

Another objective of this work is to demonstrate that the proposed methodology maintains sufficient accuracy for engineering purposes. Toward this end, three integral quantities are calculated based upon the pressure field surrounding the square cylinder: (i) mean drag coefficient, $\overline{C_D}$; (ii) root-mean-square drag coefficient, C'_D; and (iii) root-mean-square lift coefficient, C'_L. To obtain these parameters, a trapezoidal integration method is applied to the pressure values at the square cylinder surface, reducing the pertinent state-coordinates from $89,298$ to 396. We then compare

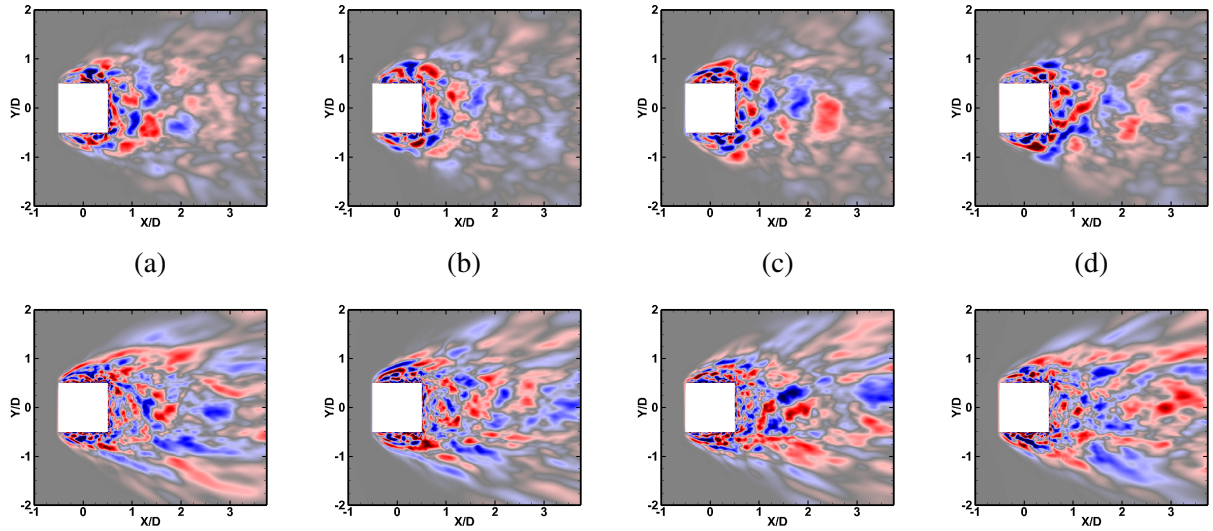

Figure 4.15: Pre-filtering comparison: mode shapes, U_m, corresponding to four higher-order modes ($m = 93$-96) for: **(a-d)** POD pre-filtered by f_{KH}; and **(e-h)** POD pre-filtered by $2f_{VS}$, respectively.

the original dataset with the reconstructed field as a function of the order of the representation.

As shown in Figure 4.22, these integral quantities can be sufficiently captured with very few modes. The mean drag coefficient, $\overline{C_D}$, is captured with sufficient accuracy before any modal reconstruction occurs, as the mean field (sometimes considered the zeroth mode) is effective in estimating $\overline{C_D}$ within $\sim 0.01\%$. Likewise, the root-mean-square lift coefficient, C_L', achieves sufficient accuracy after the first mode, estimating C_L' within $\sim 2\%$. As additional modes are added, C_L' is estimated within $\sim 0.5\%$ after 10 modes. Converging more slowly than the rest, the root-mean-square drag coefficient, C_D', is estimated within $\sim 5\%$ with the incorporation of 25 modes. This continues to improve, achieving $\sim 1\%$ with the incorporation of 92 modes.

In this work, a three-step procedure of DMD-POD-DMD is found to be well-suited toward producing reduced-order spatio-temporal representations. Toward this end, the flow field snapshots are first compiled into the data matrix, Q'.

Step 1: Pre-Filtering of Dataset (DMD)

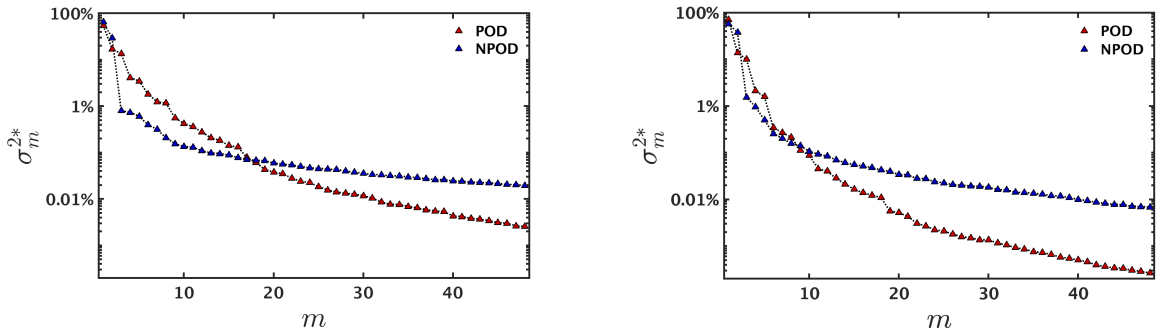

Figure 4.16: Pre-filtering comparison: (normalized) individual modal energy content, σ_m^{2*}, up to 48-modes for: **(a)** f_{KH}-based pre-filtering and **(b)** $2f_{VS}$-based pre-filtering.

i. The DMD algorithm is applied per Eqns. 4.14-4.18c.

ii. This decomposition is developed based upon a projection onto POD modes (see Eqn. 4.11 and Eqn. 4.15b) and is truncated by the rank of Q′ to obtain clear temporal characteristics.

iii. Depending on the desired fidelity of the final reconstruction, a frequency threshold, ω_T, is selected and all DMD modes corresponding to $\omega_k > \omega_T$ are disregarded.

iv. This results in a filtered data matrix, Q'_{filt}.

Step 2: Spatial Compression (POD or NPOD)

i. According to Eqn. 4.11, POD is performed upon Q'_{filt}, yielding spatial modes, $\psi_m(\vec{x})$, related amplitudes, σ_m, and temporal coefficient signals, $\mathscr{V}_m(t)$.

ii. Alternatively, NPOD can also be applied toward the same end.

iii. The number of ρ-modes is determined, commonly accomplished via an 'energy-recovery' argument described by Eqn. 4.19), for later reconstruction.

iv. The temporal coefficient matrix (V) is truncated by r, the rank of Q'_{filt}.

Step 3: Synthesizing Temporal Coefficient Functions (DMD)

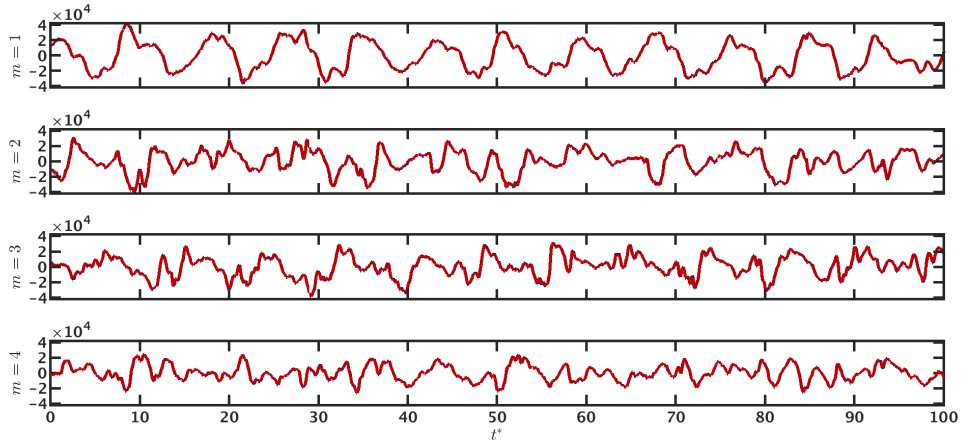

Figure 4.17: Sampling rate reduction comparison: amplified temporal coefficient signals, $\sigma_m \mathscr{V}_m$, corresponding to the first four output modes (m = 1-4) for: unfiltered POD [—]; POD pre-filtered by f_{KH} [—]; and POD pre-filtered by f_{KH} with reduced sampling [—].

i. The r-truncated temporal coefficient matrix, $\mathrm{V}^{(r)}(t)$, is transposed (i.e. $\mathscr{V}^{(r)} = [\mathrm{V}^{(r)}]^*$).

ii. The DMD algorithm is applied to $\mathscr{V}^{(r)}$, according to Eqns. 4.14-4.18c and by decomposing these signals into their DMD mode shapes, $\phi_k(\vec{x})$, initial amplitudes, b_k, and frequencies, ω_k.

iii. Temporal functions are then developed as shown in 4.20.

iv. Only the first ρ-functions are retained, corresponding to the temporal coefficient signals which relate to the retained POD mode shapes and amplitudes.

The final reduced-order spatio-temporal representations can be constructed using the retained ρ-number of POD mode shapes and amplitudes and DMD-based synthetic temporal coefficient functions. This reconstruction is produced as shown in Eqn. 4.21.

4.5 Conclusions

Reduced-order reconstructions have the potential to provide invaluable information in a real-time manner. Toward this end, it is imperative to thoroughly assess and develop robust tools that enable archiving key features for later use in various representations. The primary objective of this work is to assess different techniques and strategies for the reconstruction of wake flows using

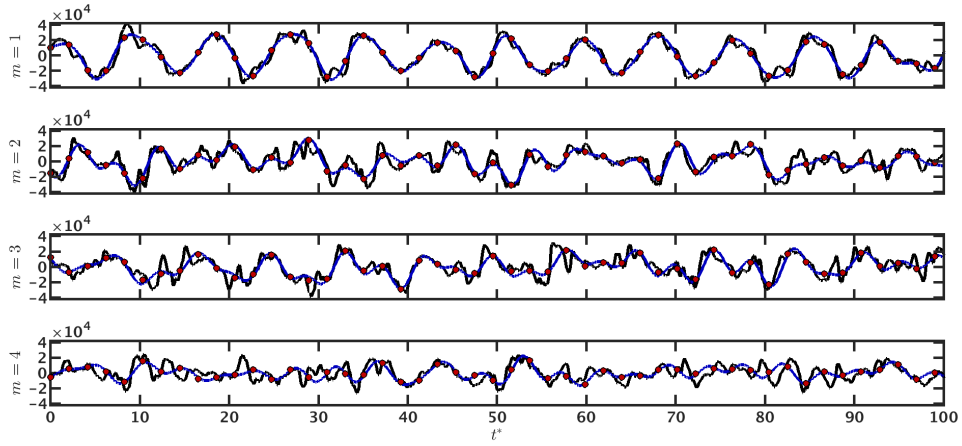

Figure 4.18: Sampling rate reduction comparison: amplified temporal coefficient signals, $\sigma_m \mathscr{V}_m$, corresponding to the first four output modes (m = 1-4) for: unfiltered POD [—]; POD pre-filtered by $2f_{VS}$ [—]; and POD pre-filtered by $2f_{VS}$ with reduced sampling [•].

fundamental modal analysis techniques. The method proposed incorporates spatial compression of snapshots via POD followed by the synthesis of temporal coefficient functions. Three aspects of this proposed method are assessed: (i) a priori local normalization of the flow field; (ii) pre-filtering of time-scales and hence length-scales; and (iii) reduction of the sampling rate. Each of these aspects highlights potential options that the end-user might want to choose between in order to obtain a reconstruction tailored to their needs.

To accomplish this, the canonical flow past a square cylinder at $Re = 22,000$ was considered. This benchmark case provides insight into many wake flow phenomena of engineering interest: massive separation; vortex shedding, secondary instabilities, and coherent structures. The necessary dataset was obtained by utilizing the PANS methodology to perform simulations with $f_k = 0.10$. This dataset consisted of snapshots of spanwise vorticity on a representative XY-plane at over $89,000$ state-coordinates over a window of nearly $5,800$ snapshots.

The main findings are as follows:

i. A priori local normalization of the flow field (implemented as NPOD, as opposed to POD), which equally distributes significance to all state-coordinates throughout the domain, has

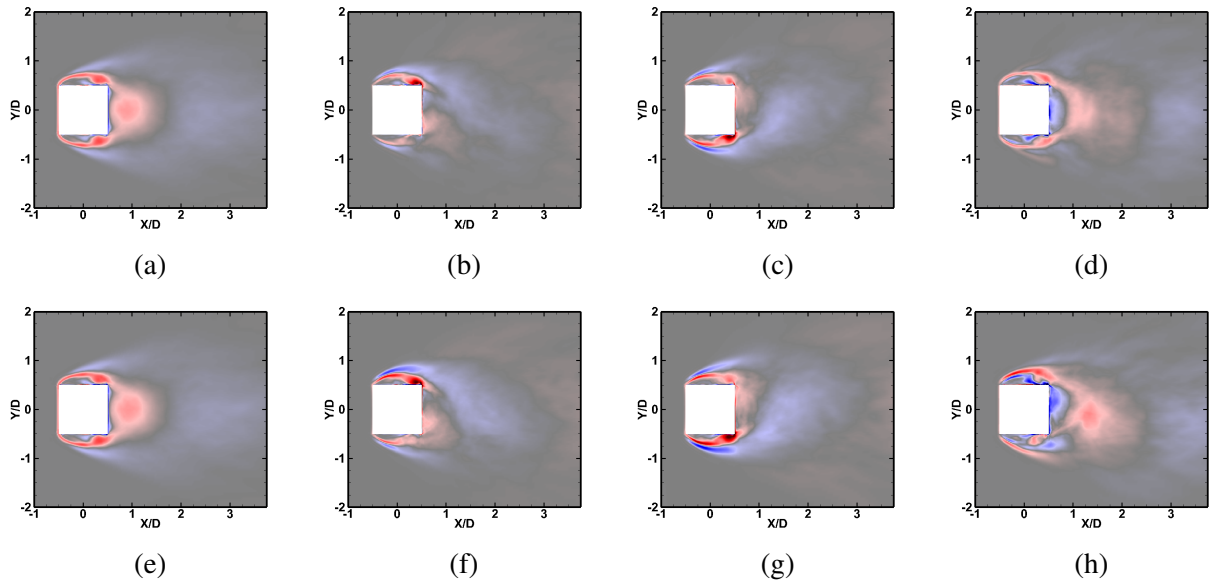

Figure 4.19: Sampling rate reduction comparison: mode shapes, U_m, corresponding to the first four output modes (m = 1-4) for: **(a-d)** POD pre-filtered by f_{KH}; and **(e-h)** POD pre-filtered by $2f_{VS}$, respectively, each with their respective reduced sampling rates.

two main effects: the prioritization of frequencies which manifest throughout the domain; and improved clarity of structures in the far-wake, which maintain recognizable structure to the downstream boundary. This comes at the cost of efficiency, at least in terms of optimal energy recovery.

ii. Pre-filtering of higher frequencies (through the use of DMD) aims to mitigate the effects of small-scales aliasing into lower modes, in addition to reducing the temporal complexity. While a conservatively prescribed filter still reduces the temporal complexity, it does not significantly prevent the aforementioned aliasing. An aggressive filter, however, further reduces the temporal complexity and better isolates large-scales, limiting the manifestation of smaller-scales to higher-order reconstructions.

iii. Reduction of the sampling rate, applied according to the Nyquist criterion as applied based upon the pre-filtered frequency cut-off, proves prudent as the effect is negligible, if any.

Overall, this work considers multiple aspects which serve to add robustness to a methodology

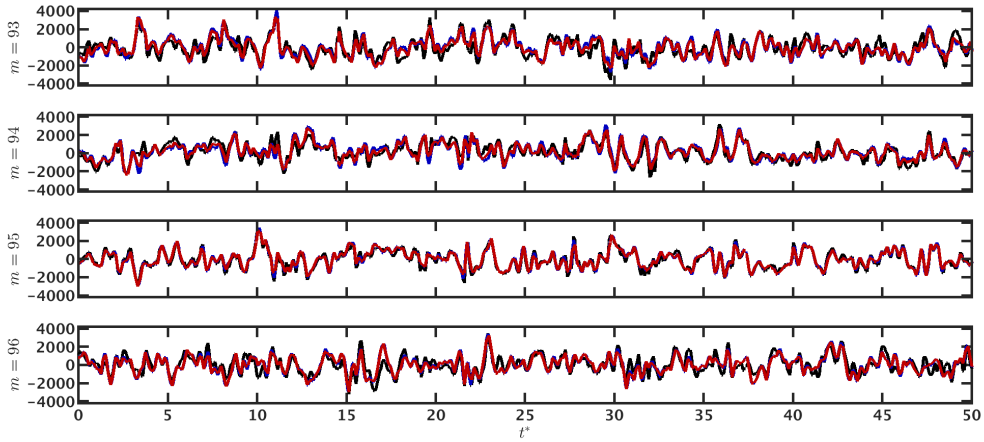

Figure 4.20: Sampling rate reduction comparison: amplified temporal coefficient signals, $\sigma_m \mathscr{V}_m$, corresponding to four higher-order modes ($m = 93$-96) for: unfiltered POD [—]; POD pre-filtered by f_{KH} [—]; and POD pre-filtered by f_{KH} with reduced sampling [—].

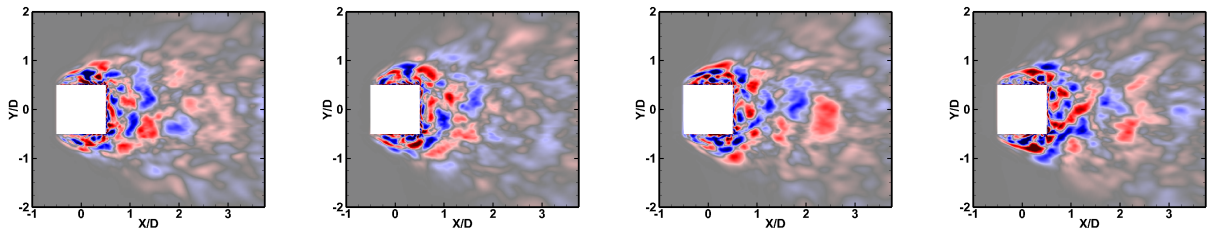

(a) (b) (c) (d)

Figure 4.21: Sampling rate reduction comparison: mode shapes, U_m, corresponding to four higher-order modes ($m = 93$-96) for: **(a-d)** POD pre-filtered by f_{KH} with sampling rate reduced.

which is readily applicable to most fluid flows.

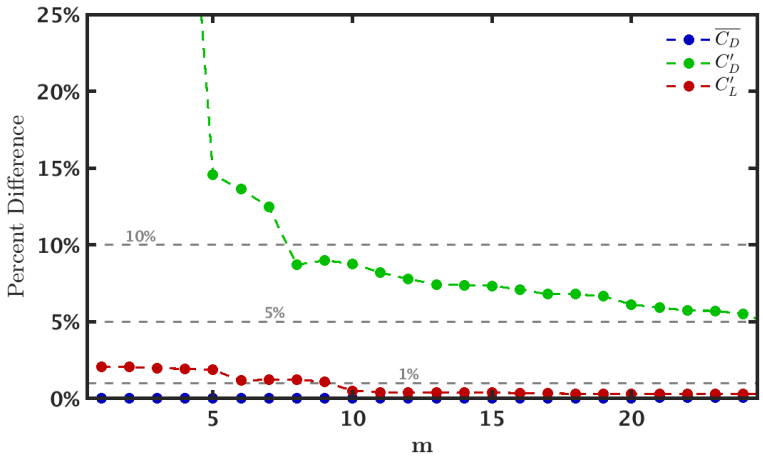

Figure 4.22: Integral quantity recovery utilizing an increasing number of modes for reduced-order reconstruction. Integral quantities shown include: mean drag coefficient, $\overline{C_D}$, root-mean-square drag coefficient, C'_D; and root-mean-square lift coefficient, C'_L.

5. SUMMARY AND CONCLUSIONS

The ultimate objective of this work is to advance the techniques available for the characterization and reconstruction of coherent structures within wake flows. Toward this end, the canonical flow past a square cylinder has been utilized in three key configurations: (i) laminar-current ($Re = 200$; steady in-flow); (ii) laminar-wave ($Re = 200$; pulsatory in-flow); and (iii) turbulent-current ($Re = 22,000$; steady in-flow). While the methods used are similarly appropriate for other geometries, the flow past a square cylinder contains several flow phenomena of importance to engineering applications, namely: massive separation, vortex-shedding, secondary instabilities, and coherent structures. Adequately capturing and isolating the effects of these phenomena contribute to a fuller understanding of the critical mechanisms inherent in wake flow physics, such as those which lead to VIV.

In the first study (Chapter 3), DNS simulations of steady and pulsatory laminar flows ($Re = 200$; $x_e/D = 0.20$; and $0 \leq f_e/f_0 \leq 4$) were performed to obtain insight into the force coefficients (and their spectra) along with the development of coherent structures under different forcing regimes. The flows within the first of these regimes, pre-lock-in ($f_e/f_0 < 1.6$), maintain a shedding frequency, f_s, which is equal to that of the natural shedding frequency, f_0. This is caused by the interruption of the vortex-structure development due to the weak pulsations, leading to the manifestation of the underlying instability. Because of these interruptions, the characteristics of these vortex-structures vary considerably causing the primary peak in the C_L PSD to be only one decade larger than its neighboring minima in addition to generating additional combination frequencies. As the pulsations grow stronger/faster, there is a very sharp transition into the second of these regimes, lock-in ($1.6 \leq f_e/f_0 \leq 2.4$), where both the shedding and combination frequencies become functions of the forcing. Within this regime, pulsations have become sufficiently strong such that the vortex-structures' development is affected without full interruption. This leads to a natural rhythm which amplifies the forcing that the vortex-structures impart upon the body. The C_L PSD peaks within this regime are four decades larger than that of their neighboring minima and the $\overline{C_D}$

and C_L' values are notably higher than in other regimes. The transition beyond lock-in (into post-lock-in, $f_e/f_0 < 2.4$) is much more gradual. In this regime, peaks of the C_L PSD broaden until fully separating into multiple discrete peaks (i.e. reemergence of the combination frequencies). The increasingly strong pulsations begin to decouple the effects of vortex-structures above/below the square cylinder from those downstream. This gives rise to a symmetry in the developing structures, leading to lesser net-forcing exerted on the body and causing f_s to tend toward f_0.

In the following study (Chapter 3), criteria are sought to establish optimal degrees of scale-resolution for various QoI in turbulent wake flows. Scale-resolving simulations of turbulence are intended to provide an optimal balance between computational effort and accuracy, depending on the complexity of the flow and the prescribed degree of accuracy of QoI. The secondary objective of this study was to formulate a procedure for quantitative assessment of large-scale coherent structures for precise comparison of features across different SRS computations. To investigate these aspects of SRS, the PANS technique – a bridging-SRS approach – is employed for simulations of the canonical flow past a square cylinder at $Re = 22,000$. As is typical in most bluff body wakes, this flow exhibits two instabilities which are found to define these optimal cut-offs: the von Kármán vortex-shedding (VS) instability and the Kelvin-Helmholtz (KH) instability. These simulations are performed for various degrees of scale-resolution, characterized by $f_k \in [0.10, 0.50]$, employing the k-ω closure. The global flow parameters (i.e. St, C_D, C_L,) are first investigated. It is found that even the $f_k = 0.50$ simulation achieves results comparable to LES, while the lower f_k simulations tend toward DNS results. Thus, accurate results are obtained at a very reasonable cost. For adequately computing these parameters, it suffices to capture the vortex-shedding frequency (f_{VS}) upon which these features are almost exclusively dependent. Assessment of the mean streamwise velocity and normal Reynolds stress profiles along the centerline follows. Gradual improvement with increasing scale-resolution is evident; likely owing to the increased influence of the KH instability. Finally, streamwise velocity probe spectra are compared. All scale-resolutions accurately capture f_{VS}, however, the Kelvin-Helmholtz frequency (f_{KH}) is not well replicated by coarse resolution simulations ($f_k > 0.3$). The KH instability is unable to be captured in these coarser resolu-

tion simulations due to the insufficient effective (computational) Reynolds number in the region of interest.

Two methods are then presented for quantitative characterization of coherent structures – Fourier-SPOD and Chebyshev-SPOD – utilizing Fourier and Chebyshev decomposition, respectively, in the cross-stream direction before performing SPOD in the streamwise direction. Different mode shapes are identified using FSPOD and CSPOD at f_{VS} and in terms of the characteristic wavelength (λ) corresponding to their respective basis functions in the cross-stream direction. For $\lambda/D \gtrsim 1$, the mode shapes and energy content are captured consistently for all f_k simulations in the study. For $\lambda/D < 1$, increased scale-resolution is required.

In the final study (Chapter 4), a methodology for reduced-order reconstruction is proposed. This method utilizes POD for spatial compression of snapshots and is followed by DMD to synthesize temporal coefficient functions. Three aspects of this method are then assessed, including: (i) a priori normalization of the flow field; (ii) pre-filtering of frequencies; and (iii) reduction of the sampling rate. Each aspect highlights potential variations of the method that the end-user may wish to select to obtain a reconstruction tailored to their priorities. To demonstrate the methodology and compare the effect of varying these aspects, a dataset obtained using the PANS k-ω model ($f_k = 0.1$) from the previous study is used, consisting of snapshots of spanwise vorticity on a representative XY-plane.

A priori normalization of the flow field is assessed by comparing the effect of using POD versus NPOD as the primary means of spatial compression. This effectively distributes significance to all state-coordinates throughout the domain and is found to have two main effects: (i) frequencies which manifest throughout the domain are prioritized; and (ii) structures in the far-wake remain clearer, dissipating less quickly than their POD counterparts. Next, pre-filtering of higher frequencies (using DMD) is assessed, aiming to prevent aliasing of small-scales into lower modes and also reduce temporal complexity. Conservative application of such a filter ($St > f_{KH}$) is found to reduce the degree of temporal complexity but did not significantly prevent undesirable aliasing effects. However, a much more aggressive filter ($St > 2f_{VS}$) is found to further reduce the temporal

complexity and better isolate large-scale structures, limiting small-scales to higher modes. Finally, the reduction of the sampling rate is compared with that of the original sampling rate. Based on the Nyquist criterion relative to the pre-filtered frequency cut-off, this change appears to have minimal impact, if any, on relevant output modes.

REFERENCES

[1] S. Minewitsch, R. Franke, and W. Rodi, "Numerical investigation of laminar vortex-shedding flow past a square cylinder oscillating in line with the mean flow," Journal of Fluids and Structures, vol. 8, no. 7, pp. 787–802, 1994.

[2] N. Steggel and N. Rockliff, "Simulation of the effects of body shape on lock-in characteristics in pulsating flow by the discrete vortex method," Journal of Wind Engineering and Industrial Aerodynamics, vol. 69-71, pp. 317–329, 1997.

[3] A. Sohankar, C. Norberg, and L. Davidson, "Simulation of three-dimensional flow around a square cylinder at moderate Reynolds numbers," Physics of Fluids, vol. 11, no. 2, pp. 288–306, 1999.

[4] R. Franke, W. Rodi, and B. Schönung, "Numerical calculation of laminar vortex-shedding flow past cylinders," Journal of Wind Engineering and Industrial Aerodynamics, vol. 35, no. C, pp. 237–257, 1990.

[5] A. Okajima, "Numerical analysis of flow around an oscillating cylinder," in Proc. Sixth International Conference on Flow Induced Vibration, London, UK, 1995, 1995.

[6] Okajima A, "Strouhal number of rectangular cylinders," Journal of Fluid Mechanics, vol. 123, pp. 379–398, 1982.

[7] H. Jiang and L. Cheng, "Hydrodynamic characteristics of flow past a square cylinder at moderate Reynolds numbers," Physics of Fluids, vol. 30, no. 10, p. 104107, 2018.

[8] S. C. Luo, Y. T. Chew, and Y. T. Ng, "Characteristics of square cylinder wake transition flows," Physics of Fluids, vol. 15, no. 9, pp. 2549–2559, 2003.

[9] S. C. Luo, X. H. Tong, and B. C. Khoo, "Transition phenomena in the wake of a square cylinder," Journal of Fluids and Structures, vol. 23, no. 2, pp. 227–248, 2007.

[10] A. K. Saha, G. Biswas, and K. Muralidhar, "Three-dimensional study of flow past a square cylinder at low Reynolds numbers," International Journal of Heat and Fluid Flow, vol. 24, no. 1, pp. 54–66, 2003.

[11] B. van Oudheusden, F. Scarano, N. van Hinsberg, and E. Roosenboom, "Quantitative visualization of the flow around a square-section cylinder at incidence," Journal of Wind Engineering and Industrial Aerodynamics, vol. 96, no. 6, pp. 913–922, 2008.

[12] D. A. Lyn, S. Einav, W. Rodi, and J.-H. Park, "A laser-doppler velocimetry study of ensemble-averaged characteristics of the turbulent near wake of a square cylinder," Journal of Fluid Mechanics, vol. 304, pp. 285–319, 1995.

[13] M. Minguez, C. Brun, R. Pasquetti, and E. Serre, "Experimental and high-order LES analysis of the flow in near-wall region of a square cylinder," International Journal of Heat and Fluid Flow, vol. 32, no. 3, pp. 558–566, 2011. 8th International Symposium on Engineering Turbulence Modelling and Measurements, Marseille, France, June 9-11, 2010.

[14] P. Meliga, O. Cadot, and E. Serre, "Experimental and theoretical sensitivity analysis of turbulent flow past a square cylinder," Flow, Turbulence and Combustion, vol. 97, no. 4, pp. 987–1015, 2016.

[15] S. C. Yen and C. W. Yang, "Flow patterns and vortex shedding behavior behind a square cylinder," Journal of Wind Engineering and Industrial Aerodynamics, vol. 99, no. 8, pp. 868–878, 2011.

[16] F. Trias, A. Gorobets, and A. Oliva, "Turbulent flow around a square cylinder at Reynolds number 22,000: A DNS study," Computers Fluids, vol. 123, pp. 87–98, 2015.

[17] R. W. C. P. Verstappen and A. E. P. Veldman, "Spectro-consistent discretization of Navier-Stokes: a challenge to RANS and LES," Journal of Engineering Mathematics, vol. 34, no. 1, pp. 163–179, 1998.

[18] Y. Cao, T. Tamura, and H. Kawai, "Spanwise resolution requirements for the simulation of high-Reynolds-number flows past a square cylinder," Computers and Fluids, vol. 196, p. 104320, 2020.

[19] J. Ochoa and N. Fueyo, "Large eddy simulation of the flow past a square cylinder," PHOENICS Journal of Computational Fluid Dynamics and its Applications, vol. 17, 2004.

[20] C. Fureby, G. Tabor, H. G. Weller, and A. D. Gosman, "Large eddy simulations of the flow around a square prism," AIAA Journal, vol. 38, no. 3, pp. 442–452, 2000.

[21] W. Rodi, "Comparison of LES and RANS calculations of the flow around bluff bodies," Journal of Wind Engineering and Industrial Aerodynamics, vol. 69–71, pp. 55–75, 1997.

[22] A. Sohankar, L. Davidson, and C. Norberg, "Large eddy simulation of flow past a square cylinder: Comparison of different subgrid scale models," Journal of Fluids Engineering, vol. 122, pp. 39–47, 11 1999.

[23] Y. Cao and T. Tamura, "Large-eddy simulations of flow past a square cylinder using structured and unstructured grids," Computers & Fluids, vol. 137, no. July, pp. 36–54, 2016.

[24] C. Brun, S. Aubrun, T. Goossens, and P. Ravier, "Coherent structures and their frequency signature in the separated shear layer on the sides of a square cylinder," Flow, Turbulence and Combustion, vol. 81, no. 1, pp. 97–114, 2008.

[25] A. K. M. F. Hussain, "Coherent structures – reality and myth," Physics of Fluids, vol. 26, no. 10, pp. 2816–2850, 1983.

[26] H. Branover, A. Eidelman, E. Golbraikh, and S. Moiseyev, Turbulence and Structures: Chaos, Fluctuations, and Helical Self-organization in Nature and the Laboratory. Academic Press, 1999.

[27] S. B. Pope, Turbulent Flows. Cambridge University Press, 2000.

[28] R. T. Pierrehumbert, "Large-scale horizontal mixing in planetary atmospheres," Physics of Fluids A: Fluid Dynamics, vol. 3, no. 5, pp. 1250–1260, 1991.

[29] J. L. J. Schols, "The detection and measurement of turbulent structures in the atmospheric surface layer," Boundary-Layer Meteorology, vol. 29, no. 1, pp. 39–58, 1984.

[30] K. Träumner, T. Damian, C. Stawiarski, and A. Wieser, "Turbulent structures and coherence in the atmospheric surface layer," Boundary-Layer Meteorology, vol. 154, no. 1, pp. 1–25, 2015.

[31] D. G. Dritschel, M. de la Torre Juárez, and M. H. P. Ambaum, "The three-dimensional vortical nature of atmospheric and oceanic turbulent flows," Physics of Fluids, vol. 11, no. 6, pp. 1512–1520, 1999.

[32] H. Karimabadi, V. Roytershteyn, M. Wan, W. H. Matthaeus, W. Daughton, P. Wu, M. Shay, B. Loring, J. Borovsky, E. Leonardis, S. C. Chapman, and T. K. M. Nakamura, "Coherent structures, intermittent turbulence, and dissipation in high-temperature plasmas," Physics of Plasmas, vol. 20, no. 1, p. 012303, 2013.

[33] G. Montani and J. Petitta, "Plasma phenomenology in astrophysical systems: Radio-sources and jets," Physics of Plasmas, vol. 21, no. 6, p. 061502, 2014.

[34] R. J. Adrian and I. Marusic, "Coherent structures in flow over hydraulic engineering surfaces," Journal of Hydraulic Research, vol. 50, no. 5, pp. 451–464, 2012.

[35] P. Holmes, J. Lumley, G. Berkooz, and C. Rowley, Turbulence, Coherent Structures, Dynamical Systems and Symmetry. Cambridge Monographs on Mechanics, Cambridge University Press, 2012.

[36] M. Treib, K. Bürger, F. Reichl, C. Meneveau, A. Szalay, and R. Westermann, "Turbulence visualization at the terascale on desktop PCs," IEEE Transactions on Visualization and Computer Graphics, vol. 18, no. 12, pp. 2169–2177, 2012.

[37] K. T. Carlberg, A. Jameson, M. J. Kochenderfer, J. Morton, L. Peng, and F. D. Witherden, "Recovering missing CFD data for high-order discretizations using deep neural networks and dynamics learning," Journal of Computational Physics, vol. 395, pp. 105 – 124, 2019.

[38] P. K. Yeung, "Advancing understanding of turbulence through extreme-scale computation," in APS Division of Fluid Dynamics Meeting Abstracts, APS Meeting Abstracts, p. E01.001, Nov. 2019.

[39] Z. Wu, T. A. Zaki, and C. Meneveau, "Data compression for turbulence databases using spatiotemporal subsampling and local resimulation," Phys. Rev. Fluids, vol. 5, p. 064607, Jun 2020.

[40] G. H. Lee, "Trailing vortex wakes," The Aeronautical Journal (1968), vol. 79, no. 777, pp. 377–388, 1975.

[41] R. L. Ash and Z. C. Zheng, "Numerical simulations of commercial aircraft wakes subjected to airport surface weather conditions," Journal of Aircraft, vol. 35, no. 1, pp. 18–26, 1998.

[42] V. J. Rossow, "Use of individual flight corridors to avoid vortex wakes," Journal of Aircraft, vol. 40, no. 2, pp. 225–231, 2003.

[43] V. Rossow and L. Meyn, "Guidelines for avoiding vortex wakes during use of closely-spaced parallel runways," p. 6907, 2012. 26th AIAA Applied Aerodynamics Conference, Honolulu, HI, August 18-21, 2008.

[44] R. J. Barthelmie, K. Hansen, S. T. Frandsen, O. Rathmann, J. G. Schepers, W. Schlez, J. Phillips, K. Rados, A. Zervos, E. S. Politis, and P. K. Chaviaropoulos, "Modelling and measuring flow and wind turbine wakes in large wind farms offshore," Wind Energy, vol. 12, no. 5, pp. 431–444, 2009.

[45] R. J. Barthelmie and L. E. Jensen, "Evaluation of wind farm efficiency and wind turbine wakes at the Nysted offshore wind farm," Wind Energy, vol. 13, no. 6, pp. 573–586, 2010.

[46] K. S. Hansen, R. J. Barthelmie, L. E. Jensen, and A. Sommer, "The impact of turbulence intensity and atmospheric stability on power deficits due to wind turbine wakes at Horns Rev wind farm," Wind Energy, vol. 15, no. 1, pp. 183–196, 2012.

[47] Y.-T. Wu and F. Porté-Agel, "Modeling turbine wakes and power losses within a wind farm using les: An application to the Horns Rev offshore wind farm," Renewable Energy, vol. 75, pp. 945 – 955, 2015.

[48] J. Rottman, D. Dommermuth, G. Innis, T. O'Shea, and E. Novikov, "Numerical simulation of wakes in a weakly stratified fluid," 07 2002. 24th Symposium on Naval Hydrodynamics, Fukuoka, Japan, July 8-13, 2002.

[49] A. Conway, J. Binns, D. Ranmuthugala, and M. Renilson, "Experimental and numerical analysis of submarine mast surface wakes," pp. 1–12, 2015. Proceedings of the Pacific International Maritime Conference, Sydney Exhibition Centre, Glebe Island, Sydney, October 6-8, 2015.

[50] J. Ren and J. Wang, "Simulation of SAR images of submarine wakes," in 2016 IEEE International Geoscience and Remote Sensing Symposium (IGARSS), pp. 906–909, 2016.

[51] K. Lambrakos, K. Steele, and L. Finn, "Wake and shielding effects on hydrodynamic loading," 1989. Proceedings of E&P forum workshop on wave and current kinematics and loading, Paris, France October 25-26, 1989.

[52] F. V. D. Abeele, J. V. Voorde, and J. Kennedylaan, "Flow induced oscillations of marine risers with wake interference," 2010. Proceedings of the COMSOL Conference, Paris, France, 2010.

[53] T. Sebastian and M. Lackner, "Development of a free vortex wake method code for offshore floating wind turbines," Renewable Energy, vol. 46, pp. 269 – 275, 2012.

[54] K. Narendran, M. Guan, P. Ma, A. Choudhary, A. Hussain, and R. Jaiman, "Control of vortex-induced motion in multi-column offshore platform by near-wake jets," Computers Fluids, vol. 167, pp. 111 – 128, 2018.

[55] T. S. Fowler, IV, F. D. Witherden, and S. S. Girimaji, "Pulsating Flow Past a Square Cylinder: Analysis of Force Coefficient Spectra and Vortex Structure Development," Journal of Fluids Engineering, vol. 142, 10 2020.

[56] T. S. Fowler, IV, F. D. Witherden, and S. S. Girimaji, "Partially-averaged Navier-Stokes simulations of turbulent flow past a square cylinder: Comparative assessment of statistics & coherent structures at different resolutions," submitted to Physics of Fluids, 2020.

[57] Z. Huang, B. O'Donnell, T. Yung, and S. Slocum, "An advanced test method to determine viscous damping of floating structures," vol. 29th International Conference on Ocean, Offshore and Arctic Engineering: Volume 1 of International Conference on Offshore Mechanics and Arctic Engineering, pp. 665–672, 06 2010.

[58] Z. Huang, B. O'Donnell, T. Yung, and S. Slocum, "Determination of viscous damping for low frequency motions of floating structures," vol. Volume 3: Materials Technology; Jan Vugts Symposium on Design Methodology of Offshore Structures; Jo Pinkster Symposium on Second Order Wave Drift Forces on Floating Structures; Johan Wichers Symposium on Mooring of Floating Structures in Waves of International Conference on Offshore Mechanics and Arctic Engineering, pp. 953–961, 06 2011.

[59] C. Williamson and R. Govardhan, "Vortex-induced vibrations," Annual Review of Fluid Mechanics, vol. 36, pp. 413–455, 2004.

[60] P. J. Strykowski and K. R. Sreenivasan, "On the formation and suppression of vortex 'shedding' at low Reynolds numbers," Journal of Fluid Mechanics, vol. 218, p. 71–107, 1990.

[61] P. Bearman and M. Branković, "Experimental studies of passive control of vortex-induced vibration," European Journal of Mechanics - B/Fluids, vol. 23, no. 1, pp. 9 – 15, 2004. Bluff Body Wakes and Vortex-Induced Vibrations.

[62] A. Trim, H. Braaten, H. Lie, and M. Tognarelli, "Experimental investigation of vortex-induced vibration of long marine risers," Journal of Fluids and Structures, vol. 21, no. 3, pp. 335 – 361, 2005. Marine and Aeronautical Fluid-Structure Interactions.

[63] I. Korkischko and J. Meneghini, "Suppression of vortex-induced vibration using moving surface boundary-layer control," Journal of Fluids and Structures, vol. 34, pp. 259–270, 2012.

[64] O. M. Griffin and S. E. Ramberg, "Vortex shedding from a cylinder vibrating in line with an incident uniform flow," Journal of Fluid Mechanics, vol. 75, no. 2, pp. 257–271, 1976.

[65] Y. Tanida, A. Okajima, and Y. Watanabe, "Stability of a circular cylinder oscillating in uniform flow or in a wake," Journal of Fluid Mechanics, vol. 61, no. 4, pp. 769–784, 1973.

[66] C. H. K. Williamson, "Three-dimensional wake transition," Journal of Fluid Mechanics, vol. 328, p. 345–407, 1996.

[67] S. Dutta, P. K. Panigrahi, and K. Muralidhar, "Sensitivity of a square cylinder wake to forced oscillations," Journal of Fluids Engineering, vol. 129, no. 7, p. 852, 2007.

[68] A. Ongoren and D. Rockwell, "Flow structure from an oscillating cylinder part 1. mechanisms of phase shift and recovery in the near wake," Journal of Fluid Mechanics, vol. 191, p. 197–223, 1988.

[69] A. Ongoren and D. Rockwell, "Flow structure from an oscillating cylinder part 2. mode competition in the near wake," Journal of Fluid Mechanics, vol. 191, p. 225–245, 1988.

[70] C. H. Williamson and A. Roshko, "Vortex formation in the wake of an oscillating cylinder," Journal of Fluids and Structures, vol. 2, no. 4, pp. 355–381, 1988.

[71] P. Welch, "The use of fast fourier transform for the estimation of power spectra: A method based on time averaging over short, modified periodograms," IEEE Transactions on Audio and Electroacoustics, vol. 15, pp. 70–73, June 1967.

[72] H. G. Weller, G. Tabor, H. Jasak, and C. Fureby, "A tensorial approach to computational continuum mechanics using object-oriented techniques," Computers in Physics, vol. 12, no. 6, p. 620, 1998.

[73] R. Issa, "Solution of the implicitly discretised fluid flow equations by operator-splitting," Journal of Computational Physics, vol. 62, no. 1, pp. 40–65, 1986.

[74] M. Provansal, C. Mathis, and L. Boyer, "Bénard-von Kármán instability: transient and forced regimes," Journal of Fluid Mechanics, vol. 182, p. 1–22, 1987.

[75] E. Naudascher, "Flow-induced streamwise vibrations of structures," Journal of Fluids and Structures, vol. 1, no. 3, pp. 265 – 298, 1987.

[76] B. Cabral and L. C. Leedom, "Imaging vector fields using line integral convolution," in Proceedings of the 20th Annual Conference on Computer Graphics and Interactive Techniques, SIGGRAPH '93, (New York, NY, USA), p. 263–270, Association for Computing Machinery, 1993.

[77] S. S. Girimaji, "Partially averaged Navier-Stokes (PANS) approach: A RANS to LES bridging model," APS, vol. 56, pp. EC–001, 2003.

[78] S. S. Girimaji, "Partially-averaged Navier-Stokes model for turbulence: A Reynolds-averaged Navier-Stokes to direct numerical simulation bridging method," Journal of Applied Mechanics, vol. 73, pp. 413–421, 11 2005.

[79] S. S. Girimaji, E. Jeong, and R. Srinivasan, "Partially averaged Navier-Stokes method for turbulence: Fixed point analysis and comparison with unsteady partially averaged Navier-Stokes," Journal of Applied Mechanics, vol. 73, pp. 422–429, 11 2005.

[80] R. Schiestel and A. Dejoan, "Towards a new partially integrated transport model for coarse grid and unsteady turbulent flow simulations," Theoretical and Computational Fluid Dynamics, vol. 18, no. 6, pp. 443–468, 2005.

[81] S. Singha, K. K. Nagarajan, and K. P. Sinhamahapatra, "Numerical study of two-dimensional flow around two side-by-side circular cylinders at low Reynolds numbers," Physics of Fluids, vol. 28, no. 5, p. 053603, 2016.

[82] T. K. Sengupta and A. Gullapalli, "Enstrophy-based proper orthogonal decomposition of flow past rotating cylinder at super-critical rotating rate," Physics of Fluids, vol. 28, no. 11, p. 114107, 2016.

[83] X. Ma and A. Schröder, "Analysis of flapping motion of reattaching shear layer behind a two-dimensional backward-facing step," Physics of Fluids, vol. 29, no. 11, p. 115104, 2017.

[84] F. Wang and K. M. Lam, "Geometry effects on mean wake topology and large-scale coherent structures of wall-mounted prisms," Physics of Fluids, vol. 31, no. 12, p. 125109, 2019.

[85] A. Desai, S. Mittal, and S. Mittal, "Experimental investigation of vortex shedding past a circular cylinder in the high subcritical regime," Physics of Fluids, vol. 32, no. 1, p. 014105, 2020.

[86] Y. Fan, C. Xia, S. Chu, Z. Yang, and O. Cadot, "Experimental and numerical analysis of the bi-stable turbulent wake of a rectangular flat-backed bluff body," Physics of Fluids, vol. 32, no. 10, p. 105111, 2020.

[87] A. Towne, O. T. Schmidt, and T. Colonius, "Spectral proper orthogonal decomposition and its relationship to dynamic mode decomposition and resolvent analysis," Journal of Fluid Mechanics, vol. 847, pp. 821–867, 2018.

[88] M. Germano, "Turbulence: the filtering approach," Journal of Fluid Mechanics, vol. 238, pp. 325–336, 1992.

[89] S. Lakshmipathy and S. S. Girimaji, "Partially-averaged Navier-Stokes method for turbulent flows: k-ω model implementation," vol. 3, p. 119, 01 2006. 44th AIAA Aerospace Sciences Meeting and Exhibit, Reno, NV, January 9–12, 2006.

[90] D. C. Wilcox, "Reassessment of the scale-determining equation for advanced turbulence models," AIAA Journal, vol. 26, no. 11, pp. 1299–1310, 1988.

[91] E. Jeong and S. Girimaji, "Partially averaged Navier–Stokes (PANS) method for turbulence simulations-—flow past a square cylinder," Journal of Fluids Engineering, vol. 132, p. 121203, 12 2010.

[92] D. A. Reyes, J. M. Cooper, and S. S. Girimaji, "Characterizing velocity fluctuations in partially resolved turbulence simulations," Physics of Fluids, vol. 26, no. 8, p. 085106, 2014.

[93] F. S. Pereira, L. Eça, G. Vaz, and S. S. Girimaji, "Challenges in scale-resolving simulations of turbulent wake flows with coherent structures," Journal of Computational Physics, vol. 363, pp. 98–115, 2018.

[94] S. S. Girimaji and K. S. Abdol-Hamid, Partially-Averaged Navier Stokes Model for Turbulence: Implementation and Validation, p. 502. 2005. 43rd AIAA Aerospace Sciences Meeting and Exhibit, Reno, NV, January 10–13, 2005.

[95] Y. Qian, T. Wang, Y. Yuan, and Y. Zhang, "Comparative study on wind turbine wakes using a modified partially-averaged Navier-Stokes method and large eddy simulation," Energy, vol. 206, p. 118147, 2020.

[96] R. Bensow and M. van den Boogaard, "Using a PANS simulation approach for the transient flow around the Japan Bulk Carrier," Journal of Ship Research, vol. 63, no. 2, pp. 123–129, 2019.

[97] J. Zhang, G. Minelli, A. N. Rao, B. Basara, R. Bensow, and S. Krajnović, "Comparison of PANS and LES of the flow past a generic ship," Ocean Engineering, vol. 165, pp. 221–236, 2018.

[98] B. Ji, X. Luo, Y. Wu, X. Peng, and H. Xu, "Partially-averaged Navier–Stokes method with modified k–ε model for cavitating flow around a marine propeller in a non-uniform wake," International Journal of Heat and Mass Transfer, vol. 55, no. 23, pp. 6582–6588, 2012.

[99] S. Krajnović, R. Lárusson, and B. Basara, "Superiority of PANS compared to LES in predicting a rudimentary landing gear flow with affordable meshes," International Journal of Heat and Fluid Flow, vol. 37, pp. 109–122, 2012.

[100] A. N. Rao, G. Minelli, J. Zhang, B. Basara, and S. Krajnović, "Investigation of the near-wake flow topology of a simplified heavy vehicle using PANS simulations," Journal of Wind Engineering and Industrial Aerodynamics, vol. 183, pp. 243–272, 2018.

[101] A. Rao, G. Minelli, B. Basara, and S. Krajnović, "On the two flow states in the wake of a hatchback ahmed body," Journal of Wind Engineering and Industrial Aerodynamics, vol. 173, pp. 262–278, 2018.

[102] J. Tschepe, D. Fischer, C. N. Nayeri, C. O. Paschereit, and S. Krajnovic, "Investigation of high-speed train drag with towing tank experiments and CFD," Flow, Turbulence and Combustion, vol. 102, no. 2, pp. 417–434, 2019.

[103] F. Pereira, G. Vaz, L. Eça, and S. Girimaji, "Simulation of the flow around a circular cylinder at Re=3900 with partially-averaged Navier-Stokes equations," International Journal of Heat and Fluid Flow, vol. 69, pp. 234–246, 2018.

[104] F. S. Pereira, L. Eça, G. Vaz, and S. S. Girimaji, "On the simulation of the flow around a circular cylinder at Re=140,000," International Journal of Heat and Fluid Flow, vol. 76, pp. 40–56, 2019.

[105] D. Luo, C. Yan, H. Liu, and R. Zhao, "Comparative assessment of PANS and DES for simulation of flow past a circular cylinder," Journal of Wind Engineering and Industrial Aerodynamics, vol. 134, pp. 65–77, 2014.

[106] B. Basara, Z. Pavlovic, and S. S. Girimaji, "A new approach for the calculation of the cut-off resolution parameter in bridging methods for turbulent flow simulation," International Journal of Heat and Fluid Flow, vol. 74, pp. 76–88, 2018.

[107] A. Chakraborty and H. Warrior, "Study of turbulent flow past a square cylinder using partially-averaged Navier-Stokes method in OpenFOAM," Proceedings of the Institution of Mechanical Engineers, Part C: Journal of Mechanical Engineering Science, vol. 234, no. 14, pp. 2821–2832, 2020.

[108] P. Ranjan and A. Dewan, "A PANS study of fluid flow and heat transfer from a square cylinder approaching a plane wall," International Journal of Thermal Sciences, vol. 120, pp. 321–336, 2017.

[109] P. Ranjan and A. Dewan, "Effect of side ratio on fluid flow and heat transfer from rectangular cylinders using the PANS method," International Journal of Heat and Fluid Flow, vol. 61, pp. 309–322, 2016.

[110] P. Ranjan and A. Dewan, "Partially averaged Navier Stokes simulation of turbulent heat transfer from a square cylinder," International Journal of Heat and Mass Transfer, vol. 89, pp. 251–266, 2015.

[111] C.-S. Song and S.-O. Park, "Numerical simulation of flow past a square cylinder using partially-averaged Navier–Stokes model," Journal of Wind Engineering and Industrial Aerodynamics, vol. 97, no. 1, pp. 37–47, 2009.

[112] C. Kamble and S. S. Girimaji, "Characterization of coherent structures in turbulent wake of a sphere using partially averaged Navier-Stokes (PANS) simulations," submitted to Physics of Fluids, 2020.

[113] F. R. Menter, "Two-equation eddy-viscosity turbulence models for engineering applications," AIAA Journal, vol. 32, no. 8, pp. 1598–1605, 1994.

[114] F. M. White, Fluid Mechanics. McGraw-Hill, New York, 5 ed., 2003.

[115] J. L. Lumley, "The structure of inhomogeneous turbulent flows," Atmospheric Turbulence and Radio Wave Propagation, pp. 166–178, 1967.

[116] G. Berkooz, P. Holmes, and J. L. Lumley, "The proper orthogonal decomposition in the analysis of turbulent flows," Annual Review of Fluid Mechanics, vol. 25, no. 1, pp. 539–575, 1993.

[117] K. Taira, S. L. Brunton, S. T. M. Dawson, C. W. Rowley, T. Colonius, B. J. McKeon, O. T. Schmidt, S. Gordeyev, V. Theofilis, and L. S. Ukeiley, "Modal analysis of fluid flows: An overview," AIAA Journal, vol. 55, no. 12, pp. 4013–4041, 2017.

[118] B. Podvin and Y. Fraigneau, "A few thoughts on proper orthogonal decomposition in turbulence," Physics of Fluids, vol. 29, no. 2, p. 020709, 2017.

[119] L. Sirovich, "Turbulence and the dynamics of coherent structures, Part I: Coherent structures," Quarterly of Applied Mathematics, vol. 45, no. 3, pp. 561–571, 1987.

[120] P. J. Schmid, "Dynamic mode decomposition of numerical and experimental data," Journal of Fluid Mechanics, vol. 656, pp. 5–28, 2010.

[121] J. H. Citriniti and W. K. George, "Reconstruction of the global velocity field in the axisymmetric mixing layer utilizing the proper orthogonal decomposition," Journal of Fluid Mechanics, vol. 418, pp. 137–166, 2000.

[122] P. J. Schmid and D. S. Henningson, Stability and Transition in Shear Flows. Springer, New York, 2001.

[123] G. Berkooz, P. Holmes, and J. L. Lumley, "The proper orthogonal decomposition in the analysis of turbulent flows," Annual Review of Fluid Mechanics, vol. 25, no. 1, pp. 539–575, 1993.

[124] N. Ahmed and K. R. Rao, Orthogonal Transforms for Digital Signal Processing. Springer-Verlag, New York, 1975.

[125] R. B. Ash and M. F. Gardner, Topics in Stochastic Processes. Academic Press, New York, 1975.

[126] K. Fukunaga, Introduction to Statistical Pattern Recognition. Academic Press, New York, 2 ed., 1990.

[127] W. Zhou, H. Chen, Y. Liu, X. Wen, and D. Peng, "Unsteady analysis of adiabatic film cooling effectiveness for discrete hole with oscillating mainstream flow," Physics of Fluids, vol. 30, no. 12, p. 127103, 2018.

[128] J. Garicano-Mena, B. Li, E. Ferrer, and E. Valero, "A composite dynamic mode decomposition analysis of turbulent channel flows," Physics of Fluids, vol. 31, no. 11, p. 115102, 2019.

[129] P. Kumar, N. P. Manelil, and S. Tiwari, "Effects of shear intensity and aspect ratio on three-dimensional wake characteristics of flow past surface mounted circular cylinder," Physics of Fluids, vol. 31, no. 4, p. 043602, 2019.

[130] R. Pain, P.-E. Weiss, S. Deck, and J.-C. Robinet, "Large scale dynamics of a high Reynolds number axisymmetric separating/reattaching flow," Physics of Fluids, vol. 31, no. 12, p. 125119, 2019.

[131] A. Alessandri, P. Bagnerini, M. Gaggero, D. Lengani, and D. Simoni, "Dynamic mode decomposition for the inspection of three-regime separated transitional boundary layers using a least squares method," Physics of Fluids, vol. 31, no. 4, p. 044103, 2019.

[132] Y. Ohmichi, K. Kobayashi, and M. Kanazaki, "Numerical investigation of wake structures of an atmospheric entry capsule by modal analysis," Physics of Fluids, vol. 31, no. 7, p. 074105, 2019.

[133] G. Yin and M. C. Ong, "On the wake flow behind a sphere in a pipe flow at low Reynolds numbers," Physics of Fluids, vol. 32, no. 10, p. 103605, 2020.

[134] L. Trefethen and D. Bau, III, Numerical Linear Algebra. Society for Industrial and Applied Mathematics, Philadelphia, 1997.

[135] I. Jolliffe, Principal Component Analysis, vol. 3, p. 1580–1584. Wiley-Interscience, 2005.

[136] D. Ruan, H. He, D. A. Castañón, and K. C. Mehta, "Normalized proper orthogonal decomposition (NPOD) for building pressure data compression," Journal of Wind Engineering and Industrial Aerodynamics, vol. 94, no. 6, pp. 447 – 461, 2006.

[137] J. H. Tu, C. W. Rowley, D. M. Luchtenburg, S. L. Brunton, and J. N. Kutz, "On dynamic mode decomposition: Theory and applications," Journal of Computational Dynamics, vol. 1, no. 2, p. 391, 2014.

[138] A. Cammilleri, F. Gueniat, J. Carlier, L. Pastur, E. Memin, F. Lusseyran, and G. Artana, "POD-spectral decomposition for fluid flow analysis and model reduction," Theoretical and Computational Fluid Dynamics, vol. 27, no. 6, pp. 787–815, 2013.

[139] C. Norberg, "Flow around rectangular cylinders: Pressure forces and wake frequencies," Journal of Wind Engineering and Industrial Aerodynamics, vol. 49, pp. 187–196, 12 1993.

[140] D. F. G. Durão, M. V. Heitor, and J. C. F. Pereira, "Measurements of turbulent and periodic flows around a square cross-section cylinder," Experiments in Fluids, vol. 6, pp. 298–304, 1988.

[141] A. Okajima, "Strouhal numbers of rectangular cylinders," Journal of Fluid Mechanics, vol. 123, pp. 379–398, 1982.

[142] S. Luo, M. Yazdani, Y. Chew, and T. Lee, "Effects of incidence and afterbody shape on flow past bluff cylinders," Journal of Wind Engineering and Industrial Aerodynamics, vol. 53, no. 3, pp. 375–399, 1994.

APPENDIX A

CHAPTER 3 APPENDICES

A.1 Integral Quantity Calculations

The integral quantities found in Section 3.4.1 and for additional results presented in Table A.1, were calculated as follows:

$$C_D = \frac{F_X}{\frac{1}{2}AV_\infty^2}; \qquad C_L = \frac{F_Y}{\frac{1}{2}AV_\infty^2}; \tag{A.1a}$$

$$\overline{C_D} = \frac{1}{N}\sum_{i=1}^{N} C_{D,i}; \qquad \overline{C_L} = \frac{1}{N}\sum_{i=1}^{N} C_{L,i}; \tag{A.1b}$$

$$C'_D = \sqrt{\frac{1}{N-1}\sum_{i=1}^{N}(C_{D,i}\overline{C_D})^2}; \qquad C'_L = \sqrt{\frac{1}{N-1}\sum_{i=1}^{N}(C_{L,i}-\overline{C_L})^2}; \tag{A.1c}$$

where F_X and F_Y are the net forces upon the square cylinder in the x- and y-directions, respectively, A is the frontal area of the square cylinder, and N denotes the number of time steps to be averaged over. Additionally, although frequency has been non-dimensionalized in the same manner, the Strouhal number, St is calculated as follows:

$$St = \frac{f_{VS}D}{V_\infty}. \tag{A.2}$$

A.2 Effective Reynolds Number Contours

Included in Figure A.1 are effective Reynolds number (Re_{eff}) contours from the four primary simulations examined throughout this study. Here, it is clearly demonstrated that as f_k is increased, the increased ν_u term (as discussed in Section 3.2) significantly impacts the effective Reynolds number in the region of the inflection lines shown in Figure 3.8. This results in the dampening and/or disappearance of the KH instability/vortices, delaying the transition to turbulence in the wake, and elongating the recirculation length.

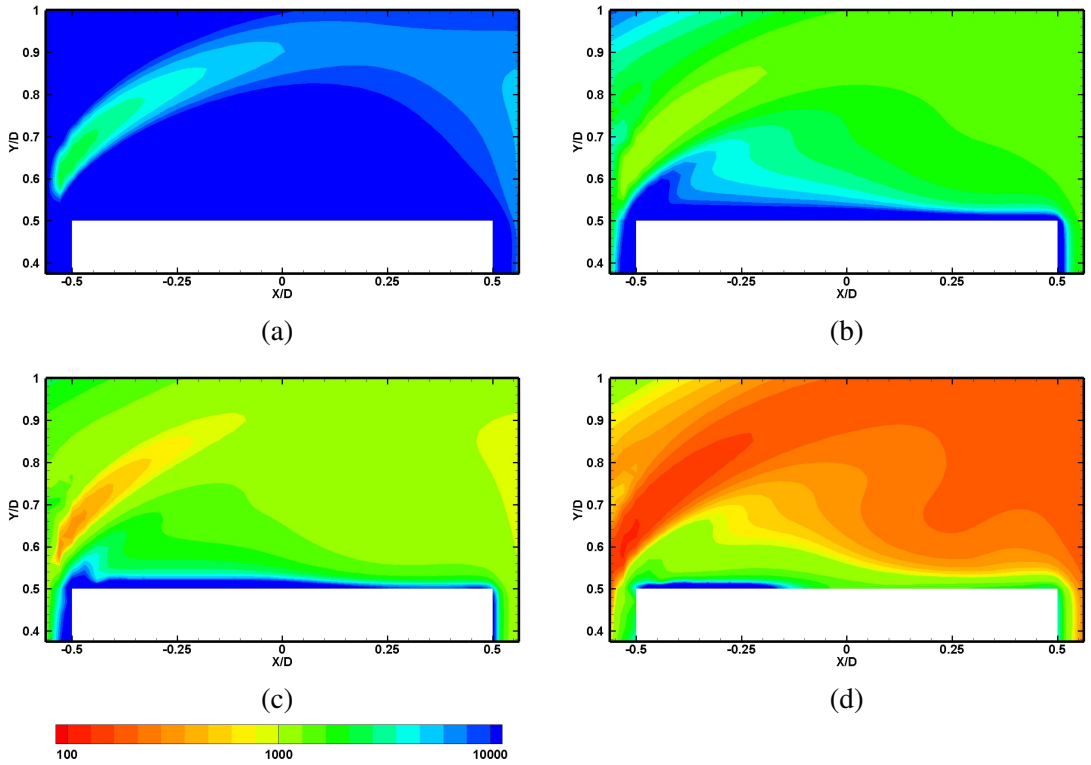

Figure A.1: Contours of effective Reynolds number (Re_{eff}): **(a)** $f_k = 0.10$; **(b)** $f_k = 0.20$; **(c)** $f_k = 0.30$; and **(d)** $f_k = 0.50$. The critical Reynolds number for the Kelvin-Helmholtz instability occurs at $Re \approx 1,000$[24].

Table A.1: Comparison of integral quantities with literature at similar Reynolds number, including: Strouhal number, St; time-averaged drag coefficient, $\overline{C_D}$; root-mean-square lift coefficient, C'_L; root-mean-square drag coefficient, C'_D; and recirculation length, L_R.

Reference	$Re/10^3$	St	$\overline{C_D}$	C'_L	C'_D	L_R
Present, $f_k = 0.50$	22	0.124	2.27	1.46	0.278	1.24
Present, $f_k = 0.30$	22	0.121	2.50	1.64	0.308	1.19
Present, $f_k = 0.20$	22	0.121	2.47	1.70	0.293	1.08
Present, $f_k = 0.10$	22	0.119	2.36	1.73	0.220	1.05
Norberg [139]	13	0.132	2.16			
Durão et al. [140]	14	0.138				1.33
Okajima [141]	20	0.133				
van Oudheusden et al. [11]	20		2.19			1.1
Lyn et al. [12]	21.4	0.13	2.1			1.4
Minguez et al. [13]	21.4	0.130	2.1			
Meliga et al. [14]	22	0.123				1.42
Yen et al. [15]	24	0.134	1.96			
Luo et al. [142]	34	0.13	2.21	1.21	0.18	
Trias et al. [16]	22	0.132	2.18	1.71	0.205	1.04
Verstappen & Veldman [17]	22	0.133	2.09	1.45	0.178	
Cao et al. [18]	22	0.130-0.134	1.98-2.15	1.35-1.53	0.117-0.181	1.04-1.16
Ochoa & Fueyo. [19]	21.4	0.139	2.01	1.4	0.22	1.67
Fureby et al. [20]	21.4	0.129-0.135	2.0-2.2	1.29-1.34	0.17-0.20	1.23-1.37
Minguez et al. [13]	21.4	0.141	2.2			1.28
Rodi [21]	22	0.09-0.15	2.17-2.77	1.15-1.79	0.14-0.27	0.94-1.68
Sohankar et al. [22]	22	0.126-0.132	2.03-2.32	1.23-1.54	0.16-0.20	0.98-1.08
Cao & Tamura [23]	22	0.126-0.133	2.14-2.21	1.26-1.54	0.156-0.210	1.11-1.25

APPENDIX B

CHAPTER 4 APPENDICES

B.1 Supplementary Materials

The following are available online, Video S1: Original Spanwise Vorticity Flow Field, Video S2: 12-Mode POD Reconstruction, Video S3: 12-Mode NPOD Reconstruction, Video S4: 96-Mode POD Reconstruction, Video S5: 96-Mode NPOD Reconstruction, Video S6: DMD-only Reconstruction with f_{KH}-based Pre-Filtering, Video S7: DMD-only Reconstruction with $2f_{VS}$-based Pre-Filtering, Video S8: 12-Mode, f_{KH}-based Pre-filtered POD Reconstruction, Video S9: 12-Mode, $2f_{VS}$-based Pre-filtered POD Reconstruction, Video S10: 96-Mode, f_{KH}-based Pre-filtered POD Reconstruction, Video S11: 96-Mode, $2f_{VS}$-based Pre-filtered POD Reconstruction, Video S12: 12-Mode, f_{KH}-based Pre-filtered NPOD Reconstruction, Video S13: 12-Mode, $2f_{VS}$-based Pre-filtered NPOD Reconstruction, Video S14: 96-Mode, f_{KH}-based Pre-filtered NPOD Reconstruction, Video S15: 96-Mode, $2f_{VS}$-based Pre-filtered NPOD Reconstruction .

B.2 Pre-filtering of Higher Frequencies with A Priori Normalization

Previously in Section 4.4.2, DMD was utilized to filter small time-scales – and hence small length-scales too – prior to performing POD. In this section, the effect of this low-pass filter analog is considered upon NPOD modal components. The same two cut-offs are compared, based upon f_{KH} and $2f_{VS}$. Again, this correlates to an equivalent passing of $2,028$ and 138 of the original $3,998$ frequencies output by the DMD algorithm ($r = 3,998$); and Video S6 and Video S7 demonstrate the immediate effects of the pre-filtered flow fields (provided in the Supplementary Materials).

The components of the first four NPOD modes (m = 1-4) are compared with those which have been subjected to the f_{KH}-based and $2f_{VS}$-based pre-filters. The temporal coefficient signals, $\mathscr{V}_m$, are shown in Figure B.1 and their respective mode shapes, U_m, in Figure B.2. The f_{KH}-based pre-filter signals agree well with the original NPOD signals, at least as well as their POD-counterparts, owing to the limited small time-scales incorporated into the lower modes. Because

of this aspect, even the $2f_{VS}$-based pre-filter signals match well with the original NPOD signals, with much lesser deviation by $m = 4$ as compared to POD. While the signals of both pre-filters match more consistently using NPOD, the difference in magnitudes within their mode shapes do not. By $m = 3$ differences in these magnitudes become apparent with only the conservative pre-filter applied. As expected, these differences manifest early (by $m = 2$) using the more aggressive pre-filtering. Qualitatively, however, it would be difficult to differentiate between these sets of mode shapes, still strongly resembling one another. Additional videos (Video S12 and S13) have been included in the Supplementary Materials based upon the pre-filtered 12-mode NPOD-based reconstructions for comparison with their POD counterparts.

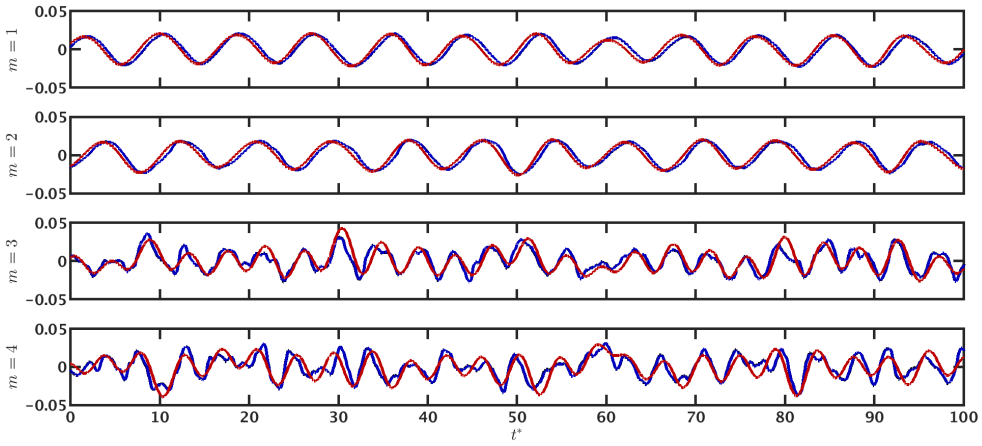

Figure B.1: Pre-filtering with a priori normalization comparison: temporal coefficient signals, $\mathscr{V}_m$, corresponding to the first four output modes (m = 1-4) for: unfiltered NPOD [—]; NPOD pre-filtered by f_{KH} [—]; and NPOD pre-filtered by $2f_{VS}$ [—].

For higher order NPOD modes (m = 93-96), the f_{KH}-based pre-filtered signals do not agree as well with the unfiltered signals as their POD counterparts (as can be seen in Figure B.3). Nonetheless, these signals still capture the overall behavior. The $2f_{VS}$-based pre-filtered signals, however, do not capture this behavior. The more pronounced differences between unfiltered and pre-filtered modes are reflected in their mode shapes, as shown in Figure B.4, exhibiting greater differences

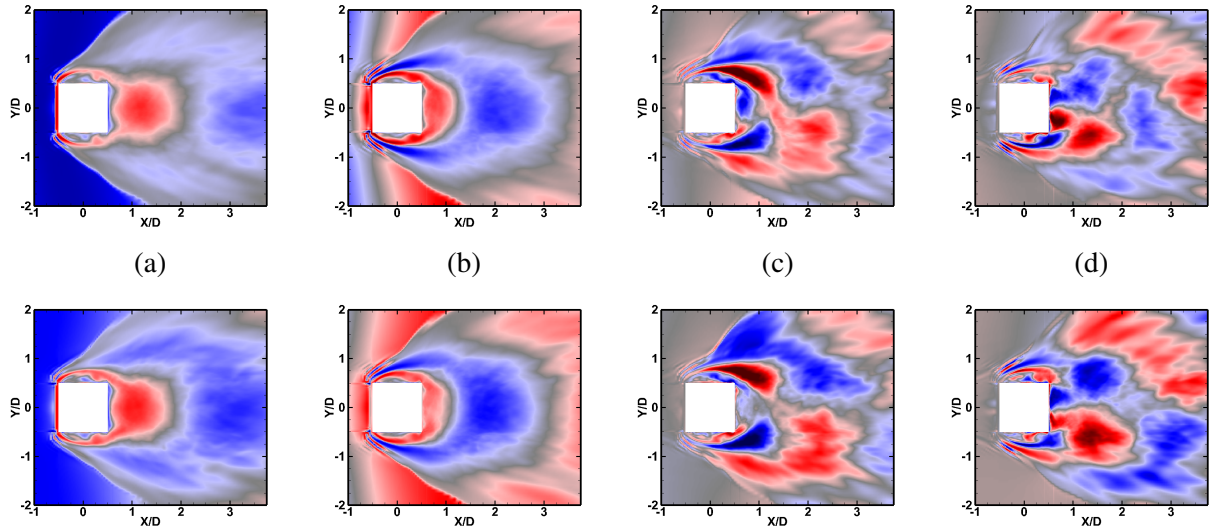

Figure B.2: Pre-filtering with a priori normalization comparison: mode shapes, U_m, corresponding to the first four output modes (m = 1-4) for: **(a-d)** NPOD pre-filtered by f_{KH}; and **(e-h)** NPOD pre-filtered by $2f_{VS}$, respectively.

than their POD equivalents do. Video S14 and S15 have been included in the Supplementary Materials based upon the pre-filtered 96-mode NPOD-based reconstructions for additional comparison.

B.3 Sampling Rate Reduction with A Priori Normalization

In Section 4.4.3, the (artificial) reduction of the sampling rate was implemented, using DMD, in accordance with the Nyquist criterion (relative to the frequency cut-off of the pre-filter) prior to performing POD. In this section the effects are reviewed instead performing NPOD. As before, the sampling rate of the original dataset is reduced from $St = 14.55$ to $St = 7.27$ and $St = 0.48$ for the f_{KH}-based and $2f_{VS}$-based pre-filters, respectively. The length of the sampling window is maintained constant, meaning the original $5,757$ snapshots are reduced to $2,879$ and 193 snapshots, accordingly.

Figure B.5 and Figure B.6 clearly show that almost no information is lost via reduction of the sampling rate for the f_{KH}-based pre-filtered signals. Only at higher order modes are these minor differences perceptible. Similarly, in Figure B.7, it is evident that the sample rate reduction

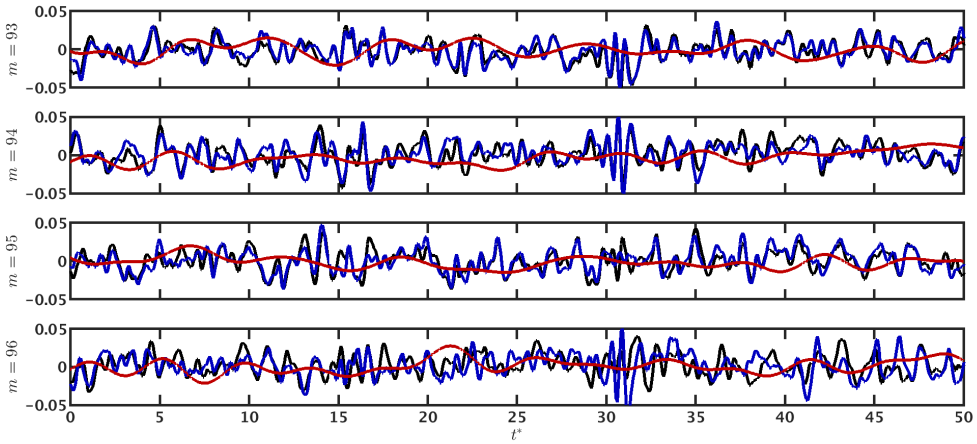

Figure B.3: Pre-filtering with a priori normalization comparison: temporal coefficient signals, $\mathscr{V}_m$, corresponding to four higher order modes (m = 93-96) for: unfiltered NPOD [—]; NPOD pre-filtered by f_{KH} [—]; and NPOD pre-filtered by $2f_{VS}$ [—].

had negligible impact on the structures within the NPOD mode shapes. Although, the magnitude of these structures is marginally different. Overall, the sample rate reduction for the f_{KH}-based pre-filtered NPOD modes does not lose any significant information as compared to the original sampling rate.

As for the $2f_{VS}$-based pre-filtered signals, Figure B.8 clearly indicates that for lower order modes, information is not lost by sample rate reduction. The same is found in Figure B.9 for the lower order mode shapes, with only minor differences manifesting where steep gradients occur. Further analysis of the $2f_{VS}$-based pre-filter with reduced sampling has been omitted for these NPOD modes, due to the inconsistencies of the signals and mode shapes shown in the previous subsection.

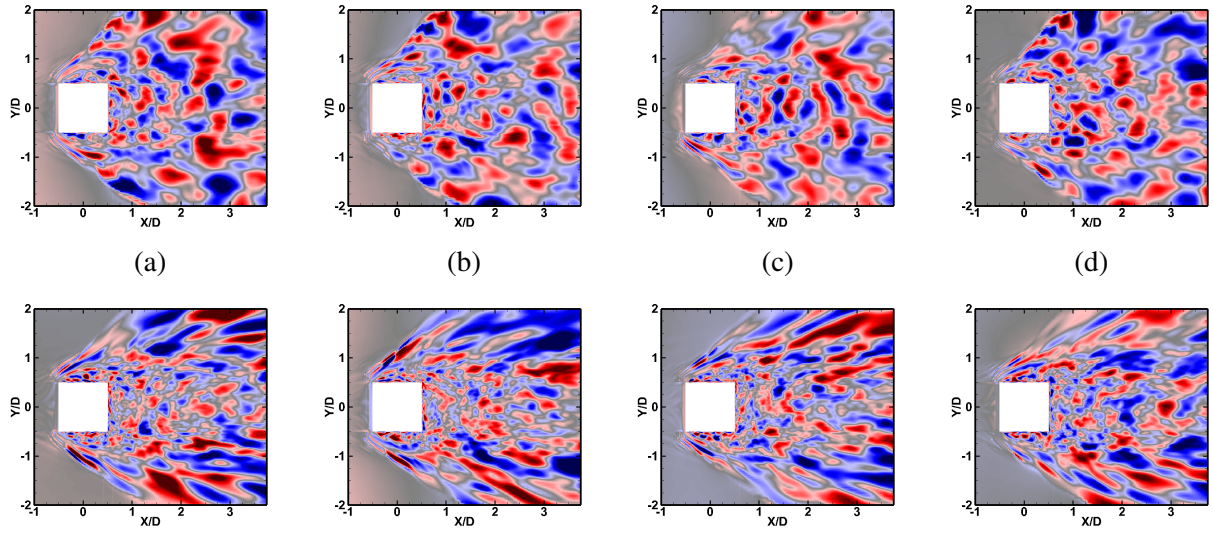

Figure B.4: Pre-filtering with a priori normalization comparison: mode shapes, U_m, corresponding to four higher order modes (m = 93-96) for: **(a-d)** NPOD pre-filtered by f_{KH}; and **(e-h)** NPOD pre-filtered by $2f_{VS}$, respectively.

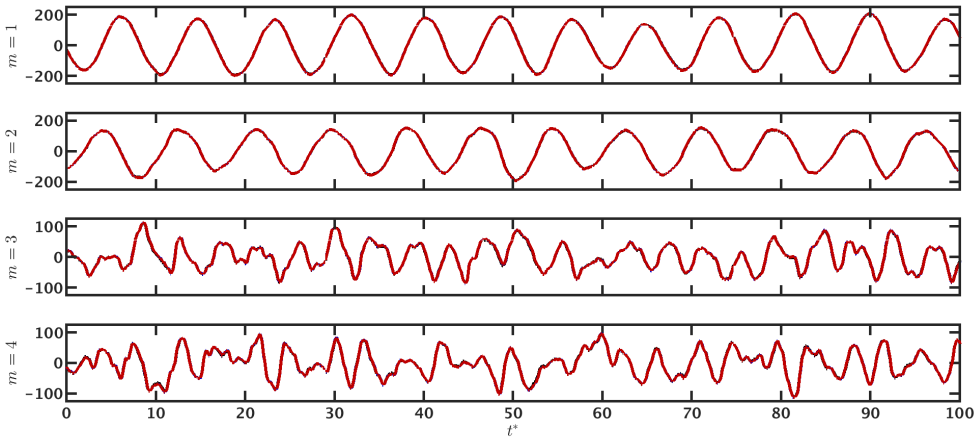

Figure B.5: Sampling rate reduction comparison: amplified temporal coefficient signals, $\sigma_m \mathscr{V}_m$, corresponding to the first four output modes (m = 1-4) for: unfiltered NPOD [—]; NPOD pre-filtered by f_{KH} [—]; and NPOD pre-filtered by f_{KH} with reduced sampling [—].

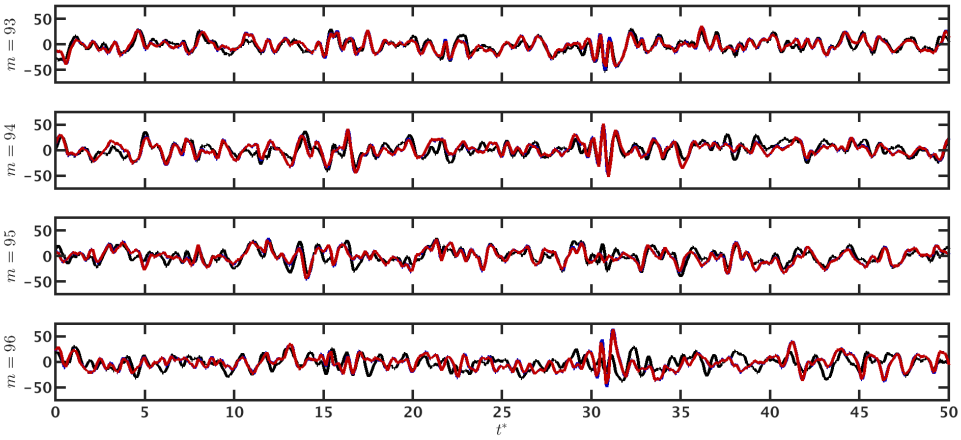

Figure B.6: Sampling rate reduction comparison: amplified temporal coefficient signals, $\sigma_m \mathscr{V}_m$, corresponding to four higher order modes (m = 93-96) for: unfiltered NPOD [—]; NPOD pre-filtered by f_{KH} [—]; and NPOD pre-filtered by f_{KH} with reduced sampling [—].

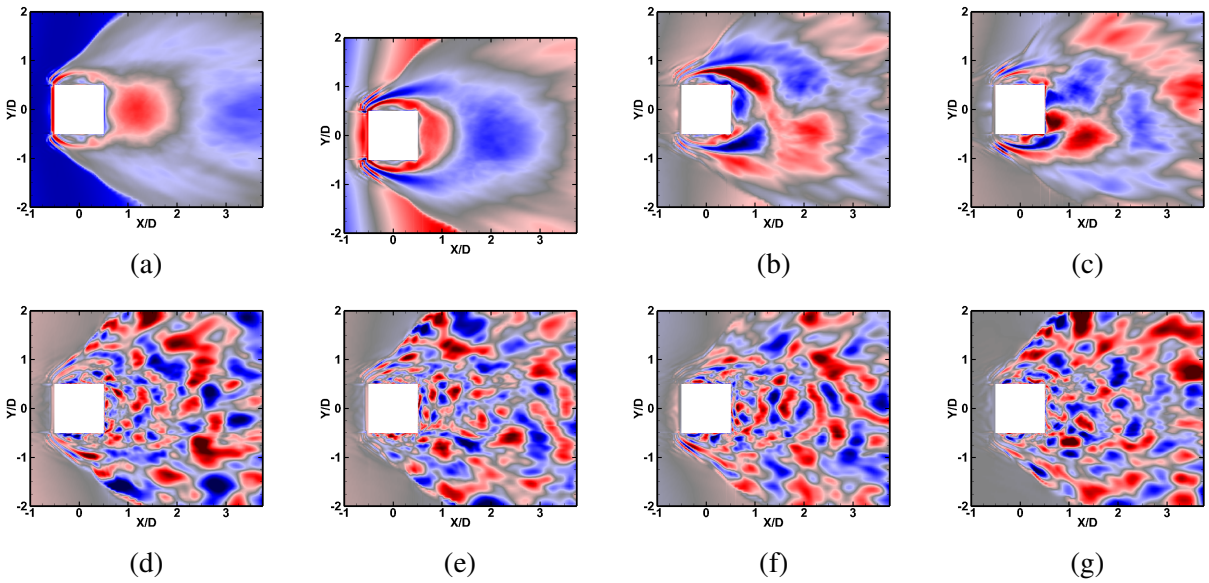

Figure B.7: Sampling rate reduction comparison: mode shapes, U_m, for NPOD pre-filtered by f_{KH} with reduced sampling rate, corresponding to: **(a-d)** the first four output modes (m = 1-4); and **(e-h)** four higher order output modes(m = 93-96).

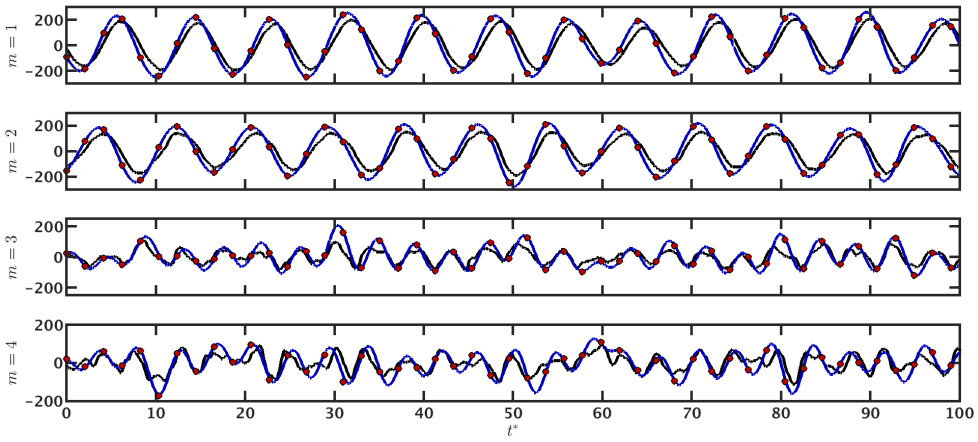

Figure B.8: Sampling rate reduction comparison: amplified temporal coefficient signals, $\sigma_m \mathscr{V}_m$, corresponding to the first four output modes (m = 1-4) for: unfiltered NPOD [—]; NPOD pre-filtered by $2f_{VS}$ [—]; and NPOD pre-filtered by $2f_{VS}$ with reduced sampling [•].

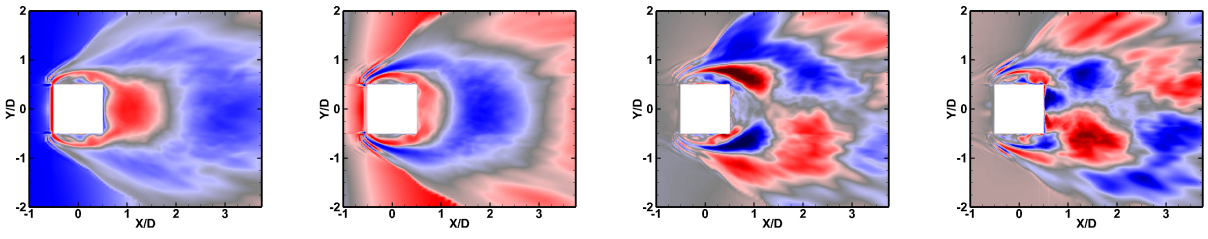

(a) (b) (c) (d)

Figure B.9: Sampling rate reduction comparison: mode shapes, U_m, for NPOD pre-filtered by $2f_{VS}$ with reduced sampling rate, corresponding to: **(a-d)** the first four output modes (m = 1-4).